



Synthesis of Waveguide Antenna Arrays Using the Coupling Matrix Approach

Rashad Hassan Mahmud

A thesis submitted to the University of Birmingham for the degree of
Doctor of Philosophy

**School of Electronic, Electrical and Computer Engineering
College of Engineering and Physical Science
The University of Birmingham
December, 2015**

UNIVERSITY OF
BIRMINGHAM

University of Birmingham Research Archive

e-theses repository

This unpublished thesis/dissertation is copyright of the author and/or third parties. The intellectual property rights of the author or third parties in respect of this work are as defined by The Copyright Designs and Patents Act 1988 or as modified by any successor legislation.

Any use made of information contained in this thesis/dissertation must be in accordance with that legislation and must be properly acknowledged. Further distribution or reproduction in any format is prohibited without the permission of the copyright holder.

Abstract

Synthesis of Waveguide Antenna Arrays Using the Coupling Matrix Approach

Rashad Hassan Mahmud.

The University of Birmingham, December 2015

With the rapid development in communication systems in recent years, improvements in components of the systems such as antennas and bandpass filters are continuously required to provide improved performance. High gain, wide bandwidth, and small size are the properties of antennas which are demanded in many modern applications, and achieving these simultaneously is a challenge. This thesis presents a new design approach to address this challenge.

The coupling matrix is an approach used to represent and design the circuits made of coupled-resonators such as filters and multiplexers. The approach has been utilised in this thesis to integrate a single waveguide resonator-based aperture antenna with an n^{th} order filter circuit. The integrated component named an *antenna-filter* is capable of providing a controllable bandwidth and additionally introduces the filtering functionality. Design and fabrication for a single waveguide resonator-based aperture antenna integrated with a 3rd order bandpass filter has been presented in this thesis to verify the approach.

The design approach is further developed in order to integrate bandpass filters with an $N \times N$ waveguide resonator-based aperture antenna array. This is to increase the gain of the array as well as provide the filtering. The integrated component here is called *antenna array-filter*. In addition to the controllable bandwidth, the integrated component can now provide an increased gain. Five novel *antenna array-filter* components have been fabricated in this thesis for the purpose of validation.

This thesis also looks at a 300 GHz communication system which is being proposed at The University of Birmingham with the objective to build a 10 metre indoor communication link with the data rate capacity of 10 Gbit/s. The system is to be constructed out of filtering rectangular waveguide resonators together with active elements. In this thesis attention is paid to the antenna required by the system. A 300 GHz planar (8×8) slotted waveguide antenna array has been designed and fabricated.

Acknowledgements

I am very thankful to the creator of the universe, the Almighty, and the Merciful for His blessing given during this PhD study. I express my deepest gratitude to my supervisor Professor Michael J. Lancaster, not only for his advices and guidance throughout this PhD project, but also for all the support whenever I needed it. I would also like to thank my second supervisor Dr. Fred Huang for his useful suggestions and comments during our meetings. Additionally, I am thankful to Dr. Yi Wang from the University of Greenwich for his valuable discussions on terahertz circuits.

The work presented in this thesis might never have been accomplished without the ever continuing support of my colleagues in the Emerging Device Technology Research Group, particularly, Dr. Xiaobang Shang, Dr. Wenlin Xia, Mofei Guo, Dr. Ekasit Nugoolcharoenlap, Dr. Konstantinos Konstantinidis, and Ben Willetts. I am thankful to Mr. Warren Hay in the School of Physics for fabricating the waveguide circuits. Thanks to Mr. Sean Gardner for all the support regarding academic writing skills.

My special thanks go to all of my Kurdish friends at the University of Birmingham. I am also grateful to my cousin and his wife in the UK; they have always made me feel like I was at home during my study. I would also like to thank my lecturers and colleagues in the Physics department at Salahaddin University-Hawler, especially, my M.Sc. supervisor Assistant Professor Dr. Star O. Hassan, my B.Sc. project supervisor Assistant Professor Dr. Mudhaffer M. Ameen and Mr. Hiwa H. Aziz.

I would like to acknowledge the Kurdistan regional government for awarding me a scholarship to pursue the PhD degree in the UK. Finally, I am deeply indebted to my family for their everlasting encouragement, and all their financial support especially after my sponsor was no longer able to continue funding my study.

Dedications

- *To my mother and father*
- *To my sisters and brothers*

List of Contents

| | | |
|------------------|---|----------|
| CHAPTER 1 | INTRODUCTION..... | 1 |
| 1.1 | Research motivation and objectives..... | 1 |
| 1.2 | Thesis organisation..... | 4 |
| 1.3 | References..... | 6 |
| CHAPTER 2 | BASIC CONCEPTS OF ANTENNAS | 7 |
| 2.1 | Introduction | 7 |
| 2.2 | High gain antennas | 10 |
| 2.2.1 | <i>Antenna gain limitation.....</i> | 13 |
| 2.3 | Wide bandwidth antennas..... | 15 |
| 2.3.1 | <i>Antenna bandwidth limitation.....</i> | 16 |
| 2.4 | Waveguides..... | 20 |
| 2.5 | Waveguide antennas..... | 24 |
| 2.5.1 | <i>Slotted waveguide antennas.....</i> | 24 |
| 2.5.2 | <i>Design of linear array broad-wall slotted waveguide antennas.....</i> | 28 |
| 2.5.3 | <i>Design of linear array Narrow-wall slotted waveguide antennas.....</i> | 32 |
| 2.6 | Conclusions..... | 35 |
| 2.7 | References..... | 36 |

| | | |
|------------------|---|-----------|
| CHAPTER 3 | FILTER THEORIES AND ANTENNA-FILTER INTEGRATION... | 39 |
| 3.1 | Overview of filter theories..... | 39 |
| 3.2 | General coupling matrix theory..... | 44 |
| 3.3 | Cavity resonators..... | 50 |
| 3.3.1 | <i>Rectangular waveguide cavity resonators</i> | 51 |
| 3.4 | Design of a 3 rd order coupled-resonators waveguide filter..... | 53 |
| 3.4.1 | <i>Extraction of the external quality factor (Q_e)</i> | 56 |
| 3.4.2 | <i>Extraction of the internal coupling (Coupling coefficient M_{12}, M_{23})</i> ... | 57 |
| 3.4.3 | <i>Integration and optimisation</i> | 60 |
| 3.5 | <i>Antenna-filter</i> integration overview..... | 61 |
| 3.6 | Radiation quality factor calculation for a cavity resonator-based aperture antenna | 65 |
| 3.7 | Coupling matrix representation for <i>antenna-filter</i> integration..... | 67 |
| 3.8 | Conclusions..... | 70 |
| 3.9 | References..... | 71 |
| CHAPTER 4 | WAVEGUIDE APERTURE ANTENNA ARRAY DESIGN..... | 73 |
| 4.1 | 3 rd order <i>antenna-filter</i> component..... | 73 |
| 4.1.1 | <i>Design and simulation</i> | 73 |
| 4.1.2 | <i>Fabrication and measurement</i> | 77 |
| 4.2 | 2 nd order <i>antenna array-filter</i> component..... | 80 |

| | | |
|---|---|------------|
| 4.2.1 | <i>Design and simulation</i> | 80 |
| 4.2.2 | <i>Fabrication and measurement</i> | 82 |
| 4.3 | 3 rd order 2×2 antenna array-filter component..... | 84 |
| 4.3.1 | <i>Design and simulation</i> | 84 |
| 4.3.2 | <i>Fabrication and measurement</i> | 87 |
| 4.4 | 7 nd order 4×4 antenna array-filter component..... | 89 |
| 4.4.1 | <i>Design and simulation</i> | 90 |
| 4.4.2 | <i>Fabrication and measurement</i> | 94 |
| 4.5 | Conclusions..... | 98 |
| 4.6 | References..... | 98 |
| CHAPTER 5 SINGLE WAVEGUIDE-LAYER PLANAR ARRAY ANTENNA DESIGN | | 100 |
| 5.1 | 3 rd 2×2 antenna array-filter component..... | 100 |
| 5.1.1 | <i>Design and simulation</i> | 100 |
| 5.1.2 | <i>Fabrication and measurement</i> | 103 |
| 5.2 | Comparison..... | 106 |
| 5.3 | 4 th order 4×4 antenna array-filter component..... | 109 |
| 5.3.1 | <i>Design and simulation</i> | 109 |
| 5.3.2 | <i>Fabrication and measurement</i> | 113 |

| | | |
|--|--|------------|
| 5.4 | Comparison..... | 116 |
| 5.5 | Conclusions..... | 119 |
| 5.6 | References..... | 119 |
| CHAPTER 6 TERAHERTZ COMMUNICATION SYSTEMS AND ANTENNAS. | | 120 |
| 6.1 | Terahertz frequency band and its applications..... | 120 |
| 6.2 | Terahertz in wireless communication systems..... | 122 |
| 6.3 | 300 GHz wireless communication system..... | 124 |
| 6.4 | Terahertz antennas..... | 126 |
| 6.5 | Design of 300 GHz planar array 8×8 slotted waveguide antenna..... | 129 |
| 6.5.1 | <i>Simulation results</i> | 130 |
| 6.5.2 | <i>Fabrication</i> | 132 |
| 6.6 | Micromachined travelling-wave array slotted waveguide antenna..... | 135 |
| 6.6.1 | <i>Design of HBR slot</i> | 136 |
| 6.6.2 | <i>Design of linear array with 8-radiating slots</i> | 137 |
| 6.6.3 | <i>Design performance</i> | 138 |
| 6.6.4 | <i>Main beam scanning</i> | 139 |
| 6.7 | Conclusions..... | 142 |
| 6.8 | References..... | 143 |
| CHAPTER 7 CONCLUSIONS AND FUTURE WORK..... | | 146 |

| | | |
|-----|------------------|-----|
| 7.1 | Conclusions..... | 146 |
| 7.2 | Future work..... | 147 |
| 7.3 | References..... | 150 |

List of Figures

| Figures | Title | page no. |
|----------------|--|-----------------|
| Figure 1.1 | Guglielmo Marconi standing on the left hand side watching his research associates raise the antenna using the kite, Newfoundland, 1901[3] | 2 |
| Figure 1.2 | A simplified terahertz communication link budget diagram. All the components of the system are to be fabricated using micromaching. Five SU-8 layers are needed to package the whole system including the antenna [5]. The physical layout of the system is demonstrated in Chapter 6 (Figure 6.4) | 2 |
| Figure 2.1 | An electric charge moves towards point A and then, it is accelerated towards point B [1] | 8 |
| Figure 2.2 | A communication link including a transmitting antenna and a receiving antenna. The transmitting antenna radiates. The radiated waves are in the form of spherical waves. As they propagate over a large distance, the waves change and become approximately plane waves. This diagram is reproduced from [2] | 9 |
| Figure 2.3 | Equivalent circuit representation of a transmitter antenna [3]. | 9 |
| Figure 2.4 | A parabolic 70 m dish antenna is used in the Goldstone Observatory station, Mojave Desert, California, USA [4] | 12 |
| Figure 2.5 | An array of four axial-mode helical antennas, France [7] | 12 |
| Figure 2.6 | A planar array slotted waveguide antenna is used in the radar system in the NASA Boeing plane 737 [8] | 12 |
| Figure 2.7 | (a) An antenna placed in a spherical coordinate system, (b) The variation of the maximum antenna gain versus different antenna sizes | 14 |

| | | |
|-------------|---|----|
| Figure 2.8 | (a) A Pyramidal horn antenna with its 3-D radiation pattern [20], (b) A Vivaldi antenna [21] | 16 |
| Figure 2.9 | The Reflection S_{11} parameter of an antenna | 17 |
| Figure 2.10 | The variation of the radiation Q of a linearly polarised electrically small antenna versus the antenna size according to Chu and Mclean's criteria [23] | 18 |
| Figure 2.11 | Four possible RC and RL circuits of a small antenna with a matching network: (a) RC is in series, (b) RL is in series, (c) RC is in parallel, and (d) RL is in parallel (This diagram is reproduced from [27]) | 19 |
| Figure 2.12 | A rectangular waveguide geometry | 20 |
| Figure 2.13 | Configuration of cut-off frequencies of different propagated mode $a=25$ mm, $b = 10$ mm air filled. The cut-off frequency is calculated using Equation 2.9 (This figure is re-drawn from [29]) | 21 |
| Figure 2.14 | The distribution of the magnetic field and current lines on the walls of a rectangular waveguide operated at TE_{10} mode (Taken from [31]) | 23 |
| Figure 2.15 | Illustration of the electric and magnetic fields of both dipole and slot antenna configurations | 24 |
| Figure 2.16 | Broad and narrow walls slotted waveguide antennas with their aperture electric field distributions and predicted radiation patterns | 26 |
| Figure 2.17 | Some slots cut in the walls of the waveguide (Taken from [5]) | 26 |
| Figure 2.18 | Longitudinal waveguide slot antenna with its equivalent circuit [36] | 27 |
| Figure 2.19 | Layout of 8-slots cut in the broad-wall of the waveguide based on the micromachined layers ($a = 0.864$ mm, $b = 0.432$ mm, $b_1 = 0.300$ mm). The outstanding structure in the central area represents the hollow waveguide WR-03 and slots, while the surrounding conductors are set to be transparent | 29 |
| Figure 2.20 | (a) The initial reflection coefficient response S_{11} (red line) in | 31 |

| | | |
|-------------|--|----|
| | comparison to the optimised (green line), (b) Variation of the antenna directivity, realised gain, and total efficiency versus frequency | |
| Figure 2.21 | Simulated radiation pattern of the antenna in the E- and H-planes at three different frequencies including the centre frequency | 31 |
| Figure 2.22 | Layout of 8-slots cut in the narrow-wall of the waveguide based on the micromachined layers ($a = 0.864$ mm, $b = 0.432$ mm, $b_1 = 0.288$ mm). The outstanding structure in the central area represents the hollow waveguide WR-03 and slots, while the surrounding conductors are set to be transparent | 32 |
| Figure 2.23 | a) The design of the WR-03 waveguide H-bend. The dimensions are; $a = 0.864$ mm, $b = 0.432$ mm, $b_1 = 0.288$ mm, $m_1 = 0.1$ mm, $m_2 = 0.083$ mm, $w_1 = 0.187$ mm, $w_2 = 0.139$ mm, (b) The simulated response of the bend | 34 |
| Figure 2.24 | a) Initial reflection coefficient response S_{11} (red line) compared to the optimised (green line), (b) Variation of the antenna directivity, realised gain, and total efficiency versus frequency | 34 |
| Figure 2.25 | Simulated radiation pattern of the antenna in both the E- and H-planes at three different frequencies including the centre frequency | 35 |
| Figure 3.1 | Two-port network representation of a filter circuit. E_s is the voltage of the source, Z_{01} and Z_{02} are the impedances of the source and the load, and I_1 , I_2 and V_1 , V_2 are the current and the voltage parameters of the source and the load, respectively (re-produced from [2]) | 40 |
| Figure 3.2 | Chebyshev response of a lowpass prototype filters | 43 |
| Figure 3.3 | An ideal response of a 3 rd order low pass filter based on the Chebyshev response with a 0.0436 dB passband ripple, (a) the magnitude of the S-parameters, (b) The enlarged scale of S_{21} to show the passband level | 44 |
| Figure 3.4 | Two equivalent circuits of a filter made out of n -coupled resonators. The resonators are coupled, (a) magnetically by the mutual | 45 |

| | | |
|-------------|--|----|
| | inductances, (b) electrically by the mutual capacitances [2] | |
| Figure 3.5 | Layout of a 3 rd order filter based on the waveguide cavity resonators. | 49 |
| Figure 3.6 | Four possible equivalent circuits for a cavity resonator. A lossless cavity when the elements are: (a) in series, and (b) in parallel. A lossy cavity when the elements are: (c) in series, and (d) in parallel [7] | 51 |
| Figure 3.7 | Rectangular waveguide cavity with the configuration of the electromagnetic field for the propagated TE ₁₀₁ mode | 52 |
| Figure 3.8 | An ideal response of a 3 rd order Chebyshev filter | 55 |
| Figure 3.9 | a) Physical structure of the 3 rd order waveguide filter based on the waveguide coupled-resonators, (b) its equivalent topology | 55 |
| Figure 3.10 | Structure modelled in CST for the extraction of the Q_e , (a) inside view of the structure, (b) the real structure. Dimensions, $a = 22.86$ mm, $b=10.16$ mm, $l_0=10.16$ mm, $h_0 = 0.04$ mm, $t=2$ mm | 56 |
| Figure 3.11 | (a) the S_{21} response of the structure modelled in CST and is shown in Figure 3.9, (b) variation of the Q_e versus the cavity dimensions | 57 |
| Figure 3.12 | Structure modelled in CST for the extraction of the internal coupling (coupling coefficient M_{12}) between two electrically coupled resonators, (a) inside view of the structure, (b) the real structure. Dimensions, $a = 22.86$ mm, $b = 10.16$ mm, $l_0 = 10.16$ mm, $h_0 = 0.04$ mm, $t = 2$ mm. Both of l_1 and dk_{12} are variables to control the M_{12} (Round corner 1.6 mm) | 59 |
| Figure 3.13 | a) the S_{21} response of the two-coupled structure modelled in CST, and is shown in Figure 3.11, (b) variation of the M_{12} versus the cavity dimensions | 59 |
| Figure 3.14 | Structure modelled in CST for the final design of the 3 rd order coupled-resonator filter, (a) inside view of the filter structure, (b) the real filter structure | 59 |

| | | |
|-------------|--|----|
| Figure 3.15 | Initial response compared with the optimisation, (b) optimised response compared with the ideal response obtained from the coupling matrix | 61 |
| Figure 3.16 | Topology shows the conventional way for the integration of an antenna with a bandpass filter using a matching circuit | 62 |
| Figure 3.17 | New approach of the integration of an antenna with a filter based on the coupled resonators circuit | 63 |
| Figure 3.18 | Layout of a single resonator-radiator fed weakly from one side and opened to space at another side via an aperture. The structure is resonated at centre frequency 10 GHz with the dimensions; $a=22.86$ mm, $b = 10.16$ mm, $d_r=1$ mm, $l_0= 10.16$ mm, and $t = 2$ mm. (a) the outstanding structure in the central area represents the hollow waveguide WR-90 and an aperture, while the surrounding conductors are set to be transparent). (b) The real structure | 66 |
| Figure 3.19 | (a) Frequency response S_{11} of the waveguide cavity <i>resonator-radiator</i> shown in Figure 3.18, (b) Extraction of the radiation quality factor Q_r of the <i>resonator-radiator</i> shown in Figure 3.18 based on the magnitude of S_{11} for different l_a values with simultaneous change of l_r to keep the resonant frequency at (10 GHz); $t_r= 10$ mm, $a = 22.86$ mm, $b = 10.16$ mm, $l_0= 10.16$ mm, $d_r= 1$ mm. | 67 |
| Figure 3.20 | a) Topology of an n -coupled resonator filter, (b) topology of <i>antenna-filter</i> component made out of n -coupled resonator | 68 |
| Figure 3.21 | (a) Topology of a multiple-output circuit based on n -coupled resonator filter, (b) topology of an <i>antenna array-filter</i> component made out of n -coupled resonator | 69 |
| Figure 4.1 | a) Proposed topology for the 3 rd order <i>antenna-filter</i> component. Resonator 3 (grey) acts as a radiator as well as the last resonator. (b) Physical configuration. Dimensions in mm are: $a = 22.86$, $b = 10.16$, t | 74 |

= 2, $l_0 = 15$, $d_y = 8.62$, $d_z = 88.32$, other dimensions can be found in Table 4.1, radius of the round corners =1.6

| | | |
|-------------|--|----|
| Figure 4.2 | (a) Equivalent coupling matrix for the 3 rd order <i>antenna-filter</i> component, (b) Ideal response of the reflection coefficient S_{11} of the 3 rd order <i>antenna-filter</i> component | 74 |
| Figure 4.3 | The simulated initial response of S_{11} parameter of the 3 rd order <i>antenna-filter</i> component, (b) The optimised response compared with the calculated, (c) Simulated total efficiency versus frequency | 76 |
| Figure 4.4 | (a) Photograph of the fabricated 3 rd order <i>antenna-filter</i> component, (b) The component under test | 77 |
| Figure 4.5 | (a) Measured return loss compared with simulated, (b) Measured realised gain of the compared with simulated | 78 |
| Figure 4.6 | Measured radiation pattern of the 3 rd order <i>antenna-filter</i> component for both the E- and H-planes at three frequencies including the centre frequency | 79 |
| Figure 4.7 | (a) Physical configuration, and (b) Equivalent topology and scaled coupling matrix of the 2 nd order <i>antenna array-filter</i> component. Dimensions in mm are: $a = 22.86$, $b = 10.16$, $t = 2$, $t_r = 10$, $d_0 = 6.62$, $d_r = 9.30$, $l_0 = 15$, $l_1 = 24.51$, $l_r = 18$, $l_a = 17.22$, radius of the round corners =1.6 | 81 |
| Figure 4.8 | a) Simulated return loss and realised gain of the 2 nd order <i>antenna array-filter</i> component compared with obtained results from the coupling matrix, (b) Simulated total efficiency of the component versus frequencies | 81 |
| Figure 4.9 | a) Photograph, and (b) Measured response of the 2 nd order <i>antenna array-filter</i> component | 82 |
| Figure 4.10 | Measured radiation pattern of the 2 nd order <i>antenna array-filter</i> component for both the E- and H-planes at three frequencies including | 83 |

the centre frequency

- Figure 4.11 (a) Topology (b) scaled coupling matrix, and (c) physical realisation of the 3rd order 2×2 *antenna array-filter* component. The dimensions in mm are: $a = 22.86$, $b = 10.16$, $l_0 = 8$, $l_1 = 19.76$, $l_2 = 23.90$, $l_r = 20.10$, $l_a = 17.65$, $t = 2$, $t_r = 10$, $d_0 = 17.70$, $dk_{12} = 1.14$, $d_r = 3.55$, $x = 79.56$, $y = 58.48$, $z = 42.86$, radius of the round corners = 1.6 86
- Figure 4.12 : (a) Simulated response of the 3rd order 2×2 *antenna array-filter* component compared with the calculated response, (b) Simulated total efficiency 86
- Figure 4.13 (a) Photograph, and (b) Simulated and calculated responses of the 3rd order 2 × 2 *antenna array-filter* component 87
- Figure 4.14 The simulated and measured radiation pattern of the 3rd order 2×2 *antenna array-filter* component for both the E- and H-panes at three different frequencies 88
- Figure 4.15 Proposed topology for the 7th order 4×4 *antenna array-filter* component 91
- Figure 4.16 Layout view of the 7th order 4×4 *antenna array-filter* component modelled in the CST. The physical dimensions in mm are: $d_0 = 4.9779$, $d_{k12} = 1.7156$, $d_{k23} = 0.9132$, $d_{k34} = 1.6859$, $d_{k45} = 11.5715$, $d_{k56} = 0.6909$, $d_{k67} = 5.7733$, $l_1 = 25.3234$, $l_2 = 22.4451$, $l_3 = 21.7848$, $l_4 = 19.7931$, $l_5 = 20.4377$, $l_6 = 21.5814$, $l_7 = 22.0414$, $l_a = 17.2726$, $x_1 = 6.5500$, $x_2 = 15.7800$, $t = 2.0$, $t_r = 10$, $d_x = 24.32$, $d_y = 34.31$, $l_x = 113.5$, $l_y = 150.4$, radius of the round corners = 1.6 92
- Figure 4.17 Simulated frequency responses compared with the calculated of the 7th order 4×4 *antenna array-filter* component 93
- Figure 4.18 Simulated total efficiency of the 7th order 4×4 *antenna array-filter* component 94
- Figure 4.19 Photograph of the fabricated 7th order 4 × 4 *antenna array-filter* 95

| | | |
|-------------|---|-----|
| | component | |
| Figure 4.20 | a) The 7 th order 4×4 <i>antenna array-filter</i> component under test, (b) Measured frequency responses compared with the simulated | 96 |
| Figure 4.21 | Measured radiation pattern of the 7 th order 4×4 <i>antenna array-filter</i> component compared with the simulated at three different frequencies for both the E- and H-planes | 97 |
| Figure 5.1 | a) Topology, and (b) equivalent coupling matrix of the 3 rd order 2×2 <i>antenna array-filter</i> component | 102 |
| Figure 5.2 | Physical structure of the 3 rd order 2×2 <i>antenna array-filter</i> component. The dimensions in mm are: $a = 22.86$, $b = 10.16$, $b_1 = 7.0$, $l_0 = 11$, $l_1 = 26.55$, $l_2 = 26.47$, $l_3 = 20.21$, $l_a = 18.60$, $t = 2$, $t_r = 10$, $d_0 = 4.80$, $dk_{12} = 1.45$, $dk_{23} = 3.12$, $dk_{25} = 2.95$, $x_1 = 8.138$, $x = 82.12$, $y = 43.32$, $z = 42.86$, $l_x = 23.04$, $l_y = 21.16$, radius of round corners = 1.6 | 102 |
| Figure 5.3 | (a) Frequency responses of the 3 rd order 2×2 <i>antenna array-filter</i> component compared with the desired responses calculated from the coupling matrix (b) simulated total efficiency | 102 |
| Figure 5.4 | Photograph of the fabricated 3 rd order 2×2 <i>antenna array-filter</i> component | 104 |
| Figure 5.5 | Measured frequency responses of the 3 rd order 2×2 <i>antenna array-filter</i> component compared with the simulated | 104 |
| Figure 5.6 | The simulated radiation pattern of the 3 rd order 2×2 <i>antenna array-filter</i> component for both the E- and H-planes at three different frequencies | 105 |
| Figure 5.7 | Proposed topology for the 4 th order 4×4 <i>antenna array-filter</i> component | 110 |
| Figure 5.8 | Figure 5.8: (a) Physical configuration of the 4 th order 4×4 <i>antenna array-filter</i> component modelled in the CST. The physical dimensions in mm are: $d_0 = 15.68$, $dk_{12} = 1.48$, $dk_{23} = 0.82$, $dk_{341} = 1.52$, $dk_{342} = 1.64$, | 111 |

$l_1 = 15.70$, $l_2 = 21.20$, $l_3 = 25.62$, $l_4 = 20.38$, $l_a = 17.00$, $x_1 = 5.46$, $x_2 = 6.21$, $t = 2.0$, $t_0 = 1$, $t_r = 10$, $d_x = 21.46$, $d_{y1} = 32.22$, $d_{y2} = 41.98$, $l_x = 90$, $l_y = 140$, $l_z = 42.86$, radius of the round corners = 1.6. (b) The E-field distribution inside the component at 10 GHz with the aid of CST [2]

| | | |
|-------------|--|-----|
| Figure 5.9 | Frequency responses of the 4 rd order 4×4 <i>antenna array-filter</i> component compared with the desired responses calculated from the coupling matrix | 112 |
| Figure 5.10 | Simulated total efficiency response of the 4 rd order 4×4 <i>antenna array-filter</i> component | 112 |
| Figure 5.11 | (a) Photograph, and (b) Measured frequency response of the fabricated 4 th order 4 × 4 <i>antenna array-filter</i> component compared with the simulated response | 114 |
| Figure 5.12 | The simulated radiation pattern of the 7 rd order 4×4 <i>antenna array-filter</i> component for both the E- and H-planes at three different frequencies | 115 |
| Figure 6.1 | Terahertz frequency region illustration at the electromagnetic spectrum [1] | 121 |
| Figure 6.2 | Terahertz photo taken for a closed cardboard box [6] | 121 |
| Figure 6.3 | Atmospheric attenuation of the propagated waves for six atmospheric conditions at the sea level (taken from [3]) | 123 |
| Figure 6.4 | Proposed transmitter chain architecture of the 300 GHz System showing the layered view of the components based on the rectangular waveguide structure [16] | 125 |
| Figure 6.5 | 3D view of Slotted waveguide antenna, (b) Antenna under test (taken from [26]) | 128 |
| Figure 6.6 | (a) 3D view of the Fabry Perot cavity antenna, (b) The actual antenna (taken from[27]) | 128 |

| | | |
|-------------|--|-----|
| Figure 6.7 | 3D layout of the narrow-wall 8×8 slotted waveguide antenna | 129 |
| Figure 6.8 | Variation of of the simulated directivity, realised gain and return loss of of the proposed antenna versus frequency | 131 |
| Figure 6.9 | Simulated radiation patterns of the proposed antenna for E- and H-planes at three frequency points including the centre frequency | 132 |
| Figure 6.10 | Complete structure of the proposed 8×8 slotted waveguide antenna, including the brass plates and the required wholes for the interconnection with the waveguide flange | 134 |
| Figure 6.11 | Effects of the brass plates on the simulated frequency performance of the proposed antenna | 134 |
| Figure 6.12 | Photograph of the fabricated 8×8 slotted waveguide antenna | 134 |
| Figure 6.13 | Diagram of the designed HBR slot with the characterisation of the three matching steps. $b = 0.432$ mm, $d = 0.96$ mm, $a = 0.864$ mm, $D_1 = 0.699$ mm, $D_2 = 0.499$ mm, $D_3 = 0.469$ mm, $M_1 = 0.24$ mm, $M_2 = 0.60$ mm, $M_3 = 0.91$ mm | 136 |
| Figure 6.14 | Variation of S_{11} , realised gain, and directivity of the HBR slot versus frequency | 137 |
| Figure 6.15 | Radiation pattern of the designed HBR slot at three different frequencies for both E- and H-planes | 137 |
| Figure 6.16 | Layout of an 8-slot travelling array cut in the centre of the narrow wall of the waveguide based on the micromachining layers (equal thickness $t=0.288$ mm). An H-plane bend is integrated with the structure to interconnect with the waveguide flange (WR-03) precisely, and an H-plane radiating slot is designed in order to cancel the reflected power to the input port. The outstanding structure in the central area represents the hollow waveguide WR-03 and slots, while the surrounding conductors are set to be transparent). $a = 0.864$ mm, $b = 0.432$ mm, $d = 0.964$ mm, $S_w = 0.15$ mm, $S_1 = 0.55$ mm | 138 |

| | | |
|-------------|--|-----|
| Figure 6.17 | (a) Simulated radiation pattern of the 8-slots at operating frequency 300 GHz for both E- and H-planes, (b) variation of the antenna return loss, directivity, and realised gain over the whole operating frequency band | 139 |
| Figure 6.18 | Normalised H-plane radiation pattern of an 8-slotted waveguide array with the variation of operating frequencies from 255 to 325 GHz. The total beam scanning is 20° over a 23.3 GHz fractional bandwidth | 140 |
| Figure 6.19 | CST model of the assembled antenna. The holes are for the necessary screws to connect the antenna with the WR-03 waveguide flange | 141 |
| Figure 6.20 | Effects of the brass plates on the simulated frequency performance of the proposed antenna | 141 |
| Figure 7.1 | (a-g), Design steps for the 7 th order 4 × 4 <i>antenna array-filter</i> component, (h) the whole topology | 149 |

List of Tables

| Tables | Title | page no. |
|---------------|--|---------------------|
| Table 2.1 | Physical design parameters of 8 slot antenna array cut in the broad-wall of a WR-90 waveguide | 30 |
| Table 2.2 | Summary of the electrical performance of the antenna | 31 |
| Table 2.3 | Physical design parameters of 8 slot antenna array cut in the narrow-wall of a WR-90 waveguide | 33 |
| Table 2.4 | Summary of the electrical performance of the antenna | 33 |
| Table 3.1 | Electrical specification of the 3 rd order rectangular waveguide WR-90 cavity filter | 54 |
| Table 3.2 | Physical dimensions of the 3d order coupled-resonator waveguide filter shown in Figure 3.13 operated at frequency range (8-12 GHz) | 60 |
| Table 4.1 | Physical dimensions of the 3 rd order <i>antenna-filter</i> component shown in Figure 4.1 (b) | 76 |
| Table 5.1 | Comparison between the electrical and physical specifications of the components given in the Table | 107 |
| Table 5.2 | Comparison between the electrical and physical specifications of the components given in the Table | 118 |
| Table 6.1 | Physical dimensions of the planar array 8×8 slotted waveguide antenna | 130 |
| Table 6.2 | Electrical parameters of the planar array 8×8 slotted waveguide antenna | 131 |

List of publications

- 1- Rashad H. Mahmud, Tianhao He, Michael Lancaster, Yi Wang, Xiaobang Shang, "Micromachined Travelling Wave Slotted Waveguide Antenna Array for Beam-Scanning Applications", *Antennas and Propagation Conference (LAPC)*, 2014 Loughborough, UK.
- 2- Rashad H. Mahmud, Michael Lancaster, Fred Huang, "High gain, wide bandwidth, filtering antennas based solely on resonators", *IEEE Trans. Antennas and Propag.* (In preparation).
- 3- Rashad H. Mahmud, Michael Lancaster, Fred Huang, "Synthesis of planar array waveguide aperture antennas using coupling matrix approach", *IEEE Trans. Antennas and Propag.* (In preparation).
- 4- Rashad H. Mahmud, Michael Lancaster, Fred Huang, "300 GHz planar array micromachined SU-8 based slotted waveguide antenna", *IET Microw. Antennas and Propag.* (Waiting for measurement).

Chapter 1

Introduction

This chapter is intended to highlight the main objectives of this thesis which can be summarised into: (i) the development of the coupling matrix approach to integrate antennas with bandpass filters, and (ii) the design of 300 GHz waveguide antennas based on the micromachining technique.

1.1 Research motivation and objectives

The Heinrich Rudolf Hertz's experiment in 1887 to investigate the electromagnetic radiation is known as the first practical antenna experiment [1, 2]. It was later developed in 1901 by Marconi to build a radio communication link between England and Newfoundland [2, 3]. Since then, there have been many wireless systems developed such as the Global Position System (GPS), Satellite communication, tracking radar, television and radio broadcasts etc.[4]. All types of information like pictures, speech, music and texts are transmitted from one place to another these days through the use of wireless communication systems without any physical connections, no matter where these places are. This thesis focuses on a terahertz communication system and its components, particularly the antenna and the front end bandpass filter.

A terahertz wireless communication system, which is proposed and investigated in the

Emerging Device Technology (EDT) research group at the University of Birmingham, is shown in Figure 1.1. The purpose of the system is to build a communication link and to be able to transfer data within the range of a 10 metres distance with the data rate around 10Gbps at a centre frequency of 300 GHz. To achieve this, the system needs to have a high gain antenna with a wide bandwidth. This thesis concentrates predominantly on the design of an antenna, which can meet such specifications.

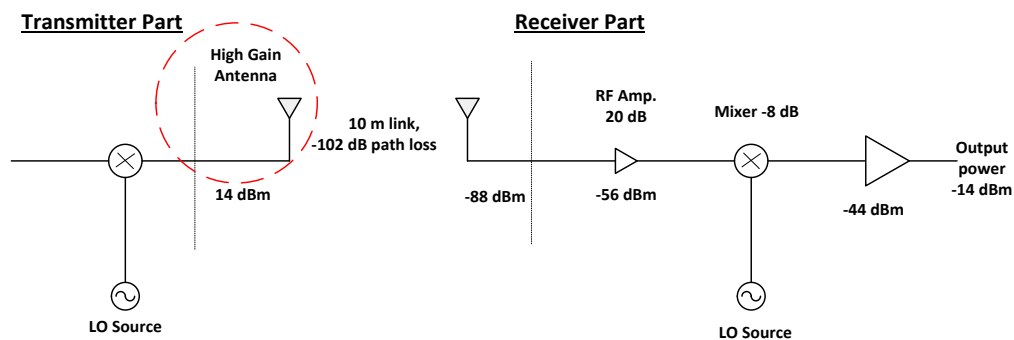


Figure 1.1: A simplified terahertz communication link budget diagram. All the components of the system are to be fabricated using micromachined layers.

It can be noticed from the specification of the terahertz system that the antenna is required to provide high gain and wide bandwidth. It is obvious that the increase of the antenna gain can be accomplished by an increase in the number of radiating elements and the antenna size[2]. However, the required bandwidth for the antenna with such a high gain value is a challenge. Enhancing the antenna bandwidth has been the subject of research for many decades [5-10]. In this thesis, a new approach has been presented to design antennas that can provide high gain and wide bandwidth.

The new design approach presented in this thesis is based on coupling matrix theory which can represent and synthesis the antenna in the form of the coupling matrix formulation. The parameters of the matrix, such as external quality factors (Q_{ei}), radiation quality factor (Q_{rj}) and coupling coefficients (M_{ij}) are capable of controlling the bandwidth of the antenna. The antennas produced from using this approach, which will also have a filtering functionality, is named *antenna-filter* component (single radiating element). The design approach has been developed further to expand the *antenna-filter* component to the *antenna array-filter* component (multiple radiating elements) so as to accomplish the high gain value simultaneously with the wide bandwidth.

With the use of the new design approach, five important features can be achieved for the components and the communication system. These are: (i) controlling the bandwidth of the antenna, (ii)controlling the gain of the antenna, (iii) reducing the size of the communication system because the bandpass filter component is no longer required to be placed after the antenna in the system due to the filtering functionality of the antenna, (iv) enhancing the performance of the communication system by overcoming the degradation caused by the mismatch between the bandpass filter and the antenna, and (v)scalability of the antenna circuits to terahertz frequencies (300 GHz and above). We will be able to recognise some of the features mentioned above in Chapters 4 and 5.

1.2 Thesis Organisation

This thesis is organised into seven Chapters, and high gain and wide bandwidth antennas dominate its main theme.

In the first section of Chapter 1, attention was given to the components of the proposed terahertz wireless communication system, particularly those which are placed at the very front-end of the systems such as the antenna and the bandpass filter. Not only the specification of the antenna was discussed, but also a new design approach was discussed so as to achieve it. Advantages of the new approach were given at the end of the section. In section 1.2, an overview of the whole thesis is given.

Chapter 2 explains the basic concept of radiation occurrence in antennas. High gain and wide bandwidth antennas are overviewed, and their limitations are addressed according to Chu-Harrington and Fano criteria. Also, details regarding the concept of operating slots in the walls of waveguide are mentioned. Two designs of slot arrays based on rectangular waveguides (WR-03) are presented.

In Chapter 3, the fundamentals of filter theories are described. The theories help us to understand the main theme of the integration of an antenna with a bandpass filter. The coupling matrix theory, which is used to represent the coupled-resonators circuits, is discussed, describing the parameters of the matrix (Q_{ei} , Q_{rj} and M_{ij}) and extracting them from their physical structure using rectangular waveguides. The extraction of the radiation Q_{rj} based on the cavity resonator is discussed, and ways to control the Q_{rj} value are addressed.

Chapters 4 and 5 present six designs of antennas all based on waveguide cavity resonators.

The design of the antennas is explained step by step, and comparisons between their initial and optimised responses are shown. Measurements for the antennas are performed for the purposes of validation.

Chapter 6 gives a brief overview of terahertz communication systems. Applications of terahertz frequency band are summarised, specifying the advantages and disadvantages of the frequency band in a communication system. The block diagram of the terahertz communication system, which is proposed to be built out of the micromachined technology, is shown. Then, design of a planar antenna which could be integrated with the system is presented. Additionally, another antenna is proposed for beam scanning applications at terahertz frequency band.

Chapter 7 presents the conclusions of this research work. Suggestions for further investigations on integration of antennas with bandpass filters are given. For this purpose, some suggested topologies are and required techniques are pointed out.

1.3 References

1. Huang, Y. and K. Boyle, *Antennas: from theory to practice*. 2008: John Wiley & Sons.
2. Kraus, J., *Antennas since hertz and marconi*. IEEE Transactions on Antennas and Propagation, 1985: p. 131-137.
3. Carnedevol, *First Atlantic Ocean crossing by a wireless signal*. Retrieved from <http://www.carnetdevol.org/Wireless/marconi-transatlantique.html>, 2015.
4. Pozar, D.M., *Microwave engineering*. 2009: John Wiley & Sons.
5. Chu, L.J., *Physical Limitations of Omni-Directional Antennas*. Journal of applied physics, 1948. **19**(12): p. 1163-1175.
6. Fano, R.M., *Theoretical limitations on the broadband matching of arbitrary impedances*. Journal of the Franklin Institute, 1950. **249**(1): p. 57-83.
7. Carlin, H., *Theoretical Limitations on the Broad-Band Matching of Arbitrary Impedances*. Circuit Theory, IRE Transactions on, 1961. **8**(2): p. 165-165.
8. Harrington, R.F., *Effect of antenna size on gain, bandwidth, and efficiency*. J. Res. Nat. Bur. Stand, 1960. **64**(1): p. 1-12.
9. Yusuf, Y. and X. Gong, *Integration of three-dimensional high-Q filters with aperture antennas and bandwidth enhancement utilising surface waves*. IET Microwaves, Antennas & Propagation, 2013. **7**(7): p. 468-475.
10. Ludlow, P., et al., *Applying band-pass filter techniques to the design of small-aperture evanescent-mode waveguide antennas*. Antennas and Propagation, IEEE Transactions on, 2013. **61**(1): p. 134-142.

Chapter 2

Basic concept of antennas

This chapter presents the basic concept of radiation from antennas. High Gain and Wide Bandwidth antennas are reviewed, and their limitations are addressed. Some design techniques presented in the literature for the calculation of an antenna gain and bandwidth (radiation Q) are discussed. Then, the properties of rectangular waveguides when used as transmission lines are characterised. Later, attention is paid to slotted waveguide antennas due to the fact that they are considered one of the most appropriate candidates for the proposed terahertz communication system. The fundamental concept of operating slots in the walls of rectangular waveguides is discussed, and the synthesis method steps presented in literature to design slots are given in this chapter. In the light of these steps, two designs for waveguide slot antennas are simulated at 300 GHz, and their performance is characterised.

2.1 Introduction

Antennas may be defined as one-port electrical devices used in wireless communication systems to deliver guided energy from the source to free space or vice versa. The delivery of the guided energy can be accomplished in the form of radiation. It is therefore worth explaining how the radiation occurs. To simplify this, a single electric charge is used in [1] as an example, and is shown in Figure 2.1. It is assumed that the electric charge with a constant velocity moves along the z -axis and reaches point A. At that point, the static electric lines

spread out from the charge radially. The circle created by the radius r_A is referred to the radial electric field lines when the electric charge is at point A. When the charge is accelerated, it starts moving towards a point denoted by B. Again at this point, the static field surrounding the electric charge is also radially spread away from the charge. The circle created by the radius r_B represents the electric field lines when the electric charge is at point B. The distance between the circles r_A and r_B is denoted by Δr . In the area located between the two circles, the electric field lines interact with each other and then a radiation would occur inside. If the electric charge is continuously accelerated backwards and forwards (oscillation), a continuous radiation can yield. More details about radiation occurrence in antennas can be found in [1-3].

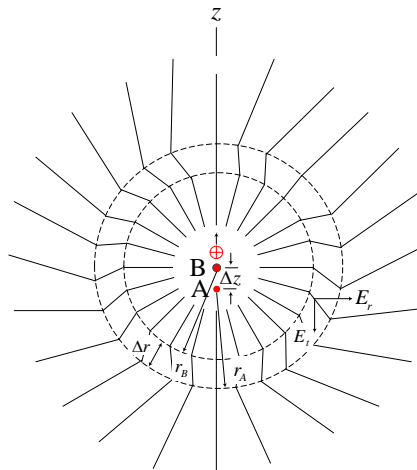


Figure 2.1: An electric charge moves towards point A and then, it is accelerated towards point B (re-drawn from [1]).

As discussed above, a power generator (source) is required in order to keep electric charges accelerating. Figure 2.2 shows a communication link where a generator on the left side has connected to the two-wire transmission line in order to guide energy as an electromagnetic (EM) wave. At the termination, the two-wire line is flared out and support the EM wave to start radiating [2]. The flared out section is called a transition or an antenna.

An antenna can be represented in the form of a circuit as shown in Figure 2.3. The antenna is

connected to the source. The source has impedance ($Z_s = R_s + jX_s$), where R_s is the source resistance and X_s is the source reactance. The antenna has also its own impedance ($Z_a = R_r + R_l + jX_a$). Here, R_r is the radiation resistance of the antenna, R_l is the loss resistance of the antenna, and X_a is the reactance of the antenna. When they are matched ($Z_s = Z_a$), maximum power generated from the source can be launched into space.

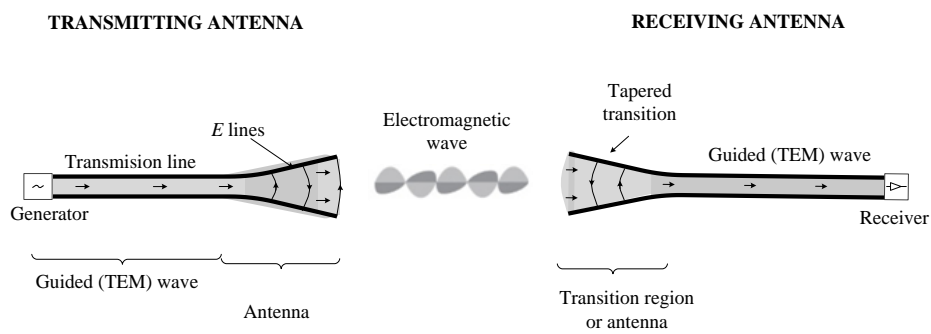


Figure 2.2: A communication link including a transmitting antenna and a receiving antenna. The transmitting antenna radiates. The radiated waves are in the form of spherical waves. As they propagate over a large distance, the waves change and become approximately plane waves. This diagram is reproduced from [2].

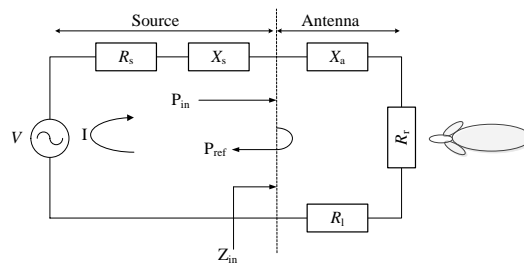


Figure 2.3: Equivalent circuit representation of a transmitter antenna [3].

Antennas can be categorised according to their radiation performance parameters such as high gain antennas and wide bandwidth antennas. They can also be classified based on their physical structure such as: wire antennas, aperture antennas, microstrip antennas, reflector antennas and lens antennas. Different physical structures of antennas can provide different

radiation performance. Because the proposed terahertz communication system seeks for a high gain and wide bandwidth antenna, and is made with a planar structure in order that it can be built out of the micromachined layers, the following sections will focus on those antennas which can meet these specifications.

2.2 High gain antennas

High gain antennas, which are sometimes known as directional antennas, are antennas which are able to direct most of the transmitted power towards the receivers when operating as transmitter antennas. These antennas are mainly used for long-range and space mission applications.

Enlarging the antenna physical aperture, which means enlarging the area of an antenna used to transmit the guided waves from the source through space and/or to capture the propagated waves from space at reception, can be considered as an approach to increasing the antenna gain [3]. Horn and parabolic dish antennas are two examples of aperture antennas. Figure 2.4 shows a parabolic dish antenna with diameter of 70 metres [4]. Its main use is for space missions. The curvature shape and the external feeding technique are considered the main drawbacks of parabolic dish antennas especially for the application of interest here due to occupying larger space.

An antenna array, which usually consists of a set of identical radiating elements, is another approach mainly used to (i) provide an overall gain of the array which is higher than the gain of the single radiating element [3], and (ii) to steer the main beam direction towards the receiver [5, 6]. The radiating elements of an antenna array can be dipoles, slots, patches, loops, reflectors, etc. The distribution of the radiating elements configures the shape of the radiation

characteristics of the antenna arrays.

A linear array, which means all the radiating elements are positioned along a linear axis, is able to produce Endfire and broadside arrays. The produced radiation pattern of an Endfire array is parallel to the axis containing the antenna. The axial mode helical antenna, which is an example of a high gain Endfire array, is of interest in space applications due to also having circular polarisation and wide bandwidth as well as being simple [2]. Figure 2.5 shows an array of four axial-mode helical antennas. This is used as the antenna for satellite tracking acquisition in France [7]. The main disadvantage of helical antennas at millimetre wave frequencies is the three dimensional structures which are difficult to fabricate and costly.

A planar array antenna is another configuration where all the radiating elements are spread over a planar surface and the radiation pattern is usually perpendicular (broadside) to the axis of the antenna. Fabry-Perot leaky wave antennas and slotted waveguide antennas are two examples of such arrays. Figure 2.6 shows a planar array slotted waveguide antenna employed in the radar system of the airplane Boeing 737 [8]. Recently, significant attention has been paid to slotted waveguide antenna arrays at millimetre wave frequencies due to (i) their planar structure, (ii) high gain, and (iii) inherent low losses in the waveguides [9-11]. The narrow bandwidth is the main concern with slotted waveguide antennas, and extensive investigations have been conducted in order to enhance the bandwidth of this antenna [12, 13]. More details about the theory of slotted waveguide antenna arrays will be given in Section 2.5.

Although the gain of an antenna can be increased with one of the approaches discussed above, no indication has been presented about the maximum achievable antenna gain so far. The following section gives brief details about the limitation of the maximum achievable antenna gain.



Figure 2.4: A parabolic 70 m dish antenna is used in the Goldstone Observatory station, Mojave Desert, California, USA [4].



Figure 2.5: An array of four axial-mode helical antennas, France [7].



Figure 2.6: A planar array slotted waveguide antenna is used in the radar system in the NASA Boeing plane 737 [8].

2.2.1 Antenna gain limitation

This section discusses the limitation of an antenna gain and its relationship to the antenna size. The discussion, which will be carried out here, is mainly based on Chu and Harington's work from 1948 and 1960 [14, 15], respectively.

In 1947 Wheeler [16] defined an electrically small antenna as the antenna where its maximum dimension (a_0) is smaller than $(1/k_0)$, where $k_0 = 2\pi/\lambda$ is the wave number related to the electromagnetic field, λ is the free space wavelength, and a_0 is the smallest radius of the sphere containing the antenna, as shown in Figure 2.7 (a). Chu in his theory found that the gain of an antenna, whose maximum dimension is $2a_0$, is equal to or less than $4a_0/\lambda$ [14]. According to Chu's theory, the gain can still be increased if the radiation Q of an antenna becomes larger [14].

Later Harington [15] developed Chu's theory, and presented a theoretical analysis regarding the influence of antenna size on antenna gain. He then realised that there is no limit to increasing the gain of an antenna if the size is increased. For the far-field zone, he derived an equation for the maximum achievable antenna gain in terms of antenna size as given below [15]:

$$G_{max} = (k_0 a_0)^2 + 2(k_0 a_0) \quad (2.1-a)$$

where, a_0 is the radius of the sphere containing the antenna, and k_0 is the wave number. The variation of the maximum achievable gain versus the antenna size using equation 2.1 is plotted in Figure 2.7 (b). One can see that the increase in antenna size leads to the increase in maximum antenna gain.

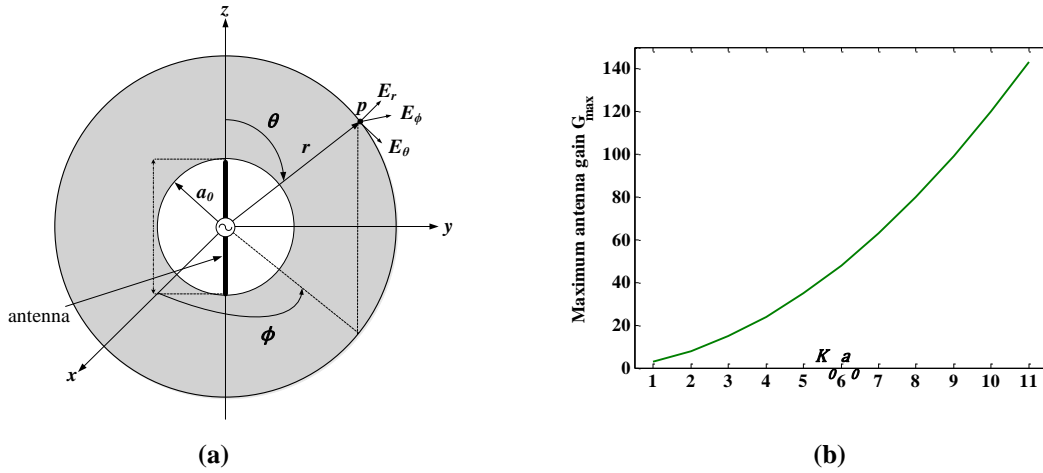


Figure 2.7: (a) An antenna placed in a spherical coordinate system, (b) The variation of the maximum antenna gain versus different antenna sizes.

The analysis given above is more appropriate to investigate the gain of the small 3-D antennas.

There is another relation that links the gain of a lossless antenna to its effective aperture as given below [3];

$$G = \frac{4\pi}{\lambda^2} A_{eff} \quad (2.1-b)$$

where, λ is the free space wavelength, and A_{eff} is the effective aperture of the antenna. It can be noticed that the gain is directly proportional to the effective aperture, and this equation is more preferable to investigate the gain of those antennas that have planar structures.

In practice, all types of antennas, if they have the same size, can actually provide different gain values. Some types of antennas can provide higher gain than others. This depends on the physical structure of antennas. Some physical structures can excite a higher number of spherical modes than others. Exciting a higher number of spherical modes leads to an increase in the antenna gain [17].

2.3 Wide bandwidth antennas

Wide bandwidth antennas are antennas which are able to operate over a wide range of frequencies. Most of the energy, which is guided by the wide bandwidth transmitter antennas, radiates to space and less is stored around the antenna and reflecting back to the input port (source). The antenna radiation quality factor (Q) is a parameter which defines the relationship between the time average stored energy and the energy radiated by the antenna. It can mathematically be expressed as follows [18]:

$$Q = \begin{cases} \frac{2\omega W_e}{P_{\text{rad}}}, & W_e > W_m \\ \frac{2\omega W_m}{P_{\text{rad}}}, & W_m > W_e \end{cases} \quad (2.2)$$

Here W_e and W_m are the electric and magnetic time average stored (non-propagating) energy, and P_{rad} is the power radiated by the antenna.

Horn and Vivaldi antennas are the antennas which usually provide wide bandwidth. As can be seen in Figure 2.8 (a) the horn antenna has a uniform waveguide section. The flared section is introduced in order to match the impedance of the waveguide to the impedance of free space [2]. Also, the length of the flaring can control the bandwidth of the antenna. Although horn antennas have wide bandwidth and high gain as well, they are less preferred for millimetre and terahertz communication applications because the flared out section is difficult to fabricate.

Vivaldi antennas are also another type of wide bandwidth antennas. They can radiate over a wide range of frequency because of the gradual taper of the slot aperture as shown in Figure 2.8 (b). The narrow part of the slot aperture supports radiation at higher frequencies, while the wider slot aperture supports the radiation at low frequencies [19]. This provides a smooth

transition between the antenna and free space. Due to the increase in losses in the microstrip at high frequencies and the complexity of the tapering shape of the aperture, this kind antenna is not of interest for terahertz communication systems.

There are many investigations conducted into the fundamental limitations of antenna radiation Q and bandwidth in the literature. In the following section, some of these limitations will be discussed.

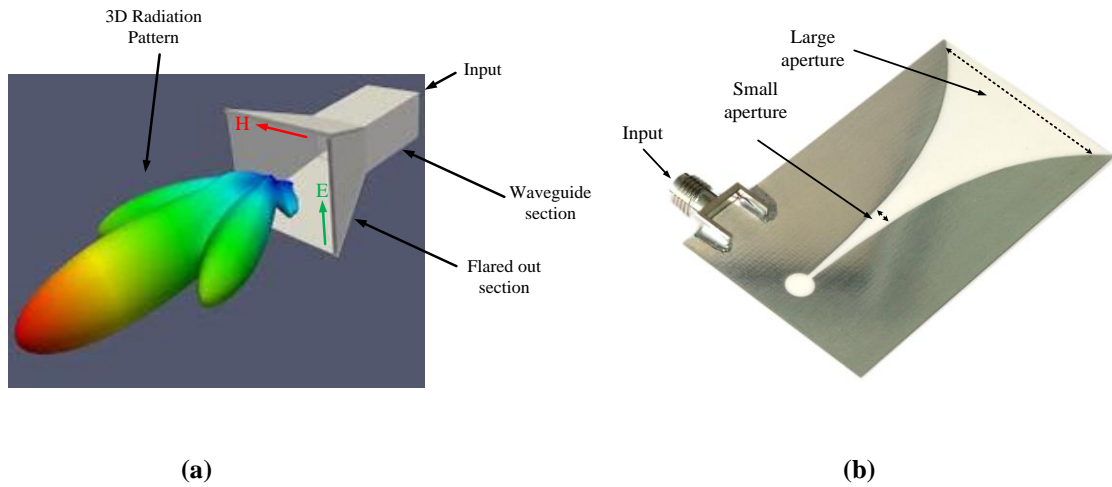


Figure 2.8: (a) A Pyramidal horn antenna with its 3-D radiation pattern [20], (b) A Vivaldi antenna [21].

2.3.1 Antenna bandwidth limitation

Bandwidth is one of the important parameters of an antenna. It is associated with the antenna radiation quality factor Q . As explained in Section 2.1, an antenna can be represented in the form of a circuit (Figure 2.3). When the antenna resonates at a particular frequency f_0 , the fractional bandwidth of the antenna B , (when assuming no conduction and dielectric losses existed), maybe computed as the inverse of the radiation Q , as follows [3, 18]:

$$B = \frac{1}{Q} \quad (2.3)$$

here B is the fractional bandwidth of the antenna, and can be expressed as follows:

$$B = \frac{f_h - f_l}{f_0} \quad (2.4)$$

where f_h and f_l are the edge frequencies of the band of interest, as shown in Figure 2.9. The centre frequency f_0 is the frequency where the antenna resonates. Looking at Equation 2.3 from a different point of view, the bandwidth can be obtained if the radiation Q of the antenna is known.

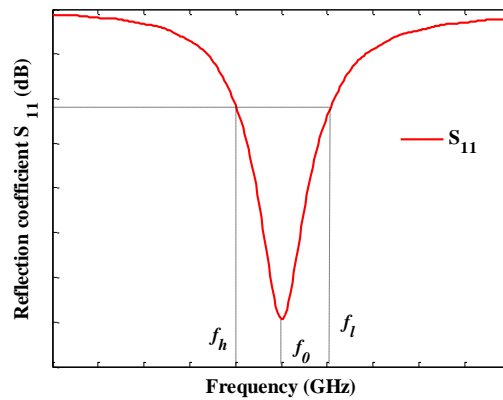


Figure 2.9: The Reflection S_{11} parameter of an antenna.

The first investigation into the radiation characteristics of an electrically small antenna was conducted in 1947 by Wheeler [16]. He worked on the radiation power factor of inductors and capacitors when used as radiators. Following this, Chu in 1948 derived an equation (Equation 2.5) to calculate the minimum radiation quality factor in terms of an antenna size for an Omni-directional antenna placed in the sphere of radius a_0 (Figure 2.7 (a)) [14]. He had assumed that the minimum radiation Q would occur if all the energy stored is located outside the sphere, and all of it is propagated. The theory was established for those antennas which are linearly polarised. Harrington later expanded the theory to include circularly polarised antennas[15]. In 1964 and 1969, Collin [22] and Fante [23] presented a new approach, which

was based on the specific energy named ‘evanescent energy’ stored around an antenna, to calculate the exact radiation Q . Later in 1996, McLean [24] realised that obtaining the minimum using Chu’s criterion is not accurate due to a failure to consider the energy stored outside the sphere which includes all the propagated and non-propagated waves. He derived a new equation (Equation 2.6) to calculate the minimum Q including non-propagating waves for a linearly polarised antenna.

$$Q = \frac{1 + 2(k_0 a_0)^2}{(k_0 a_0)^3 [1 + (k_0 a_0)^2]} \quad (2.5)$$

$$Q = \frac{1}{(k_0 a_0)^3} + \frac{1}{k_0 a_0} \quad (2.6)$$

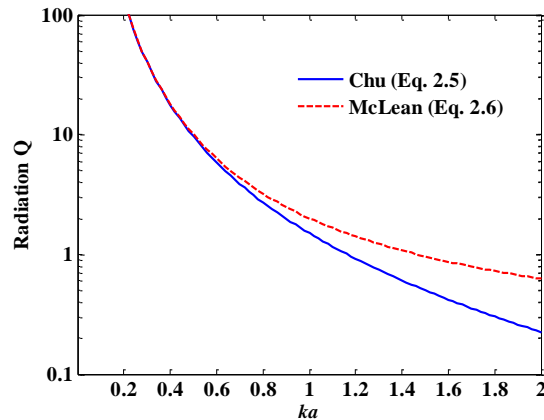


Figure 2.10: The variation of the radiation Q of a linearly polarised electrically small antenna versus the antenna size according to Chu and McLean’s criteria [24].

The variation of antenna radiation Q versus its size is shown in Figure 2.10 using both Chu and McLean equations. It can be seen that when the antenna size increases the radiation Q of the antenna decreases significantly. It can also be noticed that McLean’s approach is in good agreement with Chu’s approach when the antenna size is smaller than one ($ka_0 \ll 1$). However, when the size increases the difference between these two approaches becomes obvious. Actually, it is worth noting that both Chu and McLean’s approaches are dependent

on antenna sizes only for the calculation of the antenna radiation Q without taking the effect of matching circuits into account in the antenna system. Fano in 1950 presented a new criterion to deal with an impedance matching network used with a small antenna (load) (see Figure 2.11), and addressed the impact of the matching network on the performance of the antenna particularly antenna bandwidth [25, 26].

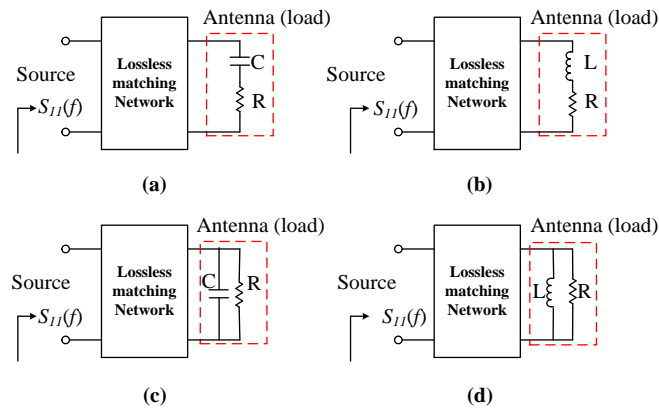


Figure 2.11: Four possible RC and RL circuits of a small antenna with a matching network: (a) RC is in series, (b) RL is in series, (c) RC is in parallel, and (d) RL is in parallel (This diagram is reproduced from[27]).

Fano discovered that there is a fundamental limit for the maximum achievable reflection bandwidth of an antenna when using a matching network in the antenna system. This maximum achievable bandwidth is expressed mathematically as follows [17, 25, 26]:

$$B = -\frac{1}{Q} \frac{\pi}{\ln(|S_{11}(f)|)} \quad (2.7)$$

Using the 3-dB bandwidth criteria (i.e. $|S_{11}(f)| = 1/\sqrt{2}$), Equation 2.7 reduces to:

$$B = \frac{9.06}{Q} \quad (2.8)$$

In comparison to Equation 2.3, the bandwidth of an antenna is enhanced according to Equation 2.8 by a factor of about 9.06. This enhancement occurs due to the employment of the matching network in the antenna system (increasing the bandwidth of the antenna system).

2.4 Waveguides

A waveguide is a transmission line used to guide electromagnetic energy from one point to another. Circular and rectangular are the common shapes of waveguides. Most attention here is paid to the rectangular waveguide, as shown in Figure 2.12, due to its simplicity in fabrication and wide use in the field of antenna design. The properties of rectangular waveguides are fully explained and presented in [28, 29], and, therefore, only the properties related to the waveguide antenna designs are discussed here.

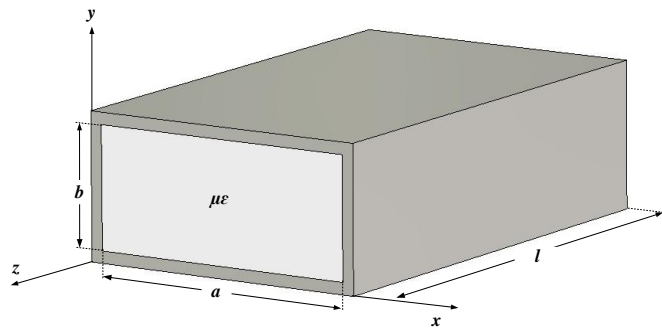


Figure 2.12: A rectangular waveguide geometry.

Unlike a transmission line supporting only the transverse electromagnetic (TEM) modes, rectangular waveguides can support both transverse electric (TE) and magnetic (TM) modes [29]. Each of the TE- and TM modes has a cut-off frequency. Below the mode cut-off frequency the propagation of electromagnetic waves inside the waveguide is not possible. However, if the waveguide is operated above the cut-off frequency then propagation takes place. The cut-off frequency of the modes in the rectangular waveguide can be calculated using the following relation [28]:

$$f_{c_{mn}} = \frac{1}{2\pi\sqrt{\mu\epsilon}} \sqrt{\left(\frac{m\pi}{a}\right)^2 + \left(\frac{n\pi}{b}\right)^2} \quad (2.9)$$

Here ε and μ are the permittivity and permeability of the material inserted into the waveguide respectively, m and n are the integer positive numbers and together they generate the TE_{mn} and TM_{mn} modes. Also, a and b are the waveguide dimensions as shown in Figure 2.12. The waveguide guided wavelength (λ_{gmn}) is always longer than the free space wavelength (λ_0), and can be computed for the TE_{10} mode using the following equation [28]:

$$\lambda_{g10} = \frac{\lambda_0}{\sqrt{1 - \left(\frac{\lambda_0}{2a}\right)^2}} \quad (2.10)$$

The dominant mode in a waveguide is defined as the mode which has the lowest cut-off frequency [29]. The first dominant mode of rectangular waveguides is the transverse electric TE_{10} mode, and the TE_{20} mode is referred to the second dominant mode. The frequency range between two neighbouring dominant modes can be considered as the useful bandwidth of a waveguide as highlighted in Figure 2.13. The b dimension of a waveguide is usually chosen to be equal to $a/2$ to keep the useful bandwidth of waveguides wide enough [30].

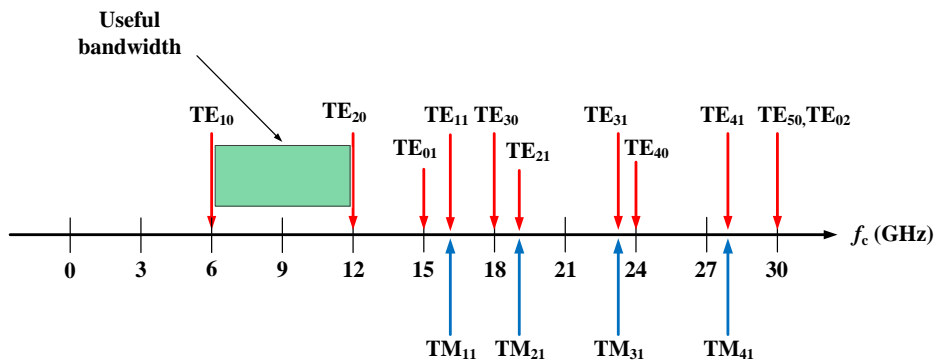


Figure 2.13: Configuration of cut-off frequencies of different propagated mode $a=25$ mm, $b=10$ mm air filled. The cut-off frequency is calculated using Equation 2.9 (This figure is re-produced from [29]).

The transverse electric field components (E_x, E_y), for a rectangular waveguide, of both TE_{mn} and TM_{mn} modes can be given as [28]:

$$\bar{E}_t(x, y, z) = \bar{e}(x, y)(A^+ e^{-j\beta_{mn}z} + A^- e^{j\beta_{mn}z}) \quad (2.11)$$

Here, $\bar{e}(x, y)$ represents the transverse variation of the mode in both x and y directions, and A^+ and A^- are the amplitudes of the waves propagating forward and backward. The propagation constant β_{mn} , for both TE_{mn} and TM_{mn} modes, is [28]:

$$\beta_{mn} = \sqrt{k^2 - \left(\frac{m\pi}{a}\right)^2 - \left(\frac{n\pi}{b}\right)^2} \quad (2.12)$$

Here, k is the wave number, and m and n are the positive integer numbers.

It is possible to obtain the surface current density (J_s) on the walls of a waveguide if the magnetic field is known [29]. Figure 2.14 shows a sketch of the current lines distributed on the walls of the rectangular waveguide for the TE_{10} mode. It is worth mentioning that the current lines do not cross the centre line at the broad wall of the waveguide. This offers an important practical feature in that waveguide can be cut at the centre of the broad wall without causing any losses [30]. It is also important to see from Figure 2.14 that the distribution of the current lines on the surface of the walls of the waveguide is not homogenous. When considering a waveguide slot antenna, in which the slots are usually cut out from the walls of the waveguide, slots interrupt the current lines. The more interruption of the current lines by the slots, the more excitation of the slots can result. Thus, it is important to determine where to place the slots in order to obtain maximum radiation. This will be discussed in detail in the next Section.

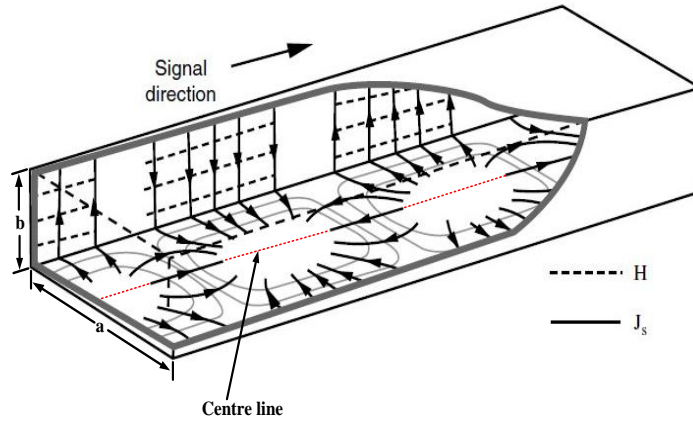


Figure 2.14: The distribution of the magnetic field and current lines on the walls of a rectangular waveguide operated at TE₁₀ mode (Taken from [31]).

The losses in the rectangular waveguide have not been addressed so far. There are two different kinds of losses existing in rectangular waveguides. The first one is the dielectric loss which is caused when a material is inserted into the waveguide. Since all the waveguides used for the antenna designs in this thesis are air filled, dielectric loss is not considered. Conductor loss is another type of loss in the waveguide which is produced from the material used to make the waveguide walls. This can be calculated as follow for the TE₁₀ mode [28, 29]:

$$\alpha_c = \frac{R_s}{a^3 b \beta k \eta} (2b\pi^2 + a^3 k^2) \text{ Np/m} \quad (2.13)$$

Here $R_s = \sqrt{\omega\mu_0/2\sigma}$ is the surface resistivity of the waveguide walls, σ is the conductivity, $k = \omega\sqrt{\mu\varepsilon}$ is the wave number, β is the propagation constant, and $\eta = \sqrt{\mu/\varepsilon}$ is the intrinsic impedance.

2.5 Waveguide antennas

As mentioned earlier, the main use of waveguides is to transfer energy from one point (source) to another (load). On the other hand, they can also be used to radiate energy into space if one of the ends of the waveguide is open to space, or if slots are cut in the walls of the waveguides. There are many configurations introduced to the geometry of waveguide antennas, such as waveguide slot and horn antennas, in order to (i) maintain the matching impedance between free space and the waveguide and (ii) to enhance the radiation characteristics of the waveguide antenna. The following Section focuses on slotted waveguide antennas.

2.5.1 Slotted waveguide antennas

A slot antenna is considered as one of the oldest types of antenna which dates back to 1946 when Booker investigated the relationship between the radiation characteristics of a half-wave slot cut in a thin flat sheet and a half-wave dipole antenna [32]. He realised that a slot acts as the complement to a dipole antenna, except that electric and magnetic fields are exchanged. As illustrated in Figure 2.15, the electric field is transverse to the longest dimension of the slot. However, it is parallel to the length of the dipole antenna.

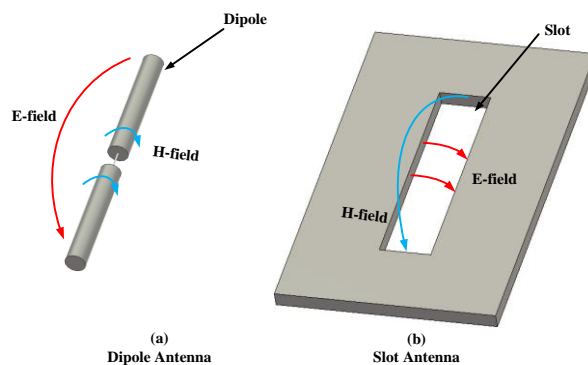


Figure 2.15: Illustration of the electric and magnetic fields of both dipole and slot antenna configurations.

Later in 1947, a pioneering investigation into slots fed by a waveguide was conducted by Watson [33]. The main purpose of Watson's investigation was to describe how a half-wavelength slot couples to a waveguide. He gave some design principles for this purpose. One year later Stevenson presented his theory of slots in the rectangular waveguide. The theory was based on field equations and some assumptions in order to simplify the calculation of the reflection and transmission coefficients. These assumptions, which have become the basics for the design of many types of modern waveguide slot antennas, are given below [34]:

- Perfect conducting of the walls of the waveguide and ignoring the effect of the thickness of the walls on the radiation characteristics
- Considering narrow slots to have a relationship to their length as given below

$$2 \log \left(\frac{\text{slot length}}{\text{slot width}} \right) \gg 1 \quad (2.14)$$

- Ignoring the effect of the fields which are behind the surface including the slots
- Assuming (H_{01} – wave (the EM propagation mode)) as the only transmitting wave from the waveguide, and that the slot length has about half-free space wavelength of the resonant frequency

As mentioned in the Section 2.4, radiations through the slots occur if they interrupt the surface current lines distributed on the walls of the waveguide. Interrupting the current lines produces a voltage across the slots where the peak value of the voltage locates at the centre of the slot, as it can be depicted in Figure 2.16. It is therefore important to determine where precisely to place the slots. Figure 2.17 shows a rectangular waveguide, where the TE_{10} mode is the only mode propagating in it with several slots cut into the walls of the waveguide. Due

to an absence of interruption in the surface current lines (see Figure 2.14 to observe the distribution of surface electric lines), radiation through slot (h) does not occur. The direction of slot (g) is the same as the direction of the current lines in the side-wall of the waveguide, which means no interruption of the current lines takes place, and radiation does not occur either. Further details about the remaining slots in Figure 2.17 and their behaviours can be found in [5].

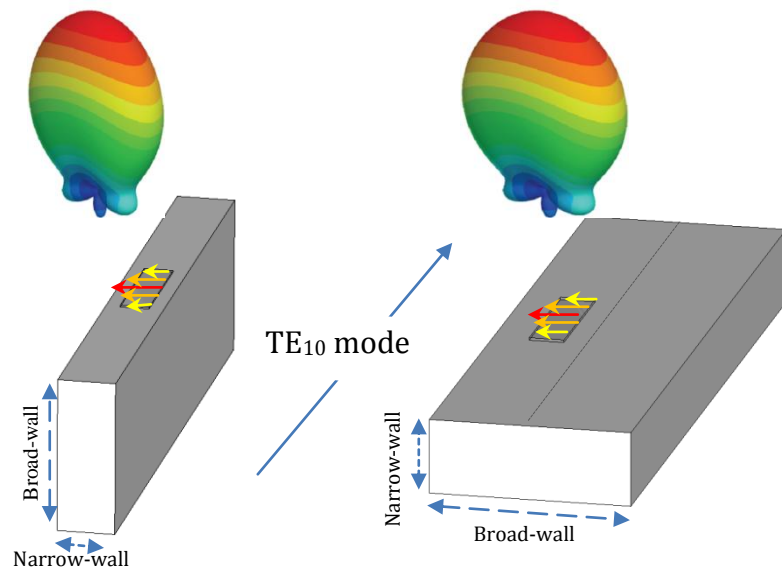


Figure 2.16: Broad and narrow walls slotted waveguide antennas with their aperture electric field distributions and predicted radiation patterns.

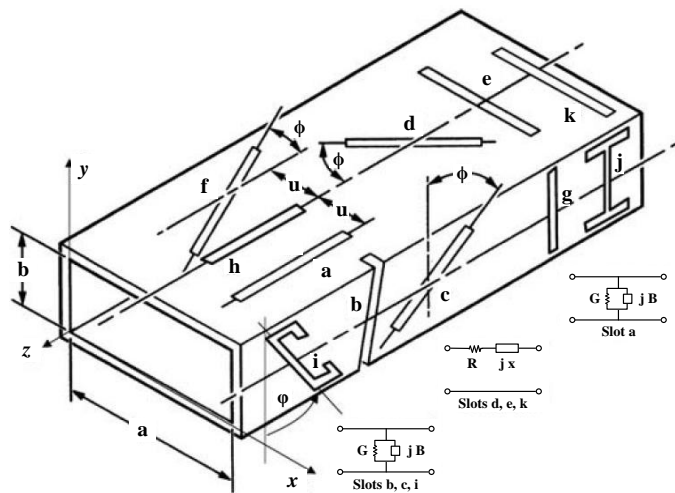


Figure 2.17: Some slots cut in the walls of the waveguide (Taken from [5]).

The slots in the broad-wall of waveguides have received significant attention from antenna designers. Stegen in 1952 was able to design longitudinal slots in the broad wall of a waveguide [35]. Oliner in 1957 presented a set of equivalent circuits in order to represent the slots in the broad-wall of waveguides (see Figure 2.18) [36]. He assumed that the slots could be represented as the shunt elements in the circuit. Using this assumption, he was able to calculate the conductance and resonant frequency of the slot antennas. Elliot and Kurtz [37] in 1978 revised one of the assumptions of Stevenson by assuming the slot length to be 2% less than a half wavelength. Again, in 1983, Elliot came back to the research and derived two equations to design linear and planar array waveguide antennas by taking the effect of mutual coupling between the slots into consideration [38]. From 1983 to 1990, Elliot's equations were improved and generalised by other researchers [39-42].

In the following sections, two designs of slots in the broad and side walls of rectangular waveguides, which operate at 300 GHz frequency, are presented. The design steps to obtain the electrical and physical parameters of the antennas are also clarified.

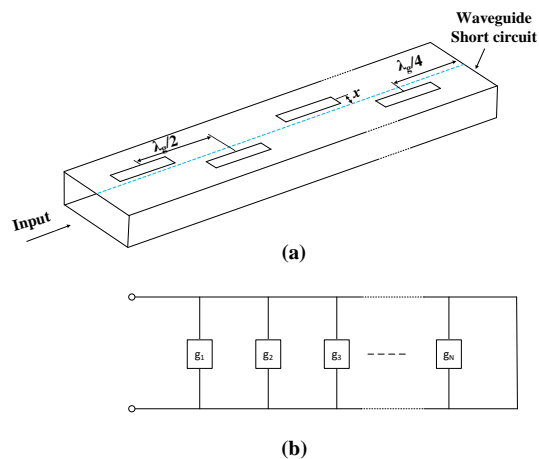


Figure 2.18: Longitudinal waveguide slot antenna with its equivalent circuit [36].

2.5.2 Design of linear array broad-wall slotted waveguide antennas

In this section, the design of a standing wave slotted waveguide linear array antenna is presented. The design steps detailed here will be used to the design of 8×8 slotted waveguide antenna in Chapter Six (Section 6.5). The antenna here is simulated at 300 GHz, and is completely compatible with multilayer micromachined techniques. As shown in Figure 2.19, the design consists of three layers of which the first layer includes 8 radiating slots. It should be noted that the depth of the slots (b_1) here, is associated with the thickness of the micromachined layers. This has an impact on the release of the energy radiated through the slots. The second layer forms the narrow walls of the waveguide, and the third layer is to enclose the whole design. To obtain the initial dimensions of the antenna, the following steps during the design of the antenna are undertaken:

- 1- The number of slots controls the gain and the beam width of the antenna. Here, 8-slots are chosen arbitrarily for the investigation.
- 2- Because the slots are designed to resonate at the centre frequency of 300 GHz and this is a standing wave array, the spacing between the slots is chosen to be half-guided wavelength ($d = 0.613$ mm).
- 3- The slots are displaced from the centreline of the broad-wall in order to interrupt the surface current lines. The displacement can be calculated using the normalised conductance equation as given below [34]:

$$g_n = 2.09 \frac{\lambda_g}{\lambda_0} \left(\frac{a}{b}\right) \left(\cos^2 \frac{\pi \lambda_0}{2\lambda_g}\right) \left(\sin^2 \frac{\pi x}{a}\right) \quad (2.15)$$

where a and b are more specific waveguide dimensions, λ_0 and λ_g are the free space and guided wavelengths, and x is the displacement. To obtain the value of x , it needs to be

assumed that all the slots in the array are matched with the input impedance. Under these circumstances, the normalised conductance can be defined in terms of the number of slots n as follows [5]:

$$g_n = \frac{1}{n} \quad (2.16)$$

After substituting the values of a , b , λ_0 , λ_g , and n into Equation 2.15, then the displacement x value can be found which is equal to 0.1590 mm.

4- According to Elliot [37], the length of the slots S_l having square corners is $0.464\lambda_0$ and their widths S_w are $0.05\lambda_0$ when the effect of the ground plane is not taken into account.

5- Because this is a standing wave array, the distance d_1 between the centre of the last slot to the waveguide termination is considered as a short circuit ($\lambda_g/4$). This leads the reflected waves back and contributes with the incident waves to radiation through the slot in phase. The physical design parameters of the antenna are summarised in table 2.1.

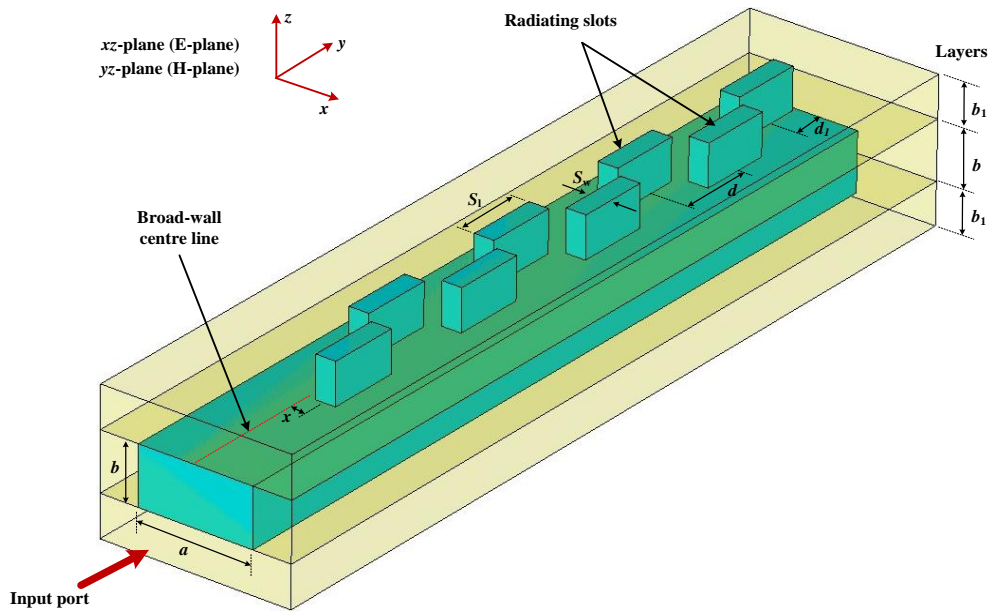


Figure 2.19: Layout of 8-slots cut in the broad-wall of the waveguide based on the micromachined layers ($a=0.864$ mm, $b=0.432$ mm, $b_1=0.300$ mm, other dimensions are given in Table 2.1). The outstanding structure in the central area represents the hollow waveguide WR-03 and slots, while the surrounding conductors are set to be transparent.

The initial performance of the designed antenna has been obtained using the computer simulation technology CST simulator [43]. The initial reflection coefficient S_{11} response of the antenna shown in Figure 2.20 (a) is not well matched at the designed frequency 300 GHz. This could be caused due to not considering the effect of (i) the waveguide wall thickness (b_1), (ii) the mutual coupling between the slots, and (iii) the ground plane. To improve the S_{11} response, tuning for the initial physical dimensions of the antenna is performed using the CST optimiser [43]. The goal for the optimiser is defined as follows: $S_{11} \ll -10$ dB, from 295-305 GHz. After optimising, an improvement in the response of the S_{11} is obtained (see Figure 2.20 (a)). The optimised dimensions are compared with the initial dimensions in Table 2.1.

The variations of directivity, realised gain, and the total efficiency of the antenna versus frequencies are shown in Figure 2.20 (b). The S_{11} response of the antenna is well matched after the optimisation over the frequency range 295-305 GHz, and as a result of that the directivity and the realised gain values are very comparable to each other around that frequency range. Moreover, the total efficiency, after including the losses caused due to the mismatch and the silver material used in modelling the antenna in CST, is more than 90%. Figure 2.21 shows the radiation pattern of the antenna in both the E- and H-planes at three different frequencies including the centre frequency. It can be seen clearly in Figure 2.21 (b) as the frequency increases, the side lobe level increases and the radiation pattern degrades. Electrical specifications of the antenna are summarised in Table 2.2.

Table 2.1
Physical design parameters of 8 slots antenna array cut in the broad-wall of a WR-90 waveguide

| Parameters | Calculated (mm) | Optimised (mm) |
|-------------------------------|-----------------|----------------|
| Slot length S_1 | 0.464 | 0.486 |
| Slot width S_w | 0.05 | 0.161 |
| Enter slot distance d | 0.613 | 0.631 |
| Slot offset x | 0.1590 | 0.130 |
| Last slot centre to end d_1 | 0.306 | 0.335 |

Table 2.2
Summary of the electrical performance of the antenna

| Parameters | Centre Frequency (GHz) | Gain (dBi) | Bandwidth (%) ($S_{11} = -10$ dB) | 3dB Beamwidth (deg.) | Side lobe level (dB) |
|------------|------------------------|------------|------------------------------------|----------------------|----------------------|
| E-plane | 300 | 14.1 | 5 | 113.0 | -14.1 |
| H-plane | | | | 9.9 | -10.1 |

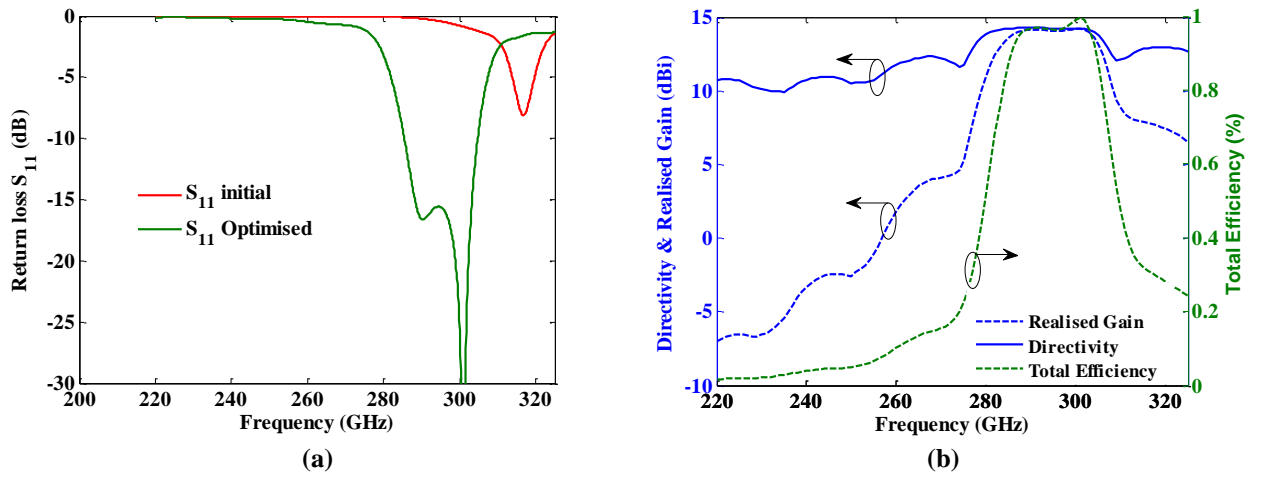


Figure 2.20: (a) The initial reflection coefficient response S_{11} (red line) in comparison to the optimised (green line), (b) Variation of the antenna directivity, realised gain, and total efficiency versus frequency.

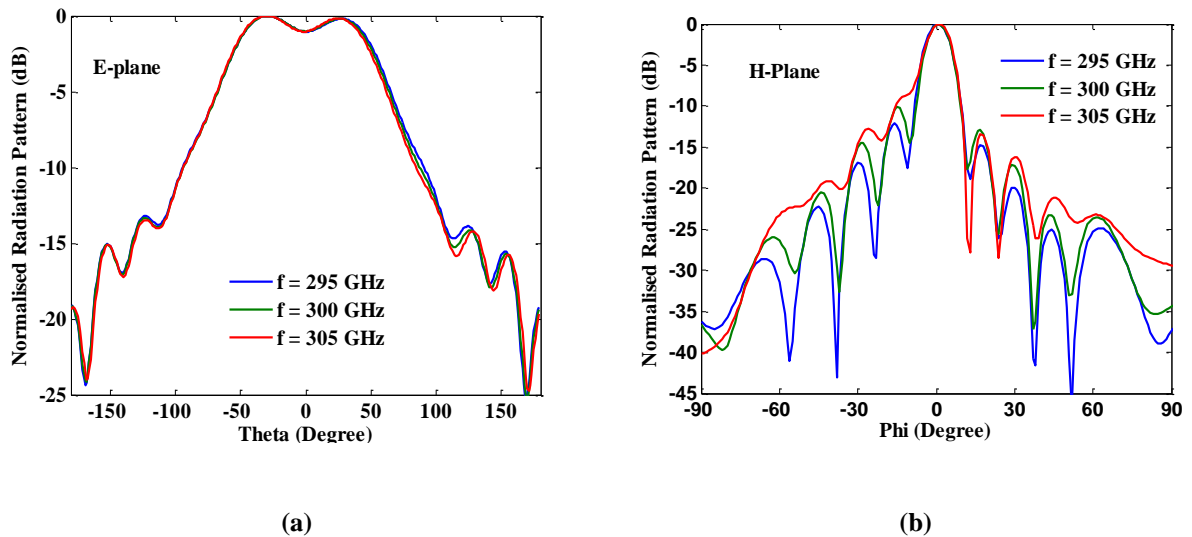


Figure 2.21: Simulated radiation pattern of the antenna in the E- and H-planes at three different frequencies including the centre frequency.

2.5.3 Design of linear array narrow-wall slotted waveguide antenna

This section demonstrates the design of narrow-wall slotted waveguide antennas at 300 GHz. A waveguide antenna with 8- radiating slots in the narrow-wall was already designed in [44] using four equal thickness layers. It is re-designed here to be built with five layers. The configuration of the design is shown in Figure 2.22. The top layer contains 8-radiating slots, and they are positioned at the centre of the narrow-wall of the waveguide. The next three layers form the rectangular waveguide.

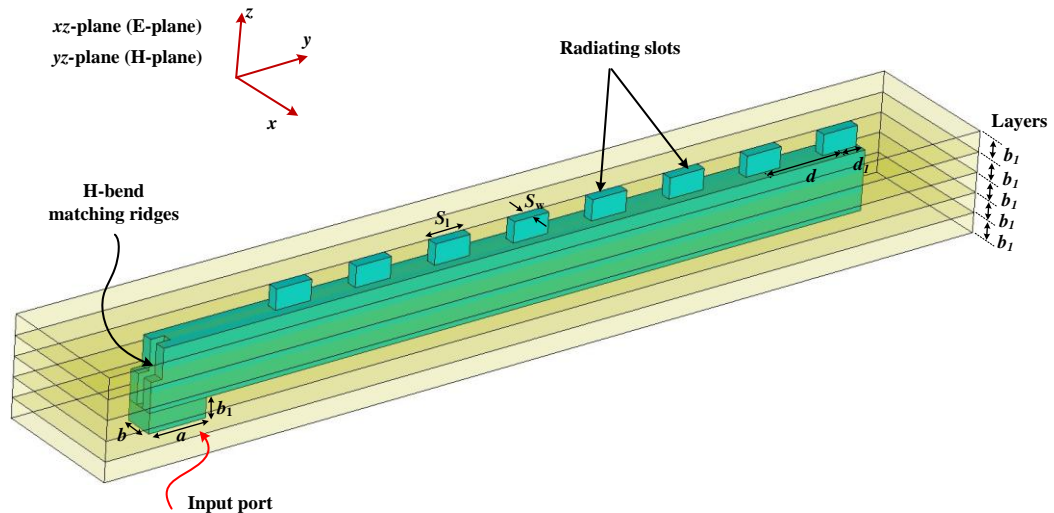


Figure 2.22: Layout of 8-slots cut in the narrow-wall of the waveguide based on the micromachined layers ($a=0.864$ mm, $b=0.432$ mm, $b_1=0.288$ mm). The outstanding structure in the central area represents the hollow waveguide WR-03 and slots, while the surrounding conductors are set to be transparent.

An embedded four-layered H-plane bend was designed in [45]. Here, the bend has been modified in order to be constructed out of five layers and to be consistent with the number of the layers of the antenna. The effect of the bend on the performance of the antenna is negligible due to good S_{11} matching of the bend around the centre frequency as can be seen in Figure 2.23.

In the previous section, the slots are located on the broad-wall and spaced approximately at a half guide wavelength ($\lambda_g/2$). However, in the design of slots in the narrow-wall, slot spacing is to be equal to one guide wavelength (λ_g) apart in order to keep exciting all the slots in phase (refer to Figure 2.14 to see the directions of the surface current lines and identify the phase changes at the narrow-walls of the waveguide). The initial dimensions of the slots here have been obtained following the design steps (1, 4, and 5) which were mentioned in the previous Section. Table 2.3 summaries some physical dimensions of the antenna.

Table 2.3
Physical design parameters of 8 slot antenna array cut in the narrow-wall of a WR-90 waveguide

| Parameters | Calculated (mm) | Optimised (mm) |
|-------------------------------|-----------------|----------------|
| Slot length S_1 | 0.464 | 0.552 |
| Slot width S_w | 0.05 | 0.149 |
| Enter slot distance d | 1.226 | 1.226 |
| Last slot centre to end d_1 | 0.306 | 0.328 |

Table 2.4
Summary of the electrical performance of the antenna

| Parameters | Centre Frequency (GHz) | Gain (dBi) | Bandwidth (%) ($S_{11} = -10$ dB) | 3dB Beamwidth (deg.) | Side lobe level (dB) |
|------------|------------------------|------------|------------------------------------|----------------------|----------------------|
| E-plane | 300 | 15.2 | 2 | 138.9 | -14.6 |
| H-plane | | | | 5.1 | -7.4 |

The initial response of the reflection coefficient S_{11} of the antenna is shown in Figure 2.24 (a). Again, it is not well-matched over the bandwidth of interest and thus an optimisation is performed for initial physical dimensions of the antenna using CST simulator [43]. The goal for the optimiser is defined as: $S_{11} \ll -10$ dB, from 295-305 GHz. The optimised dimensions of the antenna are summarised in Table 2.3. The directivity and realised gain responses versus

operating frequency band are plotted in Figure 2.24 (b) and it can be seen that their values are close to each other over the bandwidth of interest. More than 90 % total efficiency of the antenna from 297-303 GHz is predicted. The simulated radiation patterns of the antenna in both the H- and E-planes are presented in Figure 2.25 for three different frequencies including the centre frequency. The simulated antenna gain is 15.2 dBi at 300 GHz with two grating lobes appeared in the H-plane. Their appearance is due to the large spacing ($1 \lambda_g$) between the radiating slots. Further electrical specifications of the antenna can be found in Table 2.4.

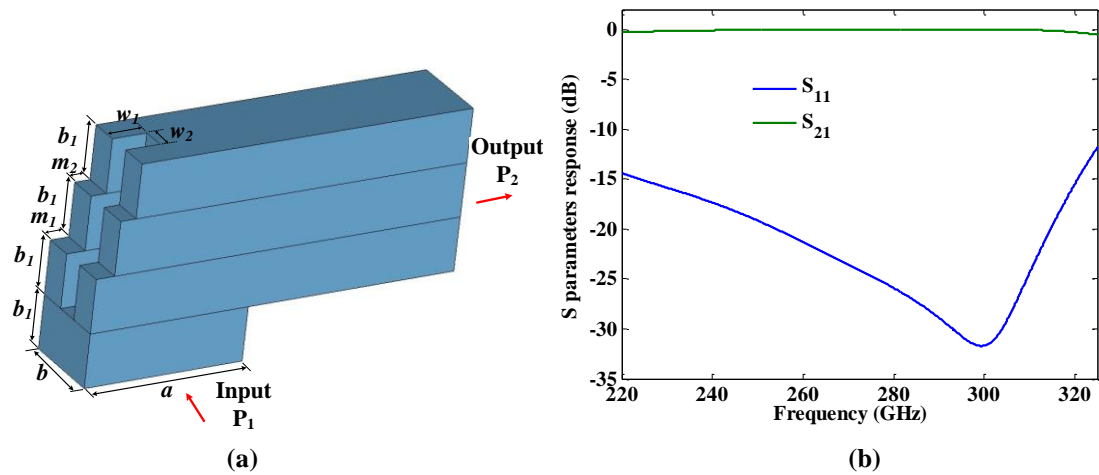


Figure 2.23: (a) The design of the WR-03 waveguide H-bend. The dimensions are; $a=0.864$ mm, $b=0.432$ mm, $b_1=0.288$ mm, $m_1=0.1$ mm, $m_2=0.083$ mm, $w_1=0.187$ mm, $w_2=0.139$ mm, (b) the simulated response of the bend.

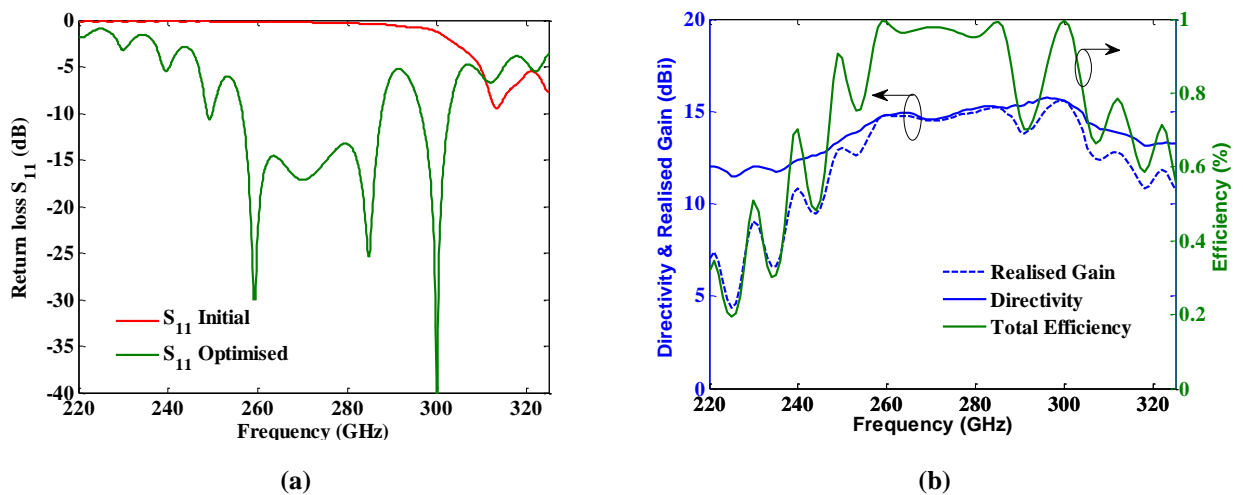


Figure 2.24: (a) Initial reflection coefficient response S_{11} (red line) compared to the optimised (green line), (b) Variation of the antenna directivity, realised gain, and total efficiency versus frequency.

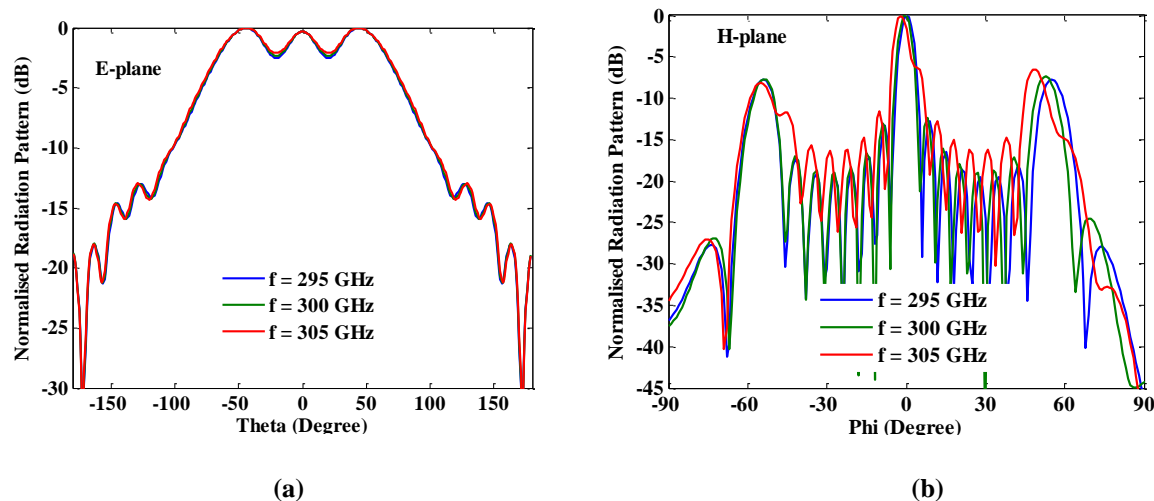


Figure 2.25: Simulated radiation pattern of the antenna in both the E- and H-planes at three different frequencies including the centre frequency.

2.6 Conclusions

This chapter has described the basic concept of radiation occurrence in antennas. High gain and Wide Bandwidth antennas were discussed, and some examples were given. The limits of antenna gain and bandwidth were addressed. The relationship between an antenna gain and its size was explained, realising that an increase in the size leads to increase the antenna gain. The antenna bandwidth and its variation versus the radiation Q were discussed. The Fano criterion was also presented in order to explain its impact on the enhancement of the bandwidth of the antenna system. An appropriate antenna candidate for the proposed terahertz communication system, which is the slotted waveguide antenna, was identified. Useful details regarding the design of the slotted waveguide antennas were presented. The steps to design slotted waveguide antenna were simplified, and implemented into two designs at 300 GHz. The simulated results obtained here were close to the theoretical expectation.

2.7 References

1. Stutzman, W.L. and G.A. Thiele, *Antenna theory and design*. 1997: John Wiley & Sons.
2. Kraus, J.D. and R.J. Marhefka, *Antenna for all applications*. Upper Saddle River, NJ: McGraw Hill, 2002.
3. Balanis, C.A., *Antenna theory: analysis and design*. Vol. 1. 2005: John Wiley & Sons.
4. NASA, *Goldstone Deep Space Communications Complex*. Retrieved from <http://www.gdscc.nasa.gov/>, 2015.
5. Oliner, A.A., D.R. Jackson, and J. Volakis, *Antenna Engineering Handbook*. McGraw Hill, 2007.
6. Huang, Y. and K. Boyle, *Antennas: from theory to practice*. 2008: John Wiley & Sons.
7. Kingbastard, *Satellite tracking-acquisition antenna*. Retrieved from https://en.wikipedia.org/wiki/File:Traqueur_acquisition.JPG#filehistory, 2015.
8. Sabat Jr, J.W., *Structural response of the slotted waveguide antenna stiffened structure components under compression*. 2010, DTIC Document.
9. Hirokawa, J., M. Ando, and N. Goto, *Waveguide-fed parallel plate slot array antenna*. *Antennas and Propagation, IEEE Transactions on*, 1992. **40**(2): p. 218-223.
10. Mizutani, A., et al., *Grating lobe suppression of narrow-wall slotted hollow waveguide millimeter-wave planar antenna for arbitrarily linear polarization*. *Antennas and Propagation, IEEE Transactions on*, 2007. **55**(2): p. 313-320.
11. Ando, M., et al., *Novel single-layer waveguides for high-efficiency millimeter-wave arrays*. *Microwave Theory and Techniques, IEEE Transactions on*, 1998. **46**(6): p. 792-799.
12. Zhang, M., J. Hirokawa, and M. Ando, *An E-band partially corporate feed uniform slot array with laminated quasi double-layer waveguide and virtual PMC terminations*. *Antennas and Propagation, IEEE Transactions on*, 2011. **59**(5): p. 1521-1527.
13. Hirokawa, J., *Plate-laminated Waveguide Slot Array Antennas and its Polarization Conversion Layers*. *Automatika–Journal for Control, Measurement, Electronics, Computing and Communications*, 2012. **53**(1).
14. Chu, L.J., *Physical Limitations of Omni-Directional Antennas*. *Journal of applied physics*, 1948. **19**(12): p. 1163-1175.
15. Harrington, R.F., *Effect of antenna size on gain, bandwidth, and efficiency*. *J. Res. Nat. Bur. Stand*, 1960. **64**(1): p. 1-12.
16. Wheeler, H., *Fundamental limitations of small antennas*. *Proceedings of the IRE*, 1947. **35**(12): p. 1479-1484.
17. Lancaster, M.J., *Passive microwave device applications of high-temperature superconductors*. 2006: Cambridge University Press.

18. Huynh, M.-C., *Wideband compact antennas for wireless communication applications*. 2004, Virginia Polytechnic Institute and State University.
19. Hamid, M.R., *Wideband reconfigurable antennas*. 2011, University of Birmingham.
20. phpBB, *OpenEMS support forum*. Retrieved from <http://openems.de/forum/viewtopic.php?f=3&t=27>, 2015.
21. UWBS, *Discover all the possibilities of UWB technology*. Retrieved from <http://uwbs.ru/en/products/sverhshirokopolosnye-pechatnye-i-rupornye-antenny/antrad-8/>, 2015.
22. Collin, R. and S. Rothschild, *Evaluation of antenna Q*. Antennas and Propagation, IEEE Transactions on, 1964. **12**(1): p. 23-27.
23. Fante, R.L., *Quality factor of general ideal antennas*. Antennas and Propagation, IEEE Transactions on, 1969. **17**(2): p. 151-155.
24. McLean, J.S., *A re-examination of the fundamental limits on the radiation Q of electrically small antennas*. Antennas and Propagation, IEEE Transactions on, 1996. **44**(5): p. 672.
25. Fano, R.M., *Theoretical limitations on the broadband matching of arbitrary impedances*. Journal of the Franklin Institute, 1950. **249**(1): p. 57-83.
26. Carlin, H., *Theoretical Limitations on the Broad-Band Matching of Arbitrary Impedances*. Circuit Theory, IRE Transactions on, 1961. **8**(2): p. 165-165.
27. Iyer, V., *Broadband Impedance Matching of Antenna Radiators*. 2010, Worcester Polytechnic Institute.
28. Pozar, D.M., *Microwave engineering*. 2009: John Wiley & Sons.
29. Sadiku, M.N., *Elements of electromagnetics*. 2002: Oxford university press.
30. Shang, X., *SU-8 micromachined terahertz waveguide circuits and coupling matrix design of multiple passband filters*. 2011, University of Birmingham.
31. Sorrentino, R. and G. Bianchi, *Microwave and RF engineering*. Vol. 1. 2010: John Wiley & Sons.
32. Booker, H.G., *Slot aerials and their relation to complementary wire aerials (Babinet's principle)*. Electrical Engineers-Part IIIA: Radiolocation, Journal of the Institution of, 1946. **93**(4): p. 620-626.
33. Watson, W., *Resonant slots*. Electrical Engineers-Part IIIA: Radiolocation, Journal of the Institution of, 1946. **93**(4): p. 747-777.
34. Stevenson, A., *Theory of Slots in Rectangular Wave-Guides*. Journal of Applied Physics, 1948. **19**(1): p. 24-38.
35. Stegen, R., *Slot radiators and arrays at X-band*. Antennas and Propagation, Transactions of the IRE Professional Group on, 1952. **1**(1): p. 62-84.

36. Oliner, A., *The impedance properties of narrow radiating slots in the broad face of rectangular waveguide: Part I--Theory*. Antennas and Propagation, IRE Transactions on, 1957. **5**(1): p. 4-11.
37. Elliott, R.S. and L. Kurt, *The design of small slot arrays*. Antennas and Propagation, IEEE Transactions on, 1978. **26**(2): p. 214-219.
38. Elliott, R.S., *An improved design procedure for small arrays of shunt slots*. Antennas and Propagation, IEEE Transactions on, 1983. **31**(1): p. 48-53.
39. Stern, G.J. and R.S. Elliott, *Resonant length of longitudinal slots and validity of circuit representation: Theory and experiment*. Antennas and Propagation, IEEE Transactions on, 1985. **33**(11): p. 1264-1271.
40. Hamadallah, M., *Frequency limitations on broad-band performance of shunt slot arrays*. Antennas and Propagation, IEEE Transactions on, 1989. **37**(7): p. 817-823.
41. Loughlin, W.R., Y.U. Kim, and R.S. Elliott, *Pattern synthesis for a forward-fire/backward-fire linear array*. Antennas and Propagation, IEEE Transactions on, 1989. **37**(6): p. 721-727.
42. Rengarajan, S.R., *Compound radiating slots in a broad wall of a rectangular waveguide*. Antennas and Propagation, IEEE Transactions on, 1989. **37**(9): p. 1116-1123.
43. Studio, C.M., *Computer simulation technology*. GmbH, Darmstadt, Germany, 2009.
44. Wang, Y., et al., *Micromachined 300-GHz SU-8-based slotted waveguide antenna*. Antennas and Wireless Propagation Letters, IEEE, 2011. **10**: p. 573-576.
45. Skaik, T., et al. *A micromachined WR-3 waveguide with embedded bends for direct flange connections*. in *Microwave Conference (EuMC), 2010 European*. 2010. IEEE.

Chapter 3

Filter theories and antenna-filter integration

This Chapter presents the fundamental filter theories that are required for the integration of antennas with filters. The coupling matrix approach, which is usually utilised to design coupled-resonator filters, is described. Investigation of the parameters of the coupling matrix, such as external quality factor Q_e , and coupling coefficient $M_{i,i+1}$, are conducted using rectangular waveguide cavity resonators. The design steps for a 3rd order rectangular waveguide filter based on coupled-resonators is then discussed. Later, a method to extract the radiation quality factor Q_r of a *resonator-radiator* based on the rectangular waveguide structure is discussed, and the possible ways to control Q_r are given. A review regarding the integration of antennas with filters is also presented. Following that, the coupling matrix approach has been developed in a way that can be used to integrate a *resonator-radiator* with a coupled-resonator filter, forming the whole integrated *antenna-filter* component. The matrix is developed further to integrate multiple *resonator-radiators* with power splitters based on coupled-resonators.

3.1 Overview of filter theories

Radio frequency (RF) and microwave filters are devices employed in many communications and radar systems to transmit signals over some required bands of frequencies and attenuate them at unwanted bands of frequencies [1]. The following network may be used to represent a

two-port filter circuit [2]:

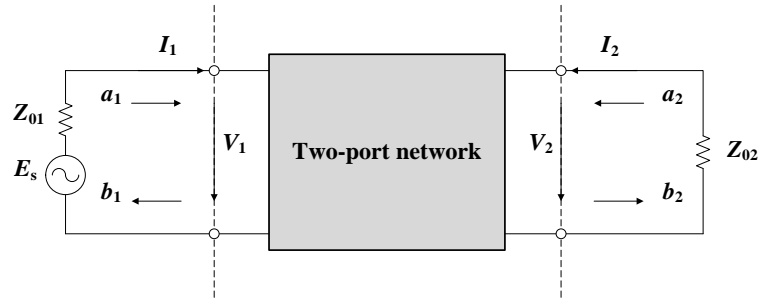


Figure 3.1: Two-port network representation of a filter circuit. E_s is the voltage of the source, Z_{01} and Z_{02} are the impedances of the source and the load, and I_1 , I_2 and V_1 , V_2 are the current and the voltage parameters of the source and the load, respectively (this diagram is re-produced from [2]).

The parameters a_1 , b_1 and a_2 , b_2 shown in Figure 3.1 are used to indicate the incident and reflected waves of the filter network, and have relations with the voltage and the current of the ports as [2]:

$$\begin{aligned} a_n &= \frac{1}{2} \left(\frac{V_n}{\sqrt{Z_{0n}}} + \sqrt{Z_{0n}} I_n \right) \\ b_n &= \frac{1}{2} \left(\frac{V_n}{\sqrt{Z_{0n}}} - \sqrt{Z_{0n}} I_n \right) \end{aligned} \quad n = 1 \text{ and } 2 \quad (3.1)$$

The reflection (S_{11} , S_{22}) and transmission (S_{21} , S_{12}) coefficients, which are also known as scattering parameters, are important parameters of a filter circuit, and can be defined in terms of the incident and reflected waves as follows [2]:

$$\begin{aligned} S_{11} &= \left. \frac{b_1}{a_1} \right|_{a_2=0} & S_{12} &= \left. \frac{b_1}{a_2} \right|_{a_1=0} \\ S_{21} &= \left. \frac{b_2}{a_1} \right|_{a_2=0} & S_{22} &= \left. \frac{b_2}{a_2} \right|_{a_1=0} \end{aligned} \quad (3.2)$$

where S_{11} stands for the reflection coefficient of the signal reflected from Port 1 (source), and S_{21} is the signal reflected from Port 1 to Port 2 (load). If the two-port filter circuit is

reciprocal, then $S_{21} = S_{12}$, and if it is symmetric, then $S_{11} = S_{22}$. The conservation law of energy ($S_{11}^2 + S_{21}^2 = 1$) can be applied if the filter circuit is lossless.

In general, the scattering parameters (S_{mn}) are complex, and consist of real and imaginary parts, that is, $S_{mn} = |S_{mn}|e^{j\phi_{mn}}$. The return loss (L_R) at Port n , and the insertion loss (L_A) between Ports n and m are related to the amplitude of the scattering parameters, and they can be computed in decibel units using the equations given below [3]:

$$\begin{aligned} L_R &= -20 \log|S_{nn}| \quad \text{dB} \quad n = 1 \text{ and } 2 \\ L_A &= -20 \log|S_{mn}| \quad \text{dB} \quad m, n = 1 \text{ and } 2 \quad (m \neq n) \end{aligned} \quad (3.3)$$

For a lossless network, the L_R and L_A are connected to each other via the following relations [2]:

$$\begin{aligned} L_R &= -10 \log(1 - 10^{-L_A/10}) \quad \text{dB} \\ L_A &= -10 \log(1 - 10^{-L_R/10}) \quad \text{dB} \end{aligned} \quad (3.4)$$

It is interesting to note that for a two-port filter circuit, there is a delay in the received signal at Port 2 that is usually characterised by the group delay (τ_d) parameter as follows [3]:

$$\tau_d = -\frac{d\phi_{21}}{d\omega} \quad \text{sec} \quad (3.5)$$

where ϕ_{21} is the phase of the transmission coefficient S_{21} in radians, and ω is the angular frequency.

The transfer function of any RF/microwave filter, is a mathematical representation of the S_{21} parameter, and is considered as one of the most important functions used to define the response of any given filter. For a two-port lossless filter, the square of the amplitude of the transfer function may be defined as follows [2]:

$$|S_{21}(j\Omega)|^2 = \frac{1}{1 + \varepsilon^2 F_n^2(\Omega)} \quad (3.6)$$

Here ε is the ripple constant, $F_n(\Omega)$ is the characteristic function, and Ω is the radian frequency variable. For a lossless filter circuit ($S_{11}^2 + S_{21}^2 = 1$), the square of the amplitude of the input function $S_{11}(j\Omega)$ can be computed using Equation 3.6, and is given by [3]:

$$|S_{11}(j\Omega)|^2 = 1 - |S_{21}(j\Omega)|^2 = 1 - \frac{1}{1 + \varepsilon^2 F_n^2(\Omega)} \quad (3.7)$$

There are certain types of transfer functions that are used for the design of filters. With the use of different transfer functions, different responses for filters can be obtained. The examples are: the Butterworth, Chebyshev, Elliptic, Gaussian, and All-pass responses. Each of these responses is desired for a specific application. The Chebyshev response is chosen in this thesis to design a filter system that can be integrated with an antenna (*antenna-filter*).

In general, the Chebyshev response has equal ripple in the passband, and is also maximally flat in the stopband, as shown in Figure 3.2 [2]. The transfer function of a filter based on the Chebyshev response is given as below [3]:

$$|S_{21}(j\Omega)|^2 = \frac{1}{1 + \varepsilon^2 T_n^2(\Omega)} \quad (3.8)$$

Here, ε is the passband ripple constant, and it can be computed from the passband ripple L_{Ar} (in dB), as [3]:

$$\varepsilon = \sqrt{10^{\frac{L_{Ar}}{10}} - 1} \quad (3.9)$$

Also, T_n is the Chebyshev polynomial of the first kind of order n , and it can be expressed mathematically as follows [2]:

$$T_n(\Omega) = \begin{cases} \cos(n \cos^{-1}\Omega) & |\Omega| \leq 1 \\ \cosh(n \cosh^{-1}\Omega) & |\Omega| \geq 1 \end{cases} \quad (3.10)$$

Bandpass filters can typically be built using one or more coupled resonators. The electrical parameters of resonators, such as quality factors and coupling coefficients, are able to control the response of filters such as the selectivity and fractional bandwidth. Figure 3.3 shows an ideal response of a 3rd order Chebyshev filter. The order number is usually equal to the number of resonators used to build the filter circuit. The passband ripple L_{Ar} is chosen to be 0.0436 dB (see Figure 3.3 (b)). Substituting this value into Equation 3.4, the return loss level L_R in dB over the passband can be calculated and is equal to -20 dB (see Figure 3.3 (a)). The fractional bandwidth of the filter is normalised in the range $-1 \leq \Omega \leq 1$.

In the following sections, some details of the general coupling matrix, which is an approach widely used to design filters based on coupled-resonator circuits, is discussed with given examples.

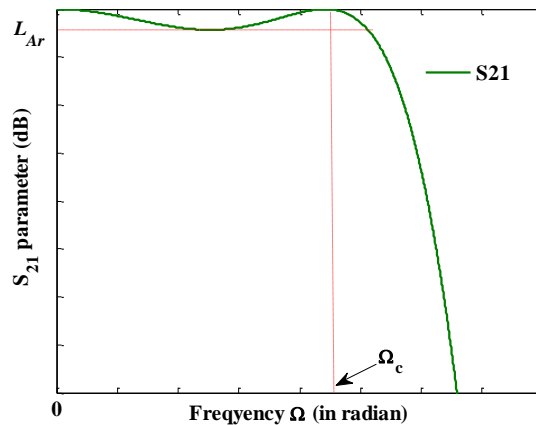


Figure 3.2: Chebyshev response of a lowpass prototype filters.

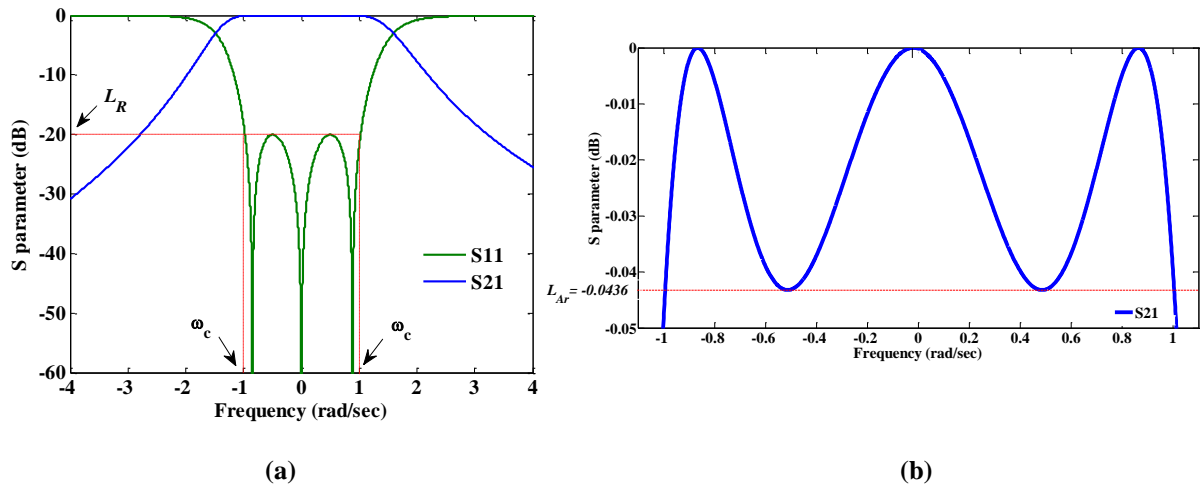
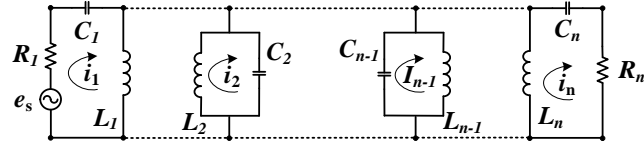


Figure 3.3: An ideal response of a 3rd order low pass filter based on the Chebyshev response with a 0.0436 dB passband ripple, (a) the magnitude of the S-parameters, (b) The enlarged scale of S₂₁ to show the passband level.

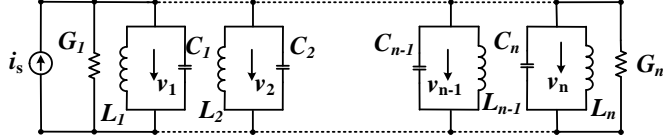
3.2 General coupling matrix theory

The concept of the coupling matrix was introduced in the early 1970s by William and Atia for the design of narrow-bandwidth bandpass waveguide cavity filters [4, 5]. It is used to represent the filters made with coupled resonators in the form of a matrix. The main advantages of this concept are: (i) each unit in the matrix can be used to refer to a specific physical dimension of the resonators used in the design of the filter circuit, and (ii) some mathematical operations can be performed for the topology of the filters with the use of the coupling matrix concept. These operations are not easy to realise with the other design concepts [3, 6].

An equivalent circuit of a filter, made out of n -coupled resonator, is shown in Figure 3.4 (a). The resonators are coupled to each other by the mutual inductances between the resonators (magnetically coupled). Here, C , R , and L refer to the capacitance, resistance, and reactance of the circuit. The symbol i shows the loop current path, and e_s is the voltage of the source.



(a)



(b)

Figure 3.4: Two equivalent circuits of a filter made out of n -coupled resonators. The resonators are coupled, (a) magnetically by the mutual inductances, (b) electrically by the mutual capacitances [2].

According to the Kirchhoff's voltage law, the vector sum of the voltage drops present in a single circuit is equal to zero. After applying this law for the given equivalent circuit, a set of loop equations can be derived. These equations can be represented in the form of a matrix as shown below [2]:

$$\begin{bmatrix} R_1 + j\omega L_1 + \frac{1}{j\omega C_1} & -j\omega L_{12} & \dots & -j\omega L_{1n} \\ -j\omega L_{21} & j\omega L_2 + \frac{1}{j\omega C_2} & \dots & -j\omega L_{2n} \\ \vdots & \vdots & \ddots & \vdots \\ -j\omega L_{n1} & -j\omega L_{n2} & \dots & R_n + j\omega L_n + \frac{1}{j\omega C_n} \end{bmatrix} \begin{bmatrix} i_1 \\ i_2 \\ \vdots \\ i_n \end{bmatrix} = \begin{bmatrix} e_s \\ 0 \\ \vdots \\ 0 \end{bmatrix} \quad (3.11)$$

Or

$$[Z] \cdot [i] = [e] \quad (3.12)$$

Here, $[Z]$, $[i]$, and $[e]$ are the $n \times n$ impedance, current and voltage matrices of the equivalent circuit respectively. In order to simplify the calculation, some assumptions need to be introduced. For instance, all the resonators need to be assumed to resonate at the same centre frequency $\omega_0 = 1/\sqrt{LC}$ (synchronously tuned filter). This leads us to assume that, $L = L_1 =$

$L_2 = \dots = L_n$, and $C = C_1 = C_2 = \dots = C_n$. In addition to this, the bandwidth of the filter is assumed to be narrow ($\omega = \omega_0$). After applying these assumptions, the normalised impedancematrix of the filter can be simplified to the following [2]:

$$[\bar{Z}] = \begin{bmatrix} \frac{1}{q_{e1}} + p & -jm_{12} & \dots & -jm_{1n} \\ -jm_{21} & p & \dots & -jm_{2n} \\ \vdots & \vdots & \ddots & \vdots \\ -jm_{n1} & -jm_{n2} & \dots & \frac{1}{q_{en}} + p \end{bmatrix} \quad (3.13)$$

where q_{ei} is the scaled external quality factor, m_{ij} is the coupling coefficient between the resonators of the filter, and p is the complex frequency variable. They can be computed using the following relations [2]:

$$q_{ei} = \frac{\omega_0 L}{R_i} \cdot FBW \quad \text{for } i=1, n$$

$$m_{ij} = \frac{L_{ij}}{L} \cdot \frac{1}{FBW} \quad (3.14)$$

$$p = j \frac{1}{FBW} \left(\frac{\omega}{\omega_0} - \frac{\omega_0}{\omega} \right)$$

where $FBW = \Delta\omega/\omega_0$ is the fractional bandwidth of the filter.

According to [2], if the resonators of the filter are asynchronously tuned (the resonators resonate at different frequencies $\omega_{0i} = 1/\sqrt{L_i C_i}$), the self-couplings ($m_{ii}, m_{jj} \dots$) need to be considered in the calculation. The normalised impedance matrix, after taking the self-coupling into account, becomes [2]:

$$[\bar{Z}] = \begin{bmatrix} \frac{1}{q_{e1}} + p - jm_{11} & -jm_{12} & \dots & -jm_{1n} \\ -jm_{21} & p - jm_{22} & \dots & -jm_{2n} \\ \vdots & \vdots & \ddots & \vdots \\ -jm_{n1} & -jm_{n2} & \dots & \frac{1}{q_{en}} + p - jm_{nn} \end{bmatrix} \quad (3.15)$$

The only difference between the normalised impedance matrix in 3.15 and 3.13 is that the matrix 3.15 has extra entries m_{ii} in the leading diagonal. This is due to accounting for the asynchronous tuning of the filter.

As mentioned in Section 3.1, a filter can be considered as a two-port network. In this case, the scattering parameters of the filter can be given in terms of the normalised impedance matrix as [2]:

$$\begin{aligned} S_{21} &= 2 \frac{1}{\sqrt{q_{e1}q_{en}}} \cdot [\bar{Z}]_{n1}^{-1} \\ S_{11} &= 1 - \frac{2}{q_{e1}} \cdot [\bar{Z}]_{11}^{-1} \end{aligned} \quad (3.16)$$

So far, in the analysis, it is considered that all the resonators of the filter are coupled only via the mutual inductance (magnetically coupled, see Figure 3.4 (a)). A similar analysis can be conducted for the calculation of the scattering parameters of the filter if the resonators are coupled via mutual capacitances (Figure 3.4 (b)). The analysis is fully discussed in [2], and only the scattering parameters of the filter are given here, which are [2, 3]:

$$\begin{aligned} S_{21} &= 2 \frac{1}{\sqrt{q_{e1}q_{en}}} \cdot [\bar{Y}]_{n1}^{-1} \\ S_{11} &= -\left(1 - \frac{2}{q_{e1}}\right) \cdot [\bar{Y}]_{11}^{-1} \end{aligned} \quad (3.17)$$

where $[\bar{Y}]$ denotes the $n \times n$ admittance matrix of the filter. In case of asynchronous tuning, it can be expressed as follows [3]:

$$[\bar{Y}] = \begin{bmatrix} \frac{1}{q_{e1}} + p - jm_{11} & -jm_{12} & \dots & -jm_{1n} \\ -jm_{21} & p - jm_{22} & \dots & -jm_{2n} \\ \vdots & \vdots & \ddots & \vdots \\ -jm_{n1} & -jm_{n2} & \dots & \frac{1}{q_{en}} + p - jm_{nn} \end{bmatrix} \quad (3.18)$$

It is interesting to note that both the normalised admittance and impedance matrices are identical. This helps us to have a general form for the scattering parameters of an n -coupled resonators filter, no matter whether the resonators are electrically or magnetically coupled, or a combination of both. The general form of the scattering parameters of an n -coupled resonator filter is [2]:

$$S_{21} = 2 \frac{1}{\sqrt{q_{e1}q_{en}}} \cdot [A]_{n1}^{-1} \quad (3.19)$$

$$S_{11} = \pm \left(1 - \frac{2}{q_{e1}}\right) \cdot [A]_{11}^{-1}$$

Here $[A]$ is the sum of three matrices as given below [2]:

$$[A] = \begin{bmatrix} \frac{1}{q_{e1}} & 0 & \dots & 0 \\ 0 & 0 & \dots & 0 \\ \vdots & \vdots & \ddots & \vdots \\ 0 & 0 & \dots & \frac{1}{q_{en}} \end{bmatrix} + p \begin{bmatrix} 1 & 0 & \dots & 0 \\ 0 & 1 & \dots & 0 \\ \vdots & \vdots & \ddots & \vdots \\ 0 & 0 & \dots & 1 \end{bmatrix} - j \begin{bmatrix} m_{11} & m_{12} & \dots & m_{1n} \\ m_{21} & m_{22} & \dots & m_{2n} \\ \vdots & \vdots & \ddots & \vdots \\ m_{n1} & m_{n2} & \dots & m_{nn} \end{bmatrix} \quad (3.20)$$

Or

$$[A] = [q] + p[U] - j[m] \quad (3.21)$$

where, $[q]$ is an $n \times n$ matrix with all zero entries except $q_{11} = 1/q_{e1}$ and $q_{nn} = 1/q_{en}$. $[U]$ is an $n \times n$ identity matrix, and $[m]$ is the general coupling matrix. The entry elements of the coupling matrix can be used to represent the physical coupling dimensions between the resonators of the filter. For instance m_{12} refers to a coupling coefficient value between Resonators 1 and 2. More details are given below.

The matrices given in Equation 3.20 is generalised for a filter built from n -coupled resonators ($n = 1, 2 \dots$). In the following, the matrices have been specialised for a 3rd order filter (see Equation 3.22), and interpreted to a physical layout of the filter (see Figure 3.5).

$$[A] = \begin{bmatrix} \frac{1}{q_{e1}} & 0 & 0 \\ 0 & 0 & 0 \\ 0 & 0 & \frac{1}{q_{e2}} \end{bmatrix} + p \begin{bmatrix} 1 & 0 & 0 \\ 0 & 1 & 0 \\ 0 & 0 & 1 \end{bmatrix} - j \begin{bmatrix} m_{11} & m_{12} & m_{13} \\ m_{21} & m_{22} & m_{23} \\ m_{31} & m_{32} & m_{33} \end{bmatrix} \quad (3.22)$$

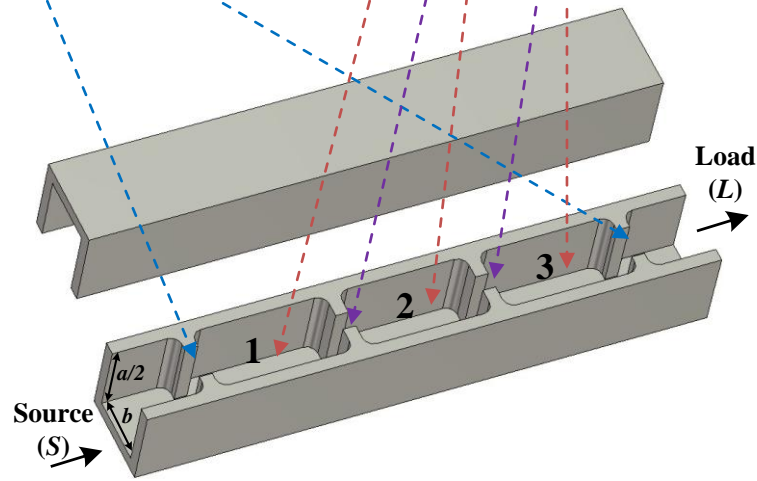


Figure 3.5: Layout of a 3rd order filter based on the waveguide cavity resonators.

Each element in the matrices in Equation 3.22 can be used to determine the physical dimensions of the filter as pointed out in Figure 3.5 (see the arrows). The scaled coupling coefficient and external quality factor, for a filter based on the Chebyshev response, can be calculated using the equations given below [2]:

$$m_{i,i+1} = \frac{1}{\sqrt{g_i g_{i+1}}} \quad i = 1 \text{ to } n - 1 \quad (3.23)$$

$$q_{e1} = g_0 \cdot g_1, \quad q_{en} = g_n \cdot g_{n+1} \quad (3.24)$$

Here, g is the element value of a two-port filter, which can be calculated by using the following relations [2]:

$$\left. \begin{aligned}
&g_0 = 1.0 \\
&g_0 = \frac{2}{\gamma} \sin\left(\frac{\pi}{2n}\right) \\
&\gamma = \sinh\left(\frac{\beta}{2n}\right) \\
&\beta = \ln\left[\coth\left(\frac{L_{Ar}}{17.37}\right)\right] \\
&g_i = \frac{1}{g_{i-1}} \frac{4 \sin\left[\frac{(2i-1)\pi}{2n}\right] \cdot \sin\left[\frac{(2i-3)\pi}{2n}\right]}{\gamma^2 + \sin^2\left[\frac{(i-1)\pi}{2n}\right]} \quad i = 2, 3, \dots, n \\
&g_{n+1} = \begin{cases} 1.0 & \text{if } n \text{ odd} \\ \coth^2\left(\frac{\beta}{4}\right) & \text{if } n \text{ even} \end{cases}
\end{aligned} \right\} \quad (3.25)$$

In the following sections, details regarding cavity resonator, particularly, rectangular waveguide resonators are given. The design of a 3rd order filter based on the Chebyshev response is then presented.

3.3 Cavity resonators

Cavity resonators can be considered as devices used to confine the electric and the magnetic fields of electromagnetic waves. Figure 3.5 shows two sets of equivalent circuits of a cavity resonator. It is possible to classify cavity resonators into two types according to their electrical performance, which are lossless and lossy cavity resonators. The lossless cavity resonator is ideal without having any form of losses (i.e. $R = 0$, see Figures 3.6 (a) and (b)). The losses in the lossy resonators are usually due to leaking of the electromagnetic waves (radiation), the conductivity of the material used to construct the resonator, and the dielectric losses of the material inserted into the resonator. The resistance R and reactance G elements are used to represent these losses in the circuit of the lossy cavity resonator (see Figure 3.6 (c) and (d)).

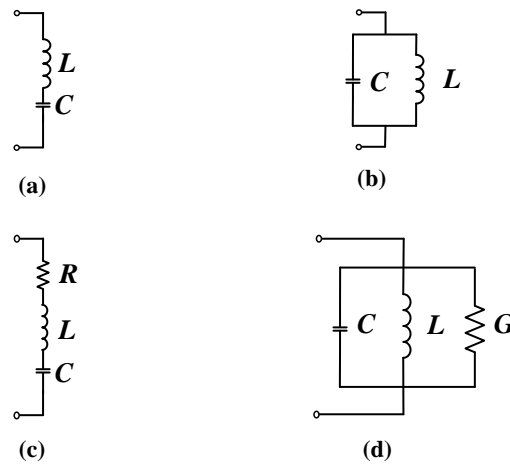


Figure 3.6: Four possible equivalent circuits for a cavity resonator. A lossless cavity when the elements are: (a) in series, and (b) in parallel. A lossy cavity when the elements are: (c) in series, and (d) in parallel (taken from [7]).

There are different types of cavity resonators existed such as microstrip cavity resonators, waveguide cavity resonators, and dielectric cavity resonators. In this thesis, only rectangular waveguide cavity resonators will be described and utilised in the design of antennas.

3.3.1 Rectangular waveguide cavity resonators

A rectangular waveguide cavity resonator is a section of a rectangular waveguide where both ends are short circuited (Figure 3.7). It is usually fed by a small probe or an aperture. Because both the ends are short circuited, standing wave with various TE and TM modes are expected to exist inside the cavity. There are two important parameters for cavity resonators, which are the resonant frequency and the quality factors. These are discussed below.

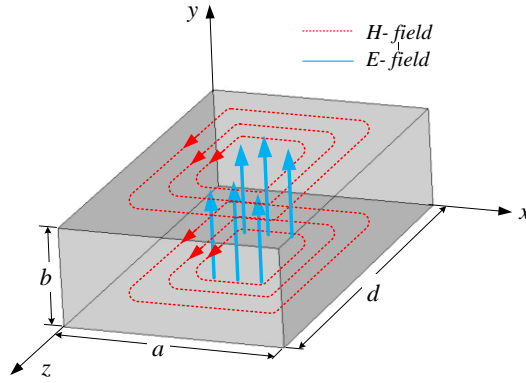


Figure 3.7: Rectangular waveguide cavity with the configuration of the electromagnetic field for the propagated TE_{101} mode.

In Chapter 2, Equation 2.11 is given to express the transverse electric fields for both TE_{mn} and TM_{mn} modes in a rectangular waveguide. From that equation a relationship between the length of a rectangular cavity resonator d and the guided wavelength λ_g can be obtained, when applying the boundary conditions $\vec{E}_t = 0$ at $z = 0$ and $z = d$, that is [1]:

$$\beta_{mn}d = l\pi \quad \text{When } l = 1, 2, 3, \dots \quad (3.26)$$

Equation 3.26 implies that the waveguide cavity length d has to be equal to an integer multiple of a half-guided wavelength at the resonant frequency. The resonant frequency f_{mnl} of the modes in a rectangular waveguide cavity can be calculated by [1]:

$$f_{mnl} = \frac{c}{2\pi\sqrt{\mu_r\epsilon_r}} \sqrt{\left(\frac{m\pi}{a}\right)^2 + \left(\frac{n\pi}{b}\right)^2 + \left(\frac{l\pi}{d}\right)^2} \quad (3.27)$$

where, c is the speed of light, ϵ_r and μ_r are the relative permittivity and relative permeability of the material filling the cavity, and the integer numbers m , n , and l are used to represent the mode of the electric and magnetic fields of a half wave inside the cavity in the x , y , and z directions. The TE_{101} mode in a rectangular waveguide cavity, as shown in Figure 3.7, is considered as the dominant mode due to having the lowest resonant frequency.

The unloaded quality factor Q_0 , which is a measure of the average losses and energy storage in a cavity, is another important parameter of cavity resonator. It can be calculated by [7]:

$$\frac{1}{Q_0} = \frac{1}{Q_c} + \frac{1}{Q_d} + \frac{1}{Q_r} \quad (3.28)$$

where, Q_d , Q_r and Q_c are the losses due to the dielectric material filling the cavity, the radiation, and the conductivity of the conductor material built the cavity, respectively. Here, Q_r is not considered to be obtained from one of the ports of the resonator. Q_c for a lossless dielectric of the rectangular waveguide can be found by [1]:

$$Q_c = \frac{(kad)^3}{2\pi^2 R_s} \frac{b\eta}{(2l^2 a^3 b + 2bd^3 + l^2 a^3 d + ad^3)} \quad (3.29)$$

The loaded quality factor Q_l of a cavity resonator is equal to the combination of the Q_0 and Q_e , and is given as [7]:

$$\frac{1}{Q_l} = \frac{1}{Q_0} + \frac{1}{Q_e} \quad (3.30)$$

In the next section, the design of a filter based on the rectangular waveguide cavity resonators, as an exercise, is presented.

3.4 Design of a 3rd order coupled-resonators waveguide filter

This section demonstrates the synthesis of a 3rd order filter based on the rectangular waveguide WR-90 (8-12 GHz) cavity resonators. It consists of three rectangular coupled-resonators in series that are synchronously tuned. The electrical specification of the filter, which is chosen arbitrarily for this exercise, is given in Table 3.1. Based on the specification,

the external quality factor Q_e (input/output couplings), and coupling coefficient $M_{i,i+1}$ between the resonators can be calculated using the following relations [2]:

$$Q_{e1} = \frac{q_{e1}}{FBW} = \frac{g_0 g_1}{FBW} \quad \text{And} \quad Q_{en} = \frac{q_{en}}{FBW} = \frac{g_n g_{n+1}}{FBW} \quad (3.31)$$

$$M_{i,i+1} = FBW \cdot m_{i,i+1} = \frac{FBW}{\sqrt{g_i g_{i+1}}} \quad \text{for } i = 1, 2, \dots, n-1 \quad (3.32)$$

Here, g represents the element values of the Chebyshev lowpass prototype filters, and can be calculated using Equation 3.25, giving: $g_0 = g_4 = 1.0$, $g_1 = g_3 = 0.8516$, $g_2 = 1.1032$. Inserting these values into Equations 3.31 and 3.32, the required Q_e and $M_{i,i+1}$ for the 3rd order filter can be obtained, which are: $Q_{e1} = Q_{e2} = 8.516$, and $M_{12} = M_{23} = 0.1032$.

Table 3.1
Electrical specification of the 3rd order rectangular waveguide WR-90 cavity filter

| Electrical specification | Values |
|--|------------------|
| Order of the filter (n) | 3 |
| Passband ripple (L_{Ar}), or Return loss level | 0.0436 dB, 20 dB |
| Centre frequency (f_0) | 10 GHz |
| Fractional bandwidth (FBW) | 0.1, or 10 % |

After the substitution of the values of Q_{e1} and M_{12} into Equation 3.20, the coupling matrix for the 3rd order filter can be given by:

$$[A] = \begin{bmatrix} 0.1117 & 0 & 0 \\ 0 & 0 & 0 \\ 0 & 0 & 0.1117 \end{bmatrix} + j \frac{1}{FBW} \left(\frac{\omega}{\omega_0} - \frac{\omega_0}{\omega} \right) \begin{bmatrix} 1 & 0 & 0 \\ 0 & 1 & 0 \\ 0 & 0 & 1 \end{bmatrix} - j \begin{bmatrix} 0 & 0.103 & 0 \\ 0.103 & 0 & 0.103 \\ 0 & 0.103 & 0 \end{bmatrix} \quad (3.33)$$

After inserting the matrix given in Equation 3.33 into Equation 3.19, the scattering parameters (S_{11} and S_{21}) of the 3rd order filter can be obtained, and they are plotted in Figure 3.8.

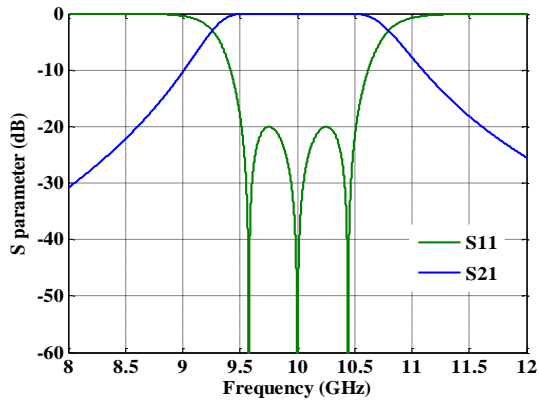


Figure 3.8: An ideal response of a 3rd order Chebyshev filter.

The physical layout of the 3rd order filter with its equivalent topology is shown in Figure 3.9. As can be seen in Figure 3.9 (a), irises are proposed for the realisation of the coupling between the resonators and the ports. The iris types can be inductive or capacitive, or a combination of both. Here, symmetric capacitive irises are chosen due to the fact that: (i) they allow us to cut the waveguide at the centre of the broad wall which reduces the losses [3], and (ii) they are more suitable for wide bandwidth filter application than others [3]. In the next sub-sections, the design techniques used to extract the coupling values from the physical structure between the resonators and the ports are demonstrated.

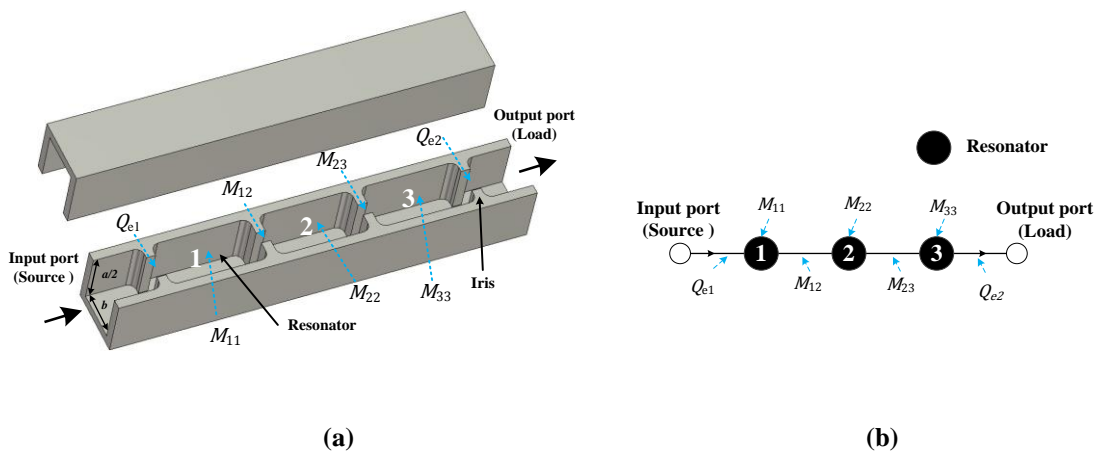


Figure 3.9: (a) Physical structure of the 3rd order waveguide filter based on the waveguide coupled-resonators, (b) its equivalent topology.

3.4.1 Extraction of the external quality factor (Q_e)

This section explains a technique that is used for the extraction of the Q_e . The structure shown in Figure 3.10 is modelled in CST [8]. It consists of a single rectangular waveguide cavity resonator which is coupled to an input and an output ports via capacitive irises.

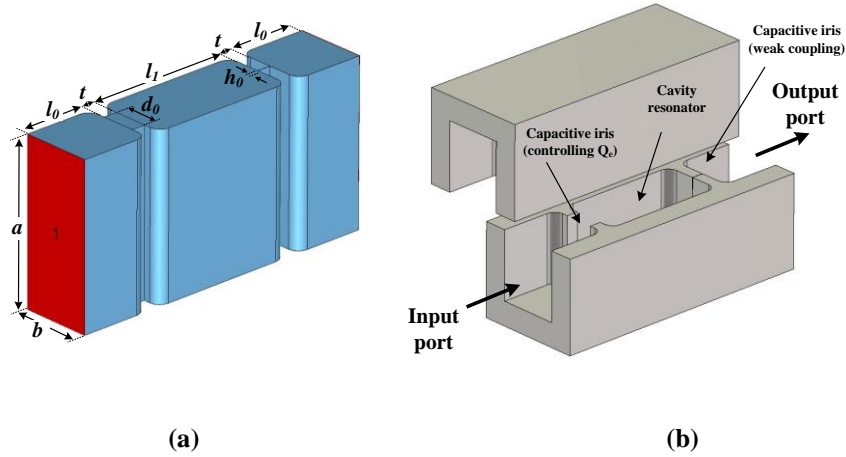


Figure 3.10: Structure modelled in CST for the extraction of the Q_e , (a) inside view of the structure, (b) the real structure. Dimensions, $a = 22.86$ mm, $b = 10.16$ mm, $l_0 = 10.16$ mm, $h_0 = 0.04$ mm, $t = 2$ mm.

The S_{21} parameter, which is realised from the structure shown in Figure 3.10, is plotted in Figure 3.11 (a). It is used here for the calculation of Q_e using the relationship between the resonant frequency f_0 of the cavity and 3-dB bandwidth Δf_{3dB} as follows [3]:

$$Q_e = \frac{f_0}{\Delta f_{3dB}} \quad (3.34)$$

The f_0 , Δf , and Q_e values vary when the cavity length l_1 and the iris width d_0 are altered. These variations are shown in Figure 3.11 (b). It can be seen that Q_e reduces when d_0 increases. To obtain any desired Q_e value, the l_1 needs to be tuned in order to keep the f_0 at the desired centre frequency, in this exercise 10 GHz.

For the 3rd order filter, the required $Q_e = 8.516$ can be obtained when the dimensions are: $d_0 = 4.52$ mm and $l_1 = 24.70$ mm. The technique presented in this sub-section will be utilised in Chapters 4 and 5 for the extraction of Q_e of the antennas that will be integrated with the filters.

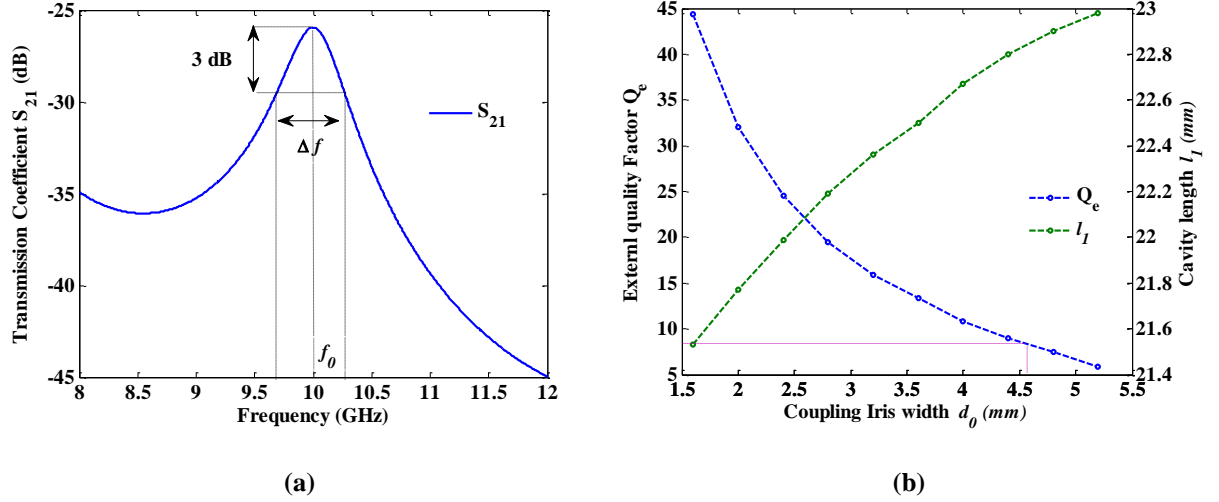


Figure 3.11: (a) the S_{21} response of the structure modelled in CST and is shown in Figure 3.10, (b) variation of the Q_e versus the cavity dimensions.

3.4.2 Extraction of the internal coupling (Coupling coefficient $M_{1,2}$, $M_{2,3}$)

After determining the external quality factor Q_e of the 3rd order filter, the internal coupling (coupling coefficient M_{12}) calculation between the two coupled-resonators are the next step. The M_{12} between two coupled-resonators can usually be defined as the ratio between the coupled energy to stored energy in the resonators, and can be expressed by [2]:

$$M_{12} = \frac{\iiint \varepsilon \vec{E}_1 \cdot \vec{E}_2 dv}{\sqrt{\iiint \varepsilon |\vec{E}_1|^2 dv} \times \sqrt{\iiint \varepsilon |\vec{E}_2|^2 dv}} + \frac{\iiint \mu \vec{H}_1 \cdot \vec{H}_2 dv}{\sqrt{\iiint \mu |\vec{H}_1|^2 dv} \times \sqrt{\iiint \mu |\vec{H}_2|^2 dv}} \quad (3.35)$$

Here, \vec{E} and \vec{H} represents the electric and magnetic field vectors, ε and μ are the permittivity and permeability of the medium where the coupling takes place, and v is the volume of the

medium. According to Equation 3.35, the M_{12} types can be either electric (first term on the right hand side), magnetic (second term on the right hand side), or a combination of these. In this thesis, capacitive irises which maintain electric coupling are utilised for most of the designs. There are some techniques presented in [2] to obtain the M_{12} value. The technique given below is preferred in this work due to its simplicity in implementation.

Two rectangular waveguide resonators modelled in CST and shown in Figure 3.12 are arranged to find M_{12} . The resonators are coupled with each other via a capacitive iris with dimensions dk_{12} , and are weakly coupled to the ports. The M_{12} is [2]:

$$M_{12} = \pm \frac{1}{2} \left(\frac{f_{02}}{f_{01}} + \frac{f_{01}}{f_{02}} \right) \sqrt{\left(\frac{f_2^2 - f_1^2}{f_2^2 + f_1^2} \right)^2 - \left(\frac{f_{02}^2 - f_{01}^2}{f_{02}^2 + f_{01}^2} \right)^2} \quad (3.36)$$

Here, the positive and negative (\pm) signs in Equation 3.36 refer the types of the coupling (capacitive or inductive), f_{01} and f_{02} are the resonant frequencies of the resonators when they are uncoupled, and f_1 and f_2 are the two split resonant frequencies which can be easily realised in the frequency response (S_{21}) of the two-coupled resonators as shown in Figure 3.13 (a). If the two-coupled resonators are tuned synchronously ($f_{01} = f_{02}$), the M_{12} can be obtained as follows:

$$M_{12} = \frac{f_2^2 - f_1^2}{f_2^2 + f_1^2} \quad (3.37)$$

The coupling coefficient of the two-coupled resonators can now be calculated by inserting the values of f_1 and f_2 obtained in Figure 3.13 (a) into Equation 3.37.

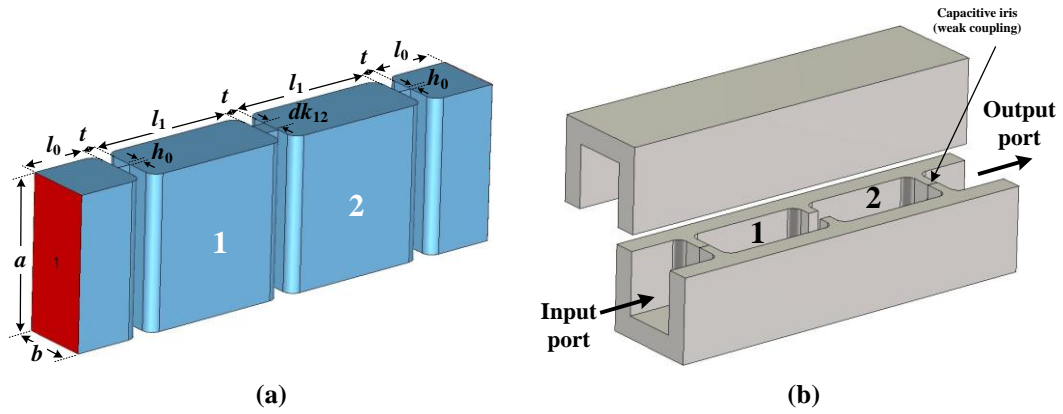


Figure 3.12: Structure modelled in CST for the extraction of the internal coupling (coupling coefficient M_{12}) between two electrically coupled resonators, (a) inside view of the structure, (b) the real structure. Dimensions, $a = 22.86$ mm, $b = 10.16$ mm, $l_0 = 10.16$ mm, $h_0 = 0.04$ mm, $t = 2$ mm. Both of l_1 and dk_{12} are variables to control the M_{12} (Round corner 1.6 mm).

The variation of M_{12} versus the iris width dk_{12} is shown in Figure 3.13 (b). One can see that the M_{12} value increases with the increase of dk_{12} . The length of the resonators l_1 is adjusted here in order to keep the centre frequency at 10 GHz, and it was seen that an increase in the l_1 value is required when dk_{12} is increased. The value of the $M_{12} = M_{23}$ for the 3rd order filter is 0.1032, and it can be obtained when $dk_{12} = 2.265$ as visualised by dotted lines in the Figure 3.13 (b). The technique discussed in this sub-section will be used in Chapters 4 and 5, to extract the coupling values between the resonators that are integrated with the antennas.

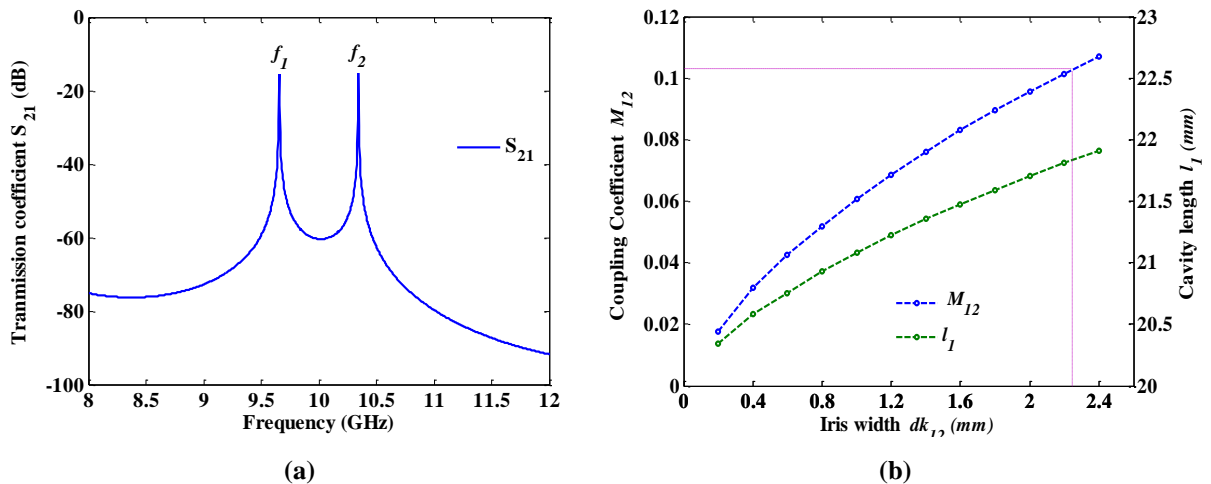


Figure 3.13: (a) the S_{21} response of the two-coupled structure modelled in CST, and is shown in Figure 3.12, (b) variation of the M_{12} versus the cavity dimensions.

3.4.3 Integration and optimisation

After extracting the corresponding aperture dimensions for the Q_e and M_{12} values in the previous sub-sections, the integration of coupled-resonators is now possible here. The physical structure of the 3rd order filter is shown in Figure 3.14, and its initial physical dimensions are summarised in Table 3.2.

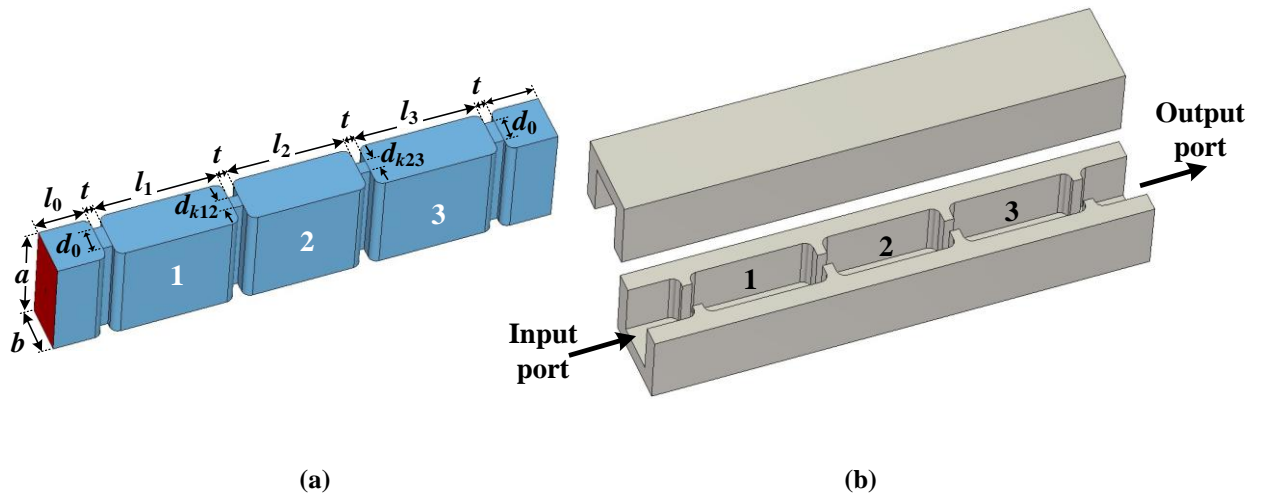


Figure 3.14: Structure modelled in CST for the final design of the 3rd order coupled-resonators filter, (a) inside view of the filter structure, (b) the real filter structure.

Table 3.2

Physical dimensions of the 3rd order coupled-resonators waveguide filter shown in Figure 3.14 operated at frequency range (8-12 GHz).

| Parameters | Initial values (mm) | Optimised values (mm) |
|---|---------------------|-----------------------|
| Cavity resonator length ($l_1=l_3$) | 24.70 | 25.13 |
| Cavity resonator length (l_2) | 23.73 | 24.12 |
| Iris width (d_0) | 4.52 | 5.20 |
| Coupling Iris width ($d_{12}=d_{23}$) | 2.265 | 2.70 |

The initial frequency response of the filter using the values given above is plotted in Figure 3.15 (a), and it is in close agreement with the desired response. Adjustment for the physical dimensions is performed using the CST simulator [8] in order to meet the exact desired response. Because the initial response is very close to the desired response, less than 100 iterations are required to meet the desired response. In addition, the structure here is symmetric and relatively simple, it is therefore each iteration does not take long (around 1-2 minutes) when using a personal computer with the following specifications: (Processor: Intel(R) Core(TM) i5-3570 CPU @3.40 GHz, Installed memory (RAM): 8.00 GB). After the adjustment, the optimised response is in excellent agreement with the desired response (Figure 3.15 (b)). There are still some differences noticed in the S_{21} response around the start band frequency. This occurs due to the capacitive irises resonate at the TE_{10} mode cut-off frequency [3], and reduces the attenuation of the S_{21} at that start frequency (Figure 3.15 (b)).

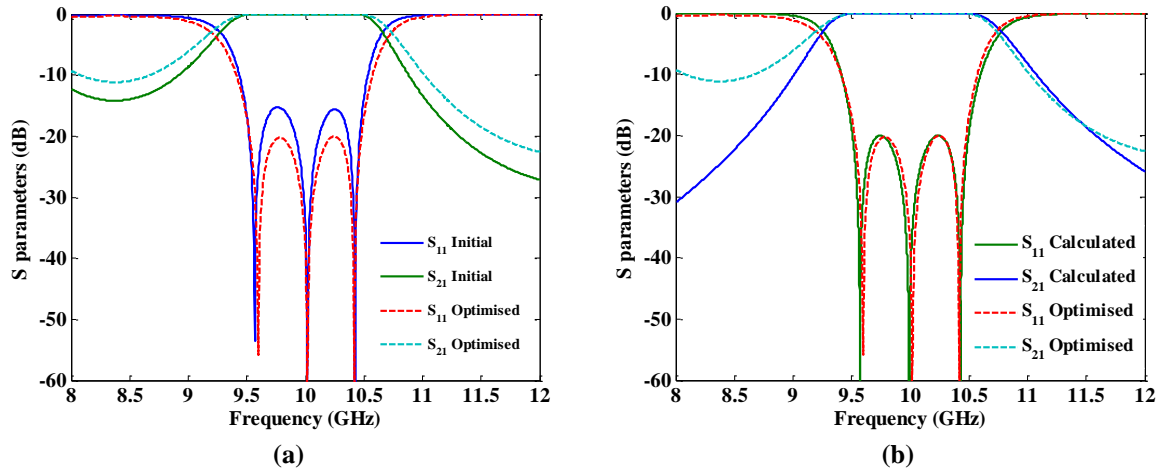


Figure 3.15: Initial response compared with the optimisation, (b) optimised response compared with the ideal response obtained from the coupling matrix.

3.5 Antenna-filter integration overview

This section discusses the main topic of this thesis, which is the integration of antennas with Bandpass filters (BPF). The main purposes of the integration are mostly to enhance the performance of communication systems, and reduce the size of the circuits.

In general, the main role of an antenna in a communication system is to receive and transmit EM waves, while the purposes of the front-end BPF are to attenuate the signals which are out of the required band whilst minimising attenuation within the required band. The front-end BPF is usually placed after the antenna. Conventionally, a matching circuit is employed in order to cascade them efficiently, and this is depicted in Figure 3.16. It should be pointed out that the input impedance of a conventional antenna is usually frequency dependent, whilst, for a BPF, it is designed for a certain value over the frequency band of interest. If their input impedances are not matched, degradation in the frequency response of the antenna and the system takes place.

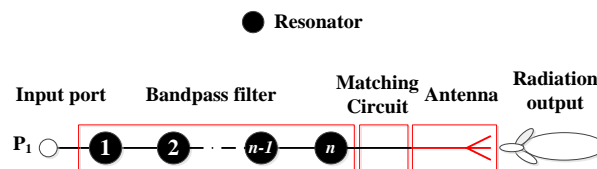


Figure 3.16: Topology shows the conventional way for the integration of an antenna with a bandpass filter using a matching circuit.

With the integration of an antenna with a BPF some important enhancements can be achieved such as; improved frequency response of the antenna, remove the need for a separate matching circuit between the antenna and the BPF (see Figure 3.17), and also reduce the total system size.

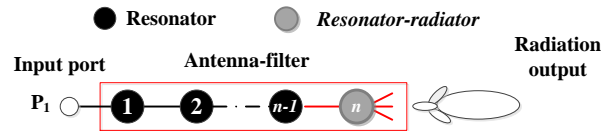


Figure 3.17: New approach of the integration of an antenna with a filter based on the coupled resonators circuit.

The integration of antennas with BPFs has been investigated extensively in the last few decades, and the filter synthesis principles are widely utilised in most of the investigations as a design tool.

Due to their flexibility in design and lightness in weight, microstrip patch antennas have been utilised to integrate with filters. In [9], a design technique is presented to integrate a microstrip patch antenna with three coplanar waveguide resonator filters. Then later in [10, 11], the synthesis procedure of bandpass filters is used to design a single and a 2×2 filtering microstrip patch antenna array. One of the drawbacks of the microstrip patch antennas is the losses from the feeding network which are significant particularly at millimetre wave frequencies. In addition, they are considered as the inherent narrow bandwidth antennas. Thus, some attempts to enhance the bandwidth of the integrated microstrip antennas were reported in [12, 13].

In [14, 15], slot antennas were integrated with 3-D waveguide cavity filters. The main purposes of the use of the 3-D cavity were to realise high Q value of the filter, reduce the circuit area, and construct a more compact *antenna-filter* component. For further reduction in the size of the component, the authors in [16, 17] integrated the slot antennas with cavities vertically. Another technique to obtain high Q of the integrated filter with slot antennas was reported in [18, 19]. Later, different types of antennas were contributed with the integration of

filters such as the dipole-slot antenna [7, 20, 21], monopole antennas [22], and some various shapes of printed antennas like the Γ -shape antenna [23, 24], and the inverted-L shape antenna [25].

A new design technique for reconfigurable open-ended evanescent waveguide antennas was presented in [26]. In this technique, an iris was employed to accomplish tuning together with matching. In [27, 28], the BPF concept was applied to the antenna given in [26] to integrate with waveguide cavity resonators, and to enhance the bandwidth of the evanescent-mode waveguide aperture antenna. Following that, another technique to enhance the bandwidth of an open-ended waveguide aperture antenna integrated with the 3rd order substrate integrated waveguide filter was presented in [29]. This technique was based on reducing the external Q_e value of the filter by using the excitation of the surface waves.

One of the main challenges of the concept of the integration of antennas with filters is its implementation for high gain antenna array due to the complex feeding network required to feed multi-radiating elements. It is discussed in [11] that using a complex feeding network causes some unexpected resonances and degrade the passband gain response of the antenna array. To overcome this, filtering feeding networks is considered as one of the better solutions. In this way, besides feeding the multi-radiating elements, the feeding networks have additional functions which are the selection of the required frequency band, and remove the need for external BPFs.

It was mentioned in Section 3.2 that the main use of the coupling matrix approach is to design filters that are made of coupled-resonators. This thesis uses this approach, as a new technique, to integrate antennas with coupled-resonators filters. The last resonator of the coupled-

resonators filter circuit opens to space and to radiate. The coupling between the last resonator and the space is analysed in detail in the following sections.

3.6 Radiation quality factor calculation of a cavity resonator-based aperture antenna

This section focuses on the calculation of the quality factors of a single cavity *resonator-radiator* when it is coupled only to a single external port, using the magnitude of the reflection coefficient S_{11} . The calculation of Q for a two-port cavity resonator can simply be performed by using the magnitude of the transmission coefficient S_{21} , and is well explained in sections 3.4.1 and 3.4.2. However, in some design situations the S_{21} parameter is not available, such as for antenna designs. Therefore an alternative technique is necessary.

A waveguide cavity *resonator-radiator*, which is shown in Figure 3.18, is designed here using the CST simulator. It's loaded quality factor Q_l can be calculated by [7]:

$$\frac{1}{Q_l} = \frac{1}{Q_e} + \frac{1}{Q_0} \quad (3.38)$$

Here, Q_e and Q_0 are the external and unloaded quality factors. The Q_0 value, based on the magnitude of S_{11} of the cavity, can be computed by [30]:

$$Q_0 = \frac{1}{|\Delta f_a|} \left[\frac{|S_{11}(f_a)|^2 (1 + \beta)^2 - (1 - \beta)^2}{1 - |S_{11}(f_a)|^2} \right]^{1/2} \quad (3.39)$$

where, $\Delta f_a = 1 - (f_0^2/f_a^2)$, f_0 is the resonant frequency, and f_a is some frequency around the resonant frequency (see Figure 3.19 (a)). The coupling coefficient β between the external circuit and the *resonator-radiator* can be given by [30]:

$$\beta = \frac{\text{Average power loss to external circuit } (P_e)}{\text{Average power loss in cavity } (P_0)} \quad (3.40)$$

or

$$\beta = \frac{P_e}{P_0} = \frac{Q_0}{Q_e} \quad (3.41)$$

In the structure shown in Figure 3.18, a capacitive iris is used to couple the *resonator-radiator* to the input port. For the calculation of the Q_0 , it is assumed that the *resonator-radiator* is weakly coupled to the port. This leads us to an approximation that the value of Q_e approaches to infinity. This means the β value vanishes ($\beta \cong 0$). After applying this approximation into Equation 3.38, we can now assume that $Q_l = Q_0$. In addition to this, the *resonator-radiator* is designed here to be air filled ($Q_d = \infty$), and the material used to model it in CST is PEC ($Q_c = \infty$). In this case, according to Equation 3.28, the radiation quality factor Q_r is equal to unloaded quality factors Q_0 , $Q_r = Q_0$. This time the Q_r is obtained from the radiating port. Equation 3.39 can now be used to calculate the radiation Q_r factor of the *resonator-radiator*. To obtain the values of β and f_a parameters in Equations 3.39, more details can be found in [30].

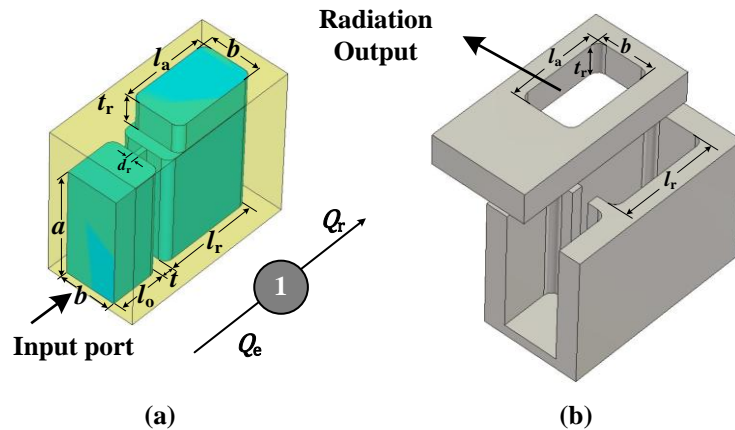


Figure 3.18: Layout of a single resonator-radiator fed weakly from one side and opened to space at another side via an aperture. The structure is resonated at centre frequency 10 GHz with the dimensions; $a = 22.86$ mm, $b = 10.16$ mm, $d_r = 1$ mm, $l_0 = 10.16$ mm, and $t = 2$ mm. (a) the outstanding structure in the central area represents the hollow waveguide WR-90 and an aperture, while the surrounding conductors are set to be transparent). (b) The real structure.

The physical dimensions (l_a , and l_r) of the *resonator-radiator*, which are labelled in Figure 3.18, are utilised to control the Q_r . The variation of Q_r versus l_a is plotted in Figure 3.19 (b), and it can be seen that the Q_r value dramatically increases when l_a is reduced. The length l_r is tuned to keep f_0 at centre frequency 10 GHz.

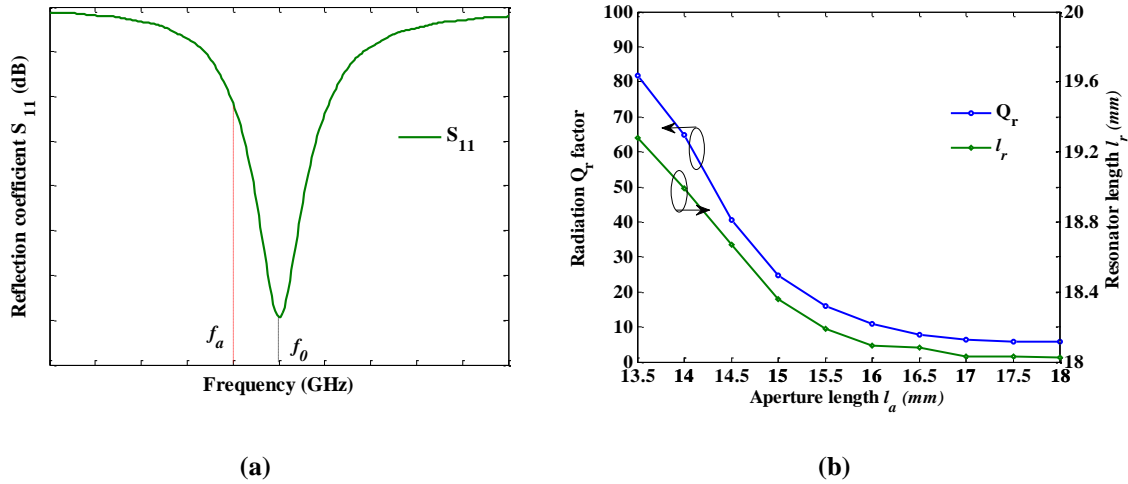


Figure 3.19: (a) Frequency response S_{11} of the waveguide cavity *resonator-radiator* shown in Figure 3.18, (b) Extraction of the radiation quality factor Q_r of the *resonator-radiator* shown in Figure 3.18 based on the magnitude of S_{11} for different l_a values with simultaneous change of l_r to keep the resonant frequency at (10 GHz); $t_r = 10\text{mm}$, $a = 22.86\text{ mm}$, $b = 10.16\text{ mm}$, $l_0 = 10.16\text{ mm}$, $d_r = 1\text{mm}$.

3.7 Coupling matrix representation for *antenna-filter* integration

This section presents the topologies and their corresponding coupling matrices for an *antenna-filter* and *antenna array-filter* components. The designs of filters are usually based on the coupled-resonators circuit as discussed in Section 3.2. In general, the topology for a two-port filter circuit based on the n coupled-resonators is represented in the form as shown in Figure 3.20 (a). Its corresponding coupling matrix can also be derived, as explained in Section 3.2, and is given here in Equation 3.42.

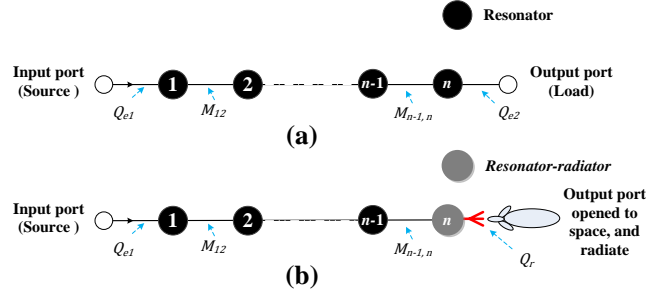


Figure 3.20: (a) Topology of an n -coupled resonator filter, (b) topology of *antenna-filter* component made out of n -coupled resonator.

$$[A] = \begin{bmatrix} \frac{1}{q_{e1}} & 0 & \dots & 0 \\ q_{e1} & 0 & \dots & 0 \\ 0 & 0 & \dots & 0 \\ \vdots & \vdots & \ddots & \vdots \\ 0 & 0 & \dots & \frac{1}{q_{en}} \end{bmatrix} + p \begin{bmatrix} 1 & 0 & \dots & 0 \\ 0 & 1 & \dots & 0 \\ \vdots & \vdots & \ddots & \vdots \\ 0 & 0 & \dots & 1 \end{bmatrix} - j \begin{bmatrix} m_{11} & m_{12} & \dots & m_{1n} \\ m_{21} & m_{22} & \dots & m_{2n} \\ \vdots & \vdots & \ddots & \vdots \\ m_{n1} & m_{n2} & \dots & m_{nn} \end{bmatrix} \quad (3.42)$$

Once the second port (output port) of the filter is removed, the last resonator of the filter starts radiating into space (see Figure 3.20 (b)). This resonator has been called *resonator-radiator* in this work. The *resonator-radiator* has a radiation quality factor Q_r which can be calculated following the technique given in the previous section.

When the resonant frequency of the *resonator-radiator* is kept the same as the filter, and its radiation Q_r is made to be equal to the external Q_e of the bandpass filter, the *resonator-radiator* can act as the last resonator of the filter and as an antenna (radiator) simultaneously. This component is named an *antenna-filter* due to carrying both functions of the components. The coupling matrix for the *antenna-filter* component remains the same as the two-port coupled-resonators filter, except that the external output q_e is replaced by the radiation q_{rn} , and is shown in Equation 3.43.

$$[A] = \begin{bmatrix} \frac{1}{q_{e1}} & 0 & \dots & 0 \\ q_{e1} & 0 & \dots & 0 \\ 0 & 0 & \dots & 0 \\ \vdots & \vdots & \ddots & \vdots \\ 0 & 0 & \dots & \frac{1}{q_{rn}} \end{bmatrix} + p \begin{bmatrix} 1 & 0 & \dots & 0 \\ 0 & 1 & \dots & 0 \\ \vdots & \vdots & \ddots & \vdots \\ 0 & 0 & \dots & 1 \end{bmatrix} - j \begin{bmatrix} m_{11} & m_{12} & \dots & m_{1n} \\ m_{21} & m_{22} & \dots & m_{2n} \\ \vdots & \vdots & \ddots & \vdots \\ m_{n1} & m_{n2} & \dots & m_{nn} \end{bmatrix} \quad (3.43)$$

The reflection coefficient S_{11} remains the same as the one used for the two-port coupled resonator filters, and is given below [2]:

$$S_{11} = \pm \left(1 - \frac{2}{q_{e1}}\right) \cdot [A]_{11}^{-1} \quad (3.44)$$

It is worth mentioning here that the response of the realised gain obtained from the *antenna-filter* component could agree with the transmission response of its equivalent filter based on coupled-resonators circuit, except that some gain is added within the passband. This can clearly be recognised in Chapters 4 and 5.

It is possible to design a multiple-output power splitter component based on the coupled-resonators using the coupling matrix approach as explained in [31, 32]. A topology is given in Figure 3.21 (a) for this purpose. Its corresponding coupling matrix can also be derived, and is given in Equation 3.45.

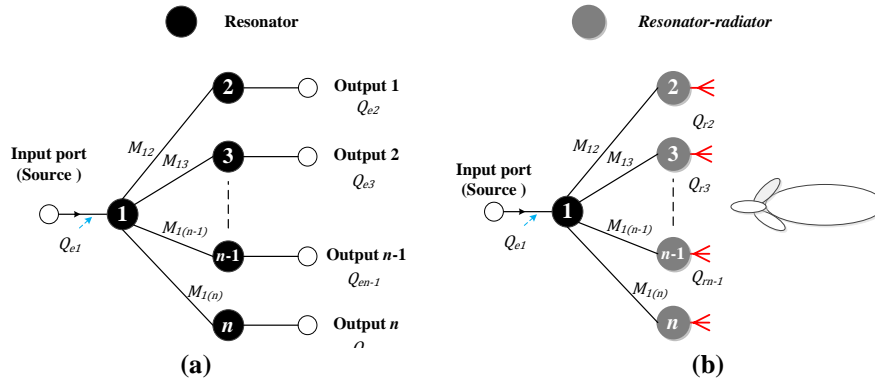


Figure 3.21: (a) Topology of a multiple-output circuit based on n -coupled resonator filter, (b) topology of an antenna array-filter component made out of n -coupled resonator.

$$[A] = \begin{bmatrix} \frac{1}{q_{e1}} & \dots & 0 & 0 \\ \vdots & \ddots & \vdots & \vdots \\ 0 & \dots & \frac{1}{q_{e(n-1)}} & \vdots \\ 0 & \dots & 0 & \frac{1}{q_{en}} \end{bmatrix} + p \begin{bmatrix} 1 & \dots & 0 & 0 \\ \vdots & \ddots & \vdots & \vdots \\ \dots & \dots & 1 & \vdots \\ 0 & \dots & 0 & 1 \end{bmatrix} - j \begin{bmatrix} m_{11} & \dots & m_{1(n-1)} & m_{1n} \\ \vdots & \ddots & \vdots & \vdots \\ m_{(n-1)1} & \dots & m_{(n-1)(n-1)} & m_{(n-1)n} \\ m_{n1} & \dots & m_{n(n-1)} & m_{nn} \end{bmatrix} \quad (3.45)$$

Similarly, when the output ports of the power splitter are opened to space, they start radiating, and then the topology converts to the one shown in Figure 3.21 (b). Again, if the last resonators of each output of the power splitter has a Q_r equal to the Q_e of the power splitter ($Q_r = Q_e$), they keep their main function in addition to the radiation. The component produced through this technique is named an *antenna array-filter*. The coupling matrix for the *antenna array-filter* can now be modified into the following.

$$[A] = \begin{bmatrix} \frac{1}{q_{e1}} & \dots & 0 & 0 \\ \vdots & \ddots & \vdots & \vdots \\ 0 & \dots & \frac{1}{q_{r(n-1)}} & \vdots \\ 0 & \dots & 0 & \frac{1}{q_{rn}} \end{bmatrix} + p \begin{bmatrix} 1 & \dots & 0 & 0 \\ \vdots & \ddots & \vdots & \vdots \\ \dots & \dots & 1 & \vdots \\ 0 & \dots & 0 & 1 \end{bmatrix} - j \begin{bmatrix} m_{11} & \dots & m_{1(n-1)} & m_{1n} \\ \vdots & \ddots & \vdots & \vdots \\ m_{(n-1)1} & \dots & m_{(n-1)(n-1)} & m_{(n-1)n} \\ m_{n1} & \dots & m_{n(n-1)} & m_{nn} \end{bmatrix} \quad (3.46)$$

3.8 Conclusions

In this Chapter, an overview through the basic theory of filters and the coupling matrix approach were provided. This was followed by the synthesis technique used to design two-port coupled-resonators filters. Based on this synthesis technique, design of a 3rd order rectangular waveguide filter has been presented, and its performance has been characterised. The simulated frequency response of the designed filter was very close to the calculated response. The calculation of the Q_r using the magnitude of S_{11} for a *resonator-radiator* was discussed. A quick review through some investigations conducted on the integration of antennas with filters was also performed. A new synthesis approach for the integration of antennas with filters was developed in this Chapter. The new approach will be used in Chapters 4 and 5 to design the *antenna-filter* and *antenna array-filter* components.

3.9 References

1. Pozar, D.M., *Microwave engineering*. 2009: John Wiley & Sons.
2. Hong, J.-S.G. and M.J. Lancaster, *Microstrip filters for RF/microwave applications*. Vol. 167. 2004: John Wiley & Sons.
3. Shang, X., *SU-8 micromachined terahertz waveguide circuits and coupling matrix design of multiple passband filters*. 2011, University of Birmingham.
4. Williams, A.E. *A four-cavity elliptic waveguide filter*. in *G-MTT 1970 International Microwave Symposium*. 1970.
5. Atia, A.E. and A.E. Williams, *Narrow-bandpass waveguide filters*. *Microwave Theory and Techniques, IEEE Transactions on*, 1972. **20**(4): p. 258-265.
6. Xia, W., *Diplexers and multiplexers design by using coupling matrix optimisation*. 2015, University of Birmingham.
7. Nugoolcharoenlap, E., *New design approach of antennas with integrated coupled resonator filters*. 2015, University of Birmingham.
8. Studio, C.M., *Computer simulation technology*. GmbH, Darmstadt, Germany, 2009.
9. Abbaspour-Tamijani, A., J. Rizk, and G. Rebeiz. *Integration of filters and microstrip antennas*. in *Antennas and Propagation Society International Symposium, 2002. IEEE*. 2002. IEEE.
10. Lin, C.-K. and S.-J. Chung. *A compact edge-fed filtering microstrip antenna with 0.2 dB equal-ripple response*. in *Microwave Conference, 2009. EuMC 2009. European*. 2009. IEEE.
11. Lin, C.-K. and S.-J. Chung, *A filtering microstrip antenna array*. *Microwave Theory and Techniques, IEEE Transactions on*, 2011. **59**(11): p. 2856-2863.
12. Tong, K.-F., et al., *A broad-band U-slot rectangular patch antenna on a microwave substrate*. *Antennas and Propagation, IEEE Transactions on*, 2000. **48**(6): p. 954-960.
13. Deslandes, D. and K. Wu, *Single-substrate integration technique of planar circuits and waveguide filters*. *Microwave Theory and Techniques, IEEE Transactions on*, 2003. **51**(2): p. 593-596.
14. Yusuf, Y. and X. Gong. *A new class of 3-D filter/antenna integration with high quality factor and high efficiency*. in *Microwave Symposium Digest (MTT), 2010 IEEE MTT-S International*. 2010. IEEE.
15. Yusuf, Y. and X. Gong, *Compact Low-Loss Integration of High-3-D Filters With Highly Efficient Antennas*. *Microwave Theory and Techniques, IEEE Transactions on*, 2011. **59**(4): p. 857-865.
16. Yusuf, Y., H. Cheng, and X. Gong, *A seamless integration of 3-D vertical filters with highly efficient slot antennas*. *Antennas and Propagation, IEEE Transactions on*, 2011. **59**(11): p. 4016-4022.
17. Cheng, H., Y. Yusuf, and X. Gong, *Vertically integrated three-pole filter/antennas for array applications*. *Antennas and Wireless Propagation Letters, IEEE*, 2011. **10**: p. 278-281.

18. Yusuf, Y. and X. Gong. *A vertical integration of high-Q filters with patch antennas with enhanced bandwidth and high efficiency*. in *Microwave Symposium Digest (MTT), 2011 IEEE MTT-S International*. 2011. IEEE.
19. Yusuf, Y., H. Cheng, and X. Gong, *Co-designed substrate-integrated waveguide filters with patch antennas*. *IET Microwaves, Antennas & Propagation*, 2013. **7**(7): p. 493-501.
20. Oda, S., et al., *Electrically small superconducting antennas with bandpass filters*. *Applied Superconductivity*, IEEE Transactions on, 2007. **17**(2): p. 878-881.
21. Nadan, T.L., et al. *Integration of an antenna/filter device, using a multi-layer, multi-technology process*. in *Microwave Conference, 1998. 28th European*. 1998. IEEE.
22. Chuang, C.-T. and S.-J. Chung. *New printed filtering antenna with selectivity enhancement*. in *Microwave Conference, 2009. EuMC 2009. European*. 2009. IEEE.
23. Wu, W.-J., et al., *A new compact filter-antenna for modern wireless communication systems*. *Antennas and Wireless Propagation Letters*, IEEE, 2011. **10**: p. 1131-1134.
24. Chuang, C.-T. and S.-J. Chung, *A compact printed filtering antenna using a ground-intruded coupled line resonator*. *Antennas and Propagation*, IEEE Transactions on, 2011. **59**(10): p. 3630-3637.
25. Chuang, C.-T. and S.-J. Chung, *Synthesis and design of a new printed filtering antenna*. *Antennas and Propagation*, IEEE Transactions on, 2011. **59**(3): p. 1036-1042.
26. Ludlow, P. and V. Fusco, *Reconfigurable small-aperture evanescent waveguide antenna*. *Antennas and Propagation*, IEEE Transactions on, 2011. **59**(12): p. 4815-4819.
27. Ludlow, P., et al., *Applying band-pass filter techniques to the design of small-aperture evanescent-mode waveguide antennas*. *Antennas and Propagation*, IEEE Transactions on, 2013. **61**(1): p. 134-142.
28. Ludlow, P., et al., *Small aperture evanescent-mode waveguide antenna matched using distributed coupled resonators*. *Electronics Letters*, 2013. **49**(9): p. 580-582.
29. Yusuf, Y. and X. Gong, *Integration of three-dimensional high-Q filters with aperture antennas and bandwidth enhancement utilising surface waves*. *IET Microwaves, Antennas & Propagation*, 2013. **7**(7): p. 468-475.
30. Lancaster, M.J., *Passive microwave device applications of high-temperature superconductors*. 2006: Cambridge University Press.
31. Skaik, T., M.J. Lancaster, and F. Huang, *Synthesis of multiple output coupled resonator circuits using coupling matrix optimisation*. *IET microwaves, antennas & propagation*, 2011. **5**(9): p. 1081-1088.
32. Skaik, T., *Synthesis of coupled resonator circuits with multiple outputs using coupling matrix optimization*. 2011, University of Birmingham.

Chapter 4

Waveguide aperture antenna array design

This chapter presents the topology, design, and measurement of four *antenna-filter* and *antenna array-filter* components based on the new design technique given in Chapter 3. The components are the 3rd order *antenna-filter*, 2nd order *antenna array-filter*, 3rd order 2×2 *antenna array-filter*, and the 7th order 4×4 *antenna array-filter*. These are formed from four novel topologies chosen in such a way as to reduce the circuit sizes as much as possible and to facilitate the fabrication process. Rectangular waveguide cavity resonators have been utilised to realise physical structures of the topologies due to the high power handling capability of waveguides and the demand of the proposed terahertz communication system for such waveguide structures. The components have the bandwidth of 10% of its operating centre frequency. Although they are designed at the X-band frequencies, they are readily scalable to terahertz frequencies.

4.1 3rd order *antenna-filter* component

The main focus of this section is on the design and fabrication of the 3rd order *antenna-filter* component.

4.1.1 Design and simulation

The topology of the 3rd order *antenna-filter* component is shown in Figure 4.1 (a). Three resonators are utilised to construct the component, and they are coupled to each other in series via capacitive irises using the technique presented in Chapter 3. The specification of the

component is chosen to: (i) operate at X- band frequencies with centre frequency 10 GHz, and (ii) have a *FBW* of 10% with the return loss level of -20 dB. From this specification, the external quality factor Q_{ei} , radiation quality factor Q_{rj} , and coupling coefficient M_{ij} of the component, which can be calculated from the Equations 3.34 and 3.37 given in Chapter 3, are $Q_e = Q_r = 8.516$, $M_{12} = M_{23} = 0.1031$. The desired frequency response can also be obtained by using the coupling matrix equations (3.19, 3.20, 3.23, and 3.24), and is plotted in Figure 4.2 (b).

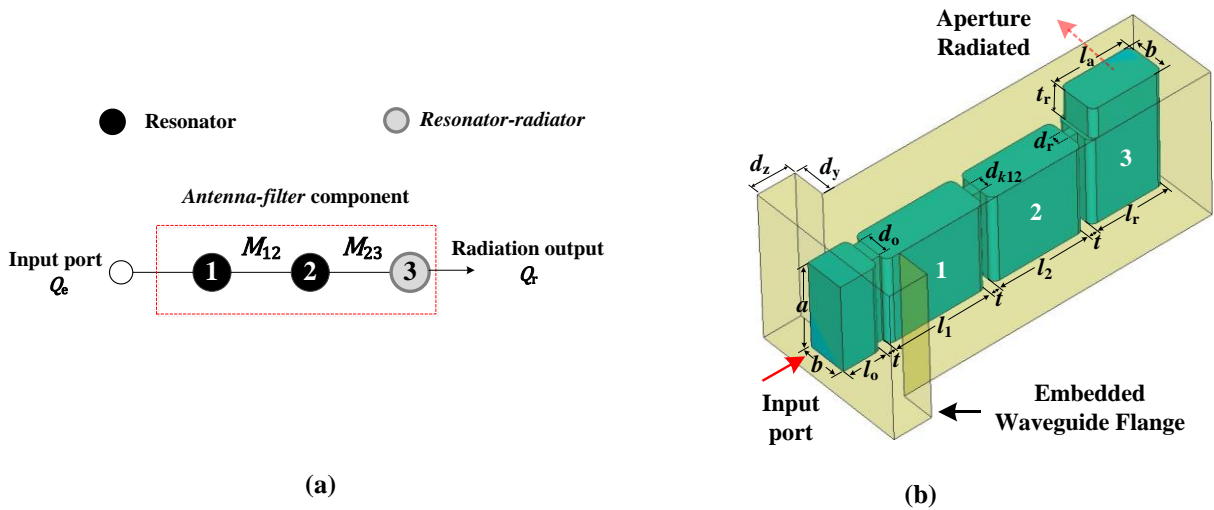


Figure 4.1: (a) Proposed topology for the 3rd order *antenna-filter* component. Resonator 3 (grey) acts as a radiator as well as the last resonator. (b) Physical configuration. Dimensions in mm are: $a = 22.86$, $b = 10.16$, $t = 2$, $l_o = 15$, $d_y = 8.62$, $d_z = 88.32$, other dimensions can be found in Table 4.1, radius of the round corners = 1.6.

$$m = \begin{bmatrix} 0 & 1.031 & 0 \\ 1.031 & 0 & 1.031 \\ 0 & 1.031 & 0 \end{bmatrix}$$

$$q_r = q_e = 0.8516$$

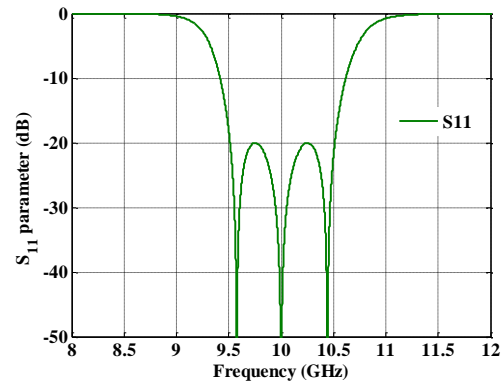


Figure 4.2: (a) Equivalent coupling matrix for the 3rd order *antenna-filter* component, (b) Ideal response of the reflection coefficient S_{11} of the 3rd order *antenna-filter* component.

The Computer Simulation Technology (CST) simulator [1] has been used to extract the initial dimensions corresponding to the coupling parameters of the component shown in Figure 4.1 (b) using the technique discussed in Chapter 3. Resonator 1 which is coupled to the input port via a capacitive iris is designed separately in order to find the equivalent aperture dimension (d_0) for the external Q_e . Moreover, resonators 1 and 2 are coupled to each other via a capacitive iris, and the technique given in Section 3.4.2 in Chapter 3 was used to find the aperture width d_{k12} . A similar technique was also used to obtain the dimension of the d_{k23} . To find the l_a dimension of the component, the technique presented in Section 3.6 of Chapter 3 is used for this purpose.

Table 4.1 summaries the initial dimensions of the component. The initial frequency response S_{11} of the component is obtained using the time domain solver in the CST simulator, and is shown in Figure 4.3 (a). It is fairly close to the desired response. To meet the exact desired S_{11} response, Adjustments for the component dimensions have been undertaken using the optimiser tool in the CST simulator [1]. The goals for the optimisation have been defined as follows: $S_{11} \gg -20$ (from 8.0-9.49 GHz), $S_{11} \ll -20$ (from 9.50-10.50 GHz), $S_{11} \gg -20$ (from 10.51-12.0 GHz). There are seven physical parameters which need to be optimised (see Table 4.1). For each physical parameter, a range (≈ 1.0 mm) is chosen to be tuned. After nearly 100 iterations, a very good response for the S_{11} parameter of the component was obtained, and it is compared with the desired response in Figure 4.3 (b).

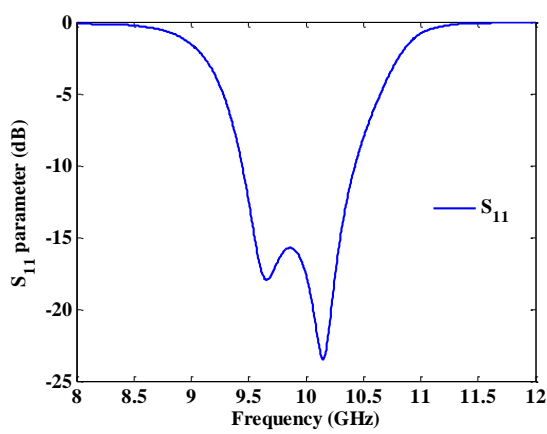
The simulated total efficiency (including the losses caused due to the mismatch) of the component is shown in Figure 4.3 (c), and it is more than 95% over the passband. It should be pointed out that the total efficiency variation manner is similar to the transmission coefficient of a bandpass filter. This is due to the filtering functionality of the component, achieving well-

matching of the return loss (-20 dB) over the passband.

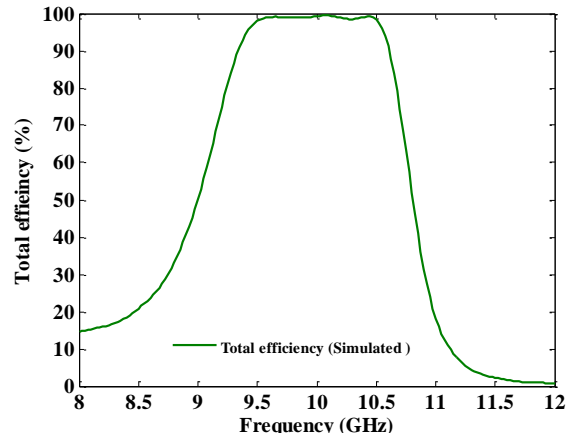
Table 4.1

Physical dimensions of the 3rd order *antenna-filter* component shown in Figure 4.1 (b).

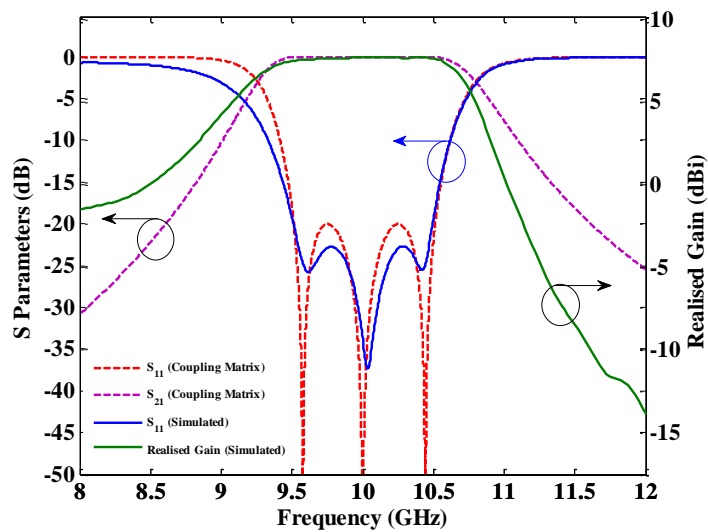
| Parameters | Initial values (mm) | Optimised values (mm) |
|-------------------------------------|---------------------|-----------------------|
| Iris width (d_0) | 4.52 | 6.0 |
| Coupling Iris width (d_{12}) | 2.26 | 3.18 |
| Coupling Iris width (d_{23}) | 2.20 | 2.31 |
| Cavity resonator length (l_1) | 24.70 | 26.00 |
| Cavity resonator length (l_2) | 23.73 | 24.47 |
| Resonator-radiator length (l_r) | 19.10 | 19.85 |
| Radiating aperture length (l_a) | 18.0 | 19.0 |



(a)



(c)



(b)

Figure 4.3: (a) The initial simulated response of S_{11} parameter of the 3rd order *antenna-filter* component, (b) The optimised response compared with the calculated, (c) Simulated total efficiency versus frequency.

4.1.2 Fabrication and measurement

The 3rd order *antenna-filter* component has been fabricated using the Computer Numerical Control (CNC) milling machine in the School of Physics at the University of Birmingham. The tolerance of the machine is about ± 0.02 mm. The material used to fabricate the component is Aluminium Alloy 6082 (RS components). The component has been cut into the centre of the broad wall of the waveguide (zero current line zones), and split into two pieces to facilitate the fabrication process as can be seen in Figure 4.4 (a). Metal screws are used to assemble the pieces, and they are inserted from the bottom in order to minimise their effects on the radiation performance.

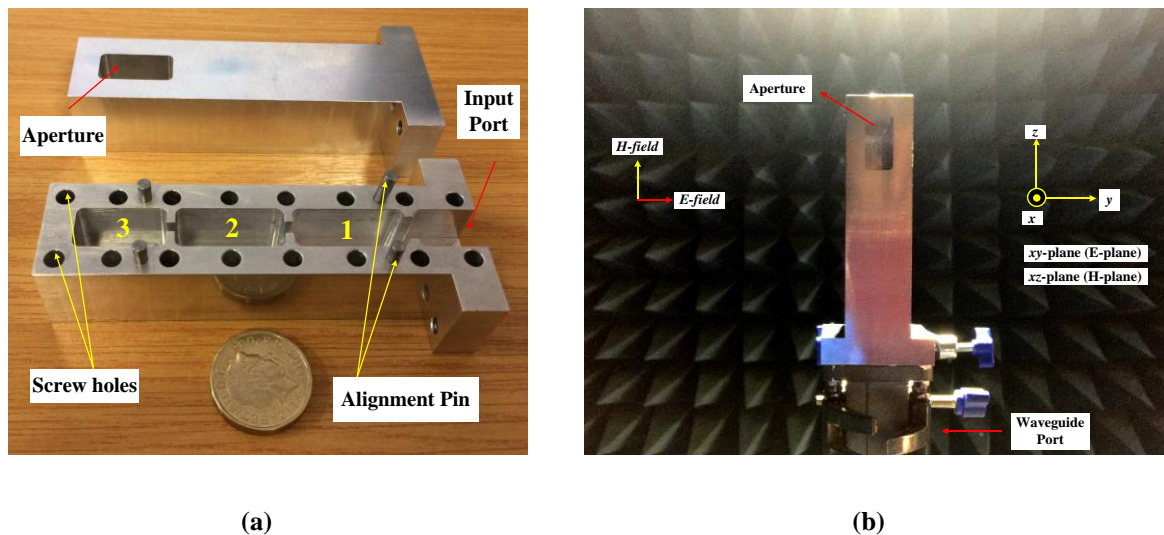


Figure 4.4: (a) Photograph of the fabricated 3rd order *antenna-filter* component, (b) The component under test.

The measured return loss S_{11} of the component compared with the simulated is presented in Figure 4.5 (a), and a very good agreement over the entire operating frequency band is achieved. The measured response of S_{11} is shifted to slightly higher frequencies, which could be due to the fabrication tolerance. Moreover, the realised gain is measured using the well-known comparison method. A broad band horn antenna was used as the reference antenna,

and the fabricated antenna was placed in the far-field region. The measured gain versus frequencies is compared with simulated in Figure 4.5 (b), and a good agreement is also depicted, having almost constant gain (7.49-7.67 dBi) over the passband. The 3-dB gain bandwidth is 17.61 %.

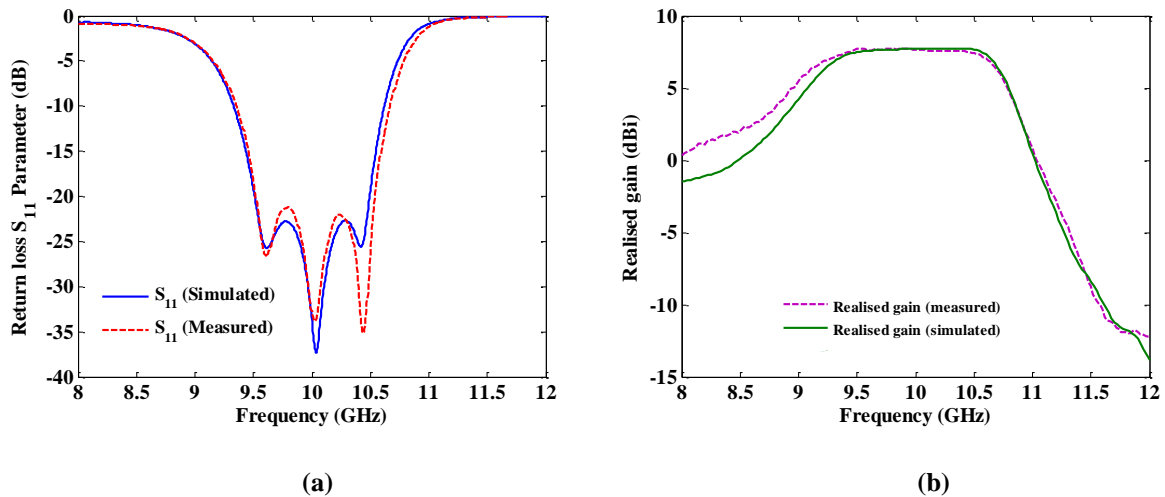


Figure 4.5: (a) Measured return loss compared with simulated, (b) Measured realised gain of the compared with simulated.

The measurement for the radiation pattern for both E- and H-planes is performed at three different frequencies within the passband frequency range, and they are compared with the simulations in Figure 4.6. There is a good agreement between the simulation and measurement depicted. The side lobe levels of the presented radiation patterns are below -11 dB. During the measurement, the waveguide port (adapter) connected to the component (see Figure 4.4 (b)) was covered by a piece of absorber to minimise reflection and discrepancy between the simulation and measurement. It should be pointed out that the asymmetry of the radiation pattern in the H-plane, which can clearly be identified in both the simulation and measurement, is due to the asymmetric physical structure of the component.

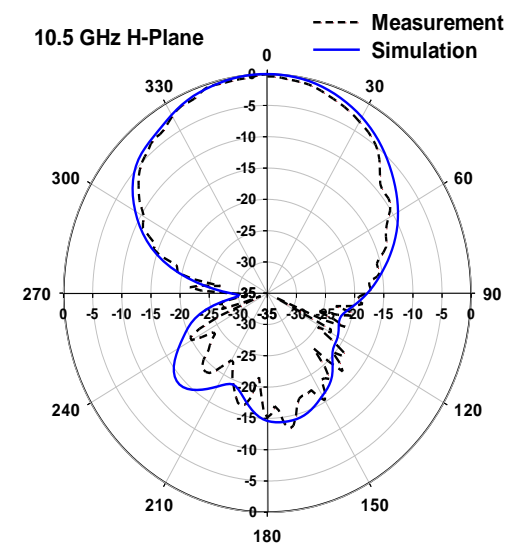
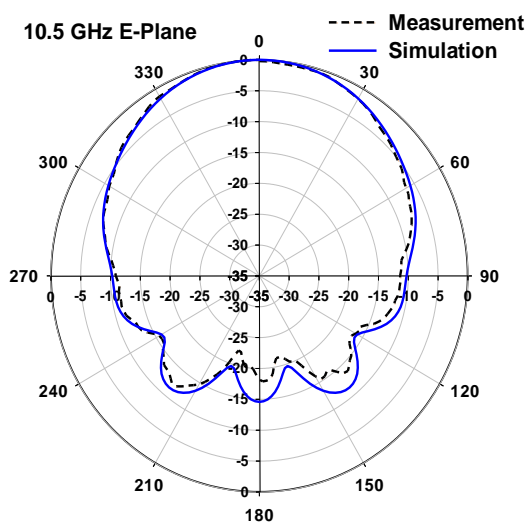
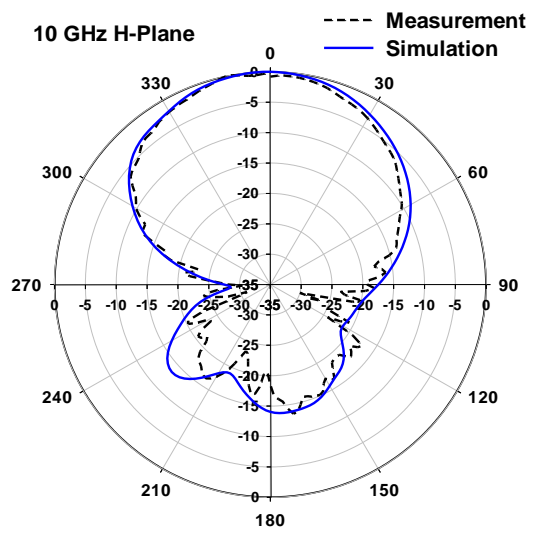
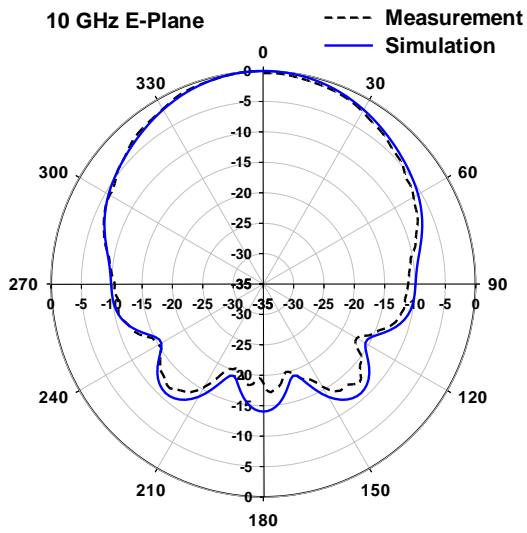
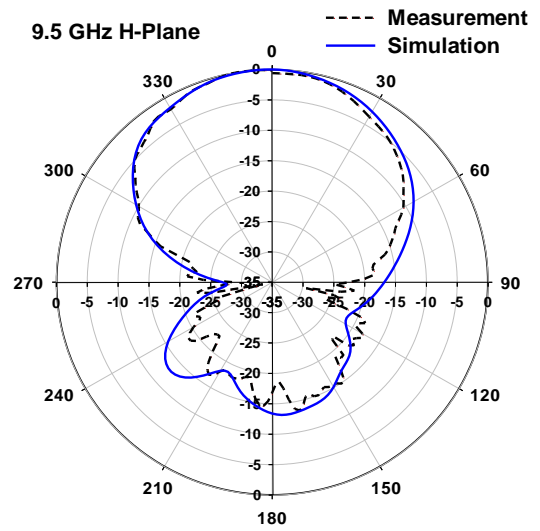
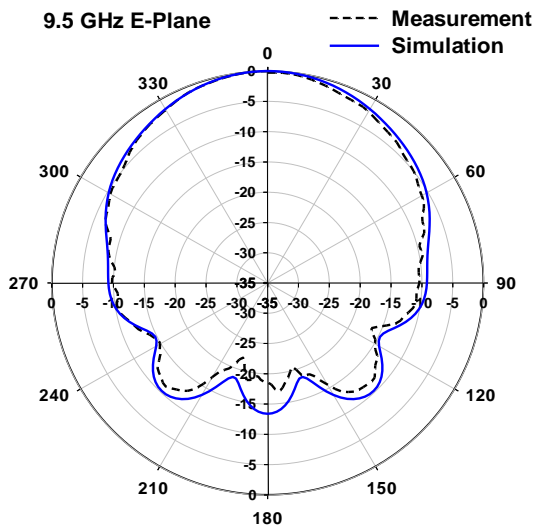


Figure 4.6: Measured radiation pattern of the 3rd order *antenna-filter* component for both the E- and H-planes at three frequencies including the centre frequency.

4.2 2nd order *antenna array-filter* component

In the previous section, the design and radiation characteristics of the 3rd order *antenna-filter* component were discussed and analysed. It has only a single *resonator-radiator* (single radiating element). As a result of that, it has provided a low value of gain and directivity. The design of an antenna with a very directive radiation characteristic (high gain) is necessary in this work. Hence, an antenna array is considered here to be one of the appropriate ways to increase the gain. In the following sub-sections, the design of a simple array (two-element array) named the 2nd order *antenna array-filter* component is presented, and its radiation characteristic is analysed.

4.2.1 Design and simulation

The design of the 2nd order *antenna array-filter* component is presented in this sub-section. It consists of three resonators arranged in a way to form a simple antenna array as illustrated in Figure 4.7 (a). Two of them act as *resonator-radiators*, and they are spaced by $0.5\lambda_0$. The concept of power splitter based on coupled-resonators, which is presented in Chapter 3, is utilised in the design and to obtain the equivalent coupling matrix. The component is designed to have 10% *FBW* at a centre frequency of 10 GHz, and -20 dB return loss level within the passband. To obtain the normalised non-zero entries of the coupling matrix, a gradient-based optimisation technique is used [2], and gives: $m_{12} = m_{13} = 1.175$. The scaled external and radiation quality factors are $q_e = q_{r1} = q_{r2} = 0.6648$.

The simulated return loss and realised gain of the component are obtained using the CST simulator, and plotted in Figure 4.8 (a). They are very comparable with the desired response

obtained from the coupling matrix. The simulated total efficiency of the component is shown in Figure 4.8 (b), and it is more than 90 % over the bandwidth of interest. Again, its manner is similar to the filtering functionality of the realised gain.

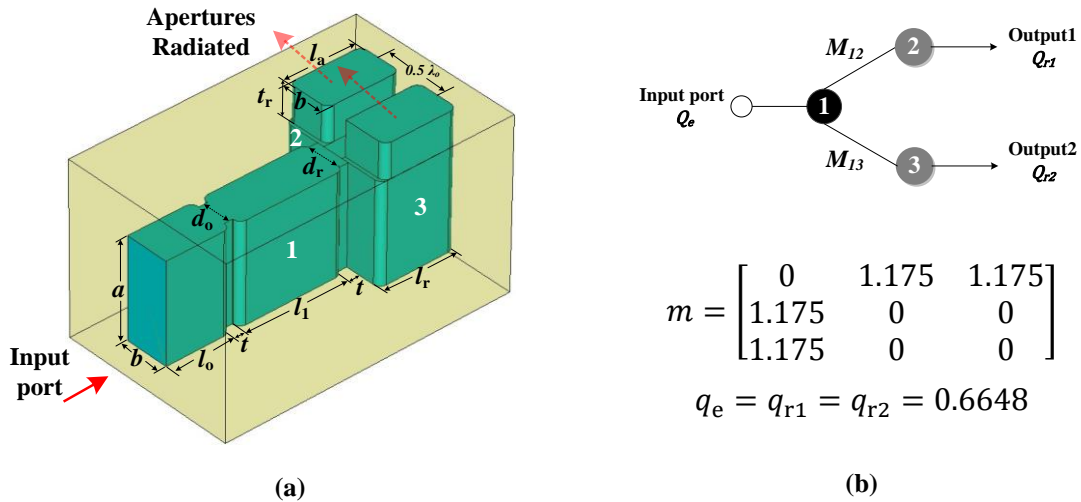


Figure 4.7: (a) Physical configuration, and (b) Equivalent topology and scaled coupling matrix of the 2nd order *antenna array-filter* component. Dimensions in mm are: $a = 22.86$, $b = 10.16$, $t = 2$, $t_r = 10$, $d_o = 6.62$, $d_r = 9.30$, $l_0 = 15$, $l_1 = 24.51$, $l_r = 18$, $l_a = 17.22$, radius of the round corners = 1.6.

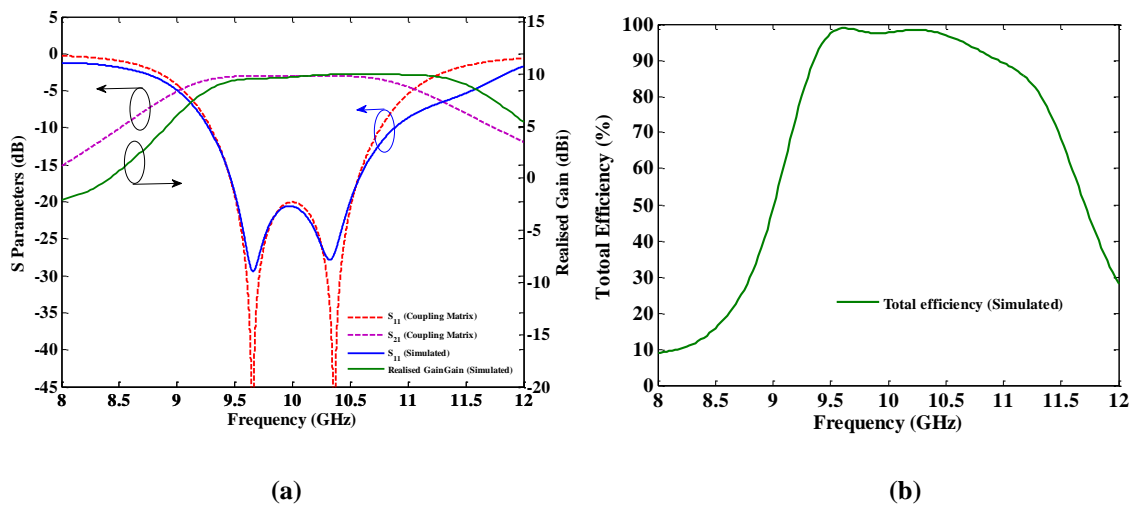
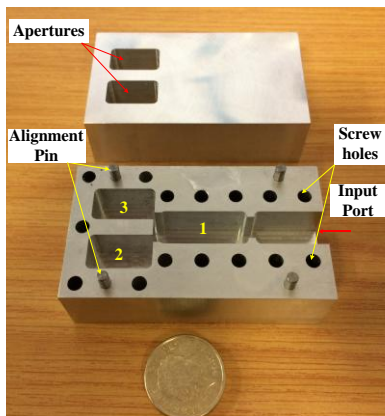


Figure 4.8: (a) Simulated return loss and realised gain of the 2nd order *antenna array-filter* component compared with obtained results from the coupling matrix, (b) Simulated total efficiency of the component versus frequencies.

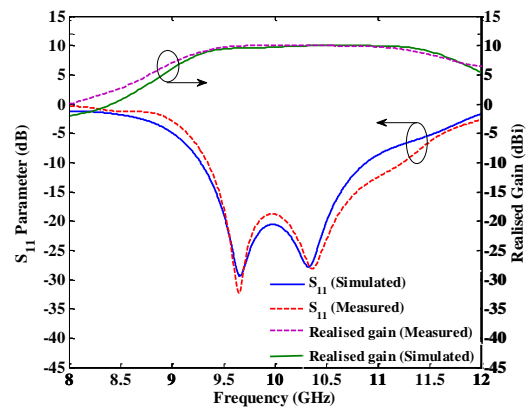
4.2.2 Fabrication and Measurement

The component has been fabricated and its radiation performance has been measured in an anechoic chamber. It is made of two pieces using the CNC milling machine (Figure 4.9 (a)). The measured realised gain and return loss are shown in Figure 4.9 (b), and compared with their simulation. A close agreement between the simulated and measured performances is identified. The component has the S_{11} response below -20 dB from 9.5 GHz to 10.5 GHz, and the 3-dB gain-bandwidth is 27 %. The realised gain fluctuates over the passband from 9.5 to 10 dBi. It should be mentioned here that the filtering functionality of the component is poor due to the fact that there are only two resonators contributing in each of the radiating path. Enhancement in the filtering functionality can be achieved by employing more resonators in each radiating path.

The radiation pattern for both the E- and H-planes at three different frequencies including the centre frequency is plotted in Figure 4.10. A very good agreement between the simulation and measurement is obtained. Because the radiating apertures are close to each other ($0.5 \lambda_0$ E-plane), a very low side lobe level, which is below -20 dB, is achieved in all the given frequencies. The asymmetry of the radiation pattern in the H-plane goes back to the asymmetric physical structure of the component on that plane.



(a)



(b)

Figure 4.9: (a) Photograph, and (b) Measured response of the 2nd order antenna array-filter component.

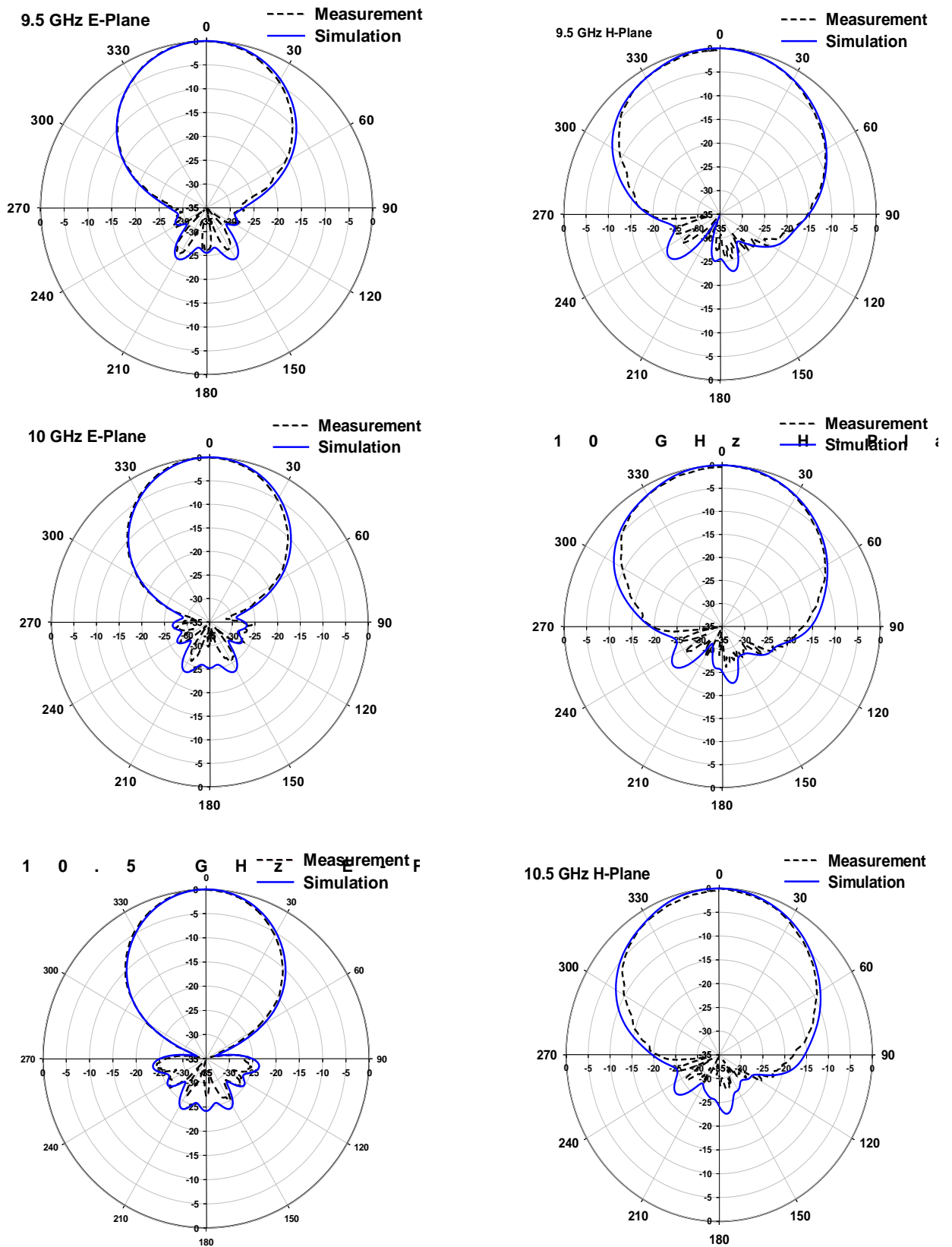


Figure 4.10: Measured radiation pattern of the 2nd order antenna array-filter component for both the E- and H-planes at three frequencies including the centre frequency.

4.3 3rd order 2×2 antenna array-filter component

After demonstrating the designs of the 3rd order *antenna-filter* and the 2nd order *antenna array-filter* components in the previous sections and improving the peak gain from 7.6 to 10 dBi, this section presents a component with more radiating elements which can improve the gain further. It is called the 3rd order 2×2 *antenna array-filter*.

To design the 2×2 *antenna array-filter* component, there are some points which need be taken into account in advance. For instance, the spacing between the radiating outputs is necessary to be close to $(\lambda_0/2)$ in order to minimise the side lobe level of the radiation pattern. In addition to this, the radiation outputs need to be arranged in a way that can keep them in phase so as to produce a constructive radiation pattern and maximise the directivity. After taking these points into account, two novel configurations for the design of the 3rd order 2×2 *antenna array-filter* component have come to our attention. In the following subsections, attention has been paid only to the first configuration (Figure 4.11), and working on the second configuration is handled to Chapter 5 (Figures 5.1 and 5.2).

4.3.1 Design and simulation

Figure 4.11 shows the topology, coupling matrix, and physical configuration of the 3rd order 2×2 *antenna array-filter* component. It consists of seven resonators that split the input power into four outputs equally using the design concept of the filtering power splitter based on the coupled-resonators as demonstrated in Chapter 3. The equivalent coupling matrix is obtained using the gradient-based optimisation technique [2], and is given in Figure 4.11 (b). The physical structure of the component is shown in Figure 4.11 (c). It is symmetric in both the E-

and H-planes. This offers significant advantages in terms of design flexibility and computation time required by the CST simulator [1].

The spacing between the outputs in both the E- and H-planes is designed to be 24.32 mm ($0.81 \lambda_0$) at the centre frequency 10 GHz. It can be shortened further by reducing the b dimension of the resonators to suppress the side lobe level. This is addressed for the second configuration of the design of the 3rd order 2×2 *antenna array-filter* component in Chapter 5 (section 5.1). Here, the standard b value ($b = 10.16$ mm) is used for the component because the main goal is to validate the design concept.

The component has 10 % *FBW* and a return loss of -20 dB over the passband (9.5-10.5 GHz). The simulated return loss and realised gain are obtained using the CST simulator, and their variation versus frequency is compared with the calculated scattering parameters in Figure 4.12 (a). The simulated S_{11} response is in excellent agreement with the calculated response. Moreover, the manner of the realised gain is also in very good agreement with the S_{21} , except that there is a transmission zero in the simulated realised gain which can clearly be noticed near the start band frequency. The way used to couple resonator 2 with resonators 4, 5 and resonator 3 with 6, 7 are responsible for the creation of such a kind of transmission zero. Investigations conducted into this kind of coupling indicate that the transmission zero occurs by creating a double path for the signal inside the resonators 2 and 3 [3-5]. It is believed that the coupling matrix approach is also able to demonstrate this kind of transmission zero [6]. This will be investigated further in the future. The variation of the simulated total efficiency of the component versus frequencies is plotted in Figure 4.12 (b), and one can clearly see that the component is very efficient within the passband.

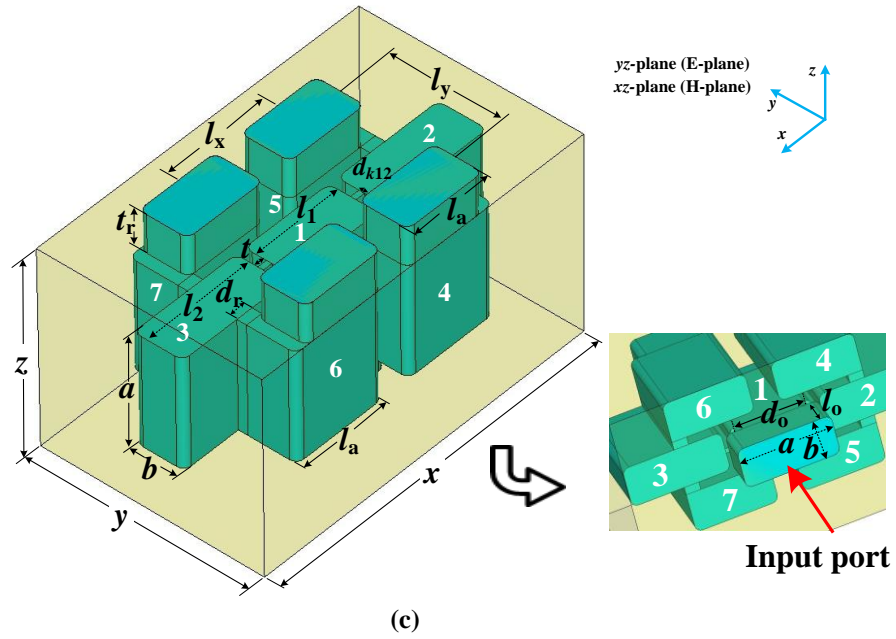
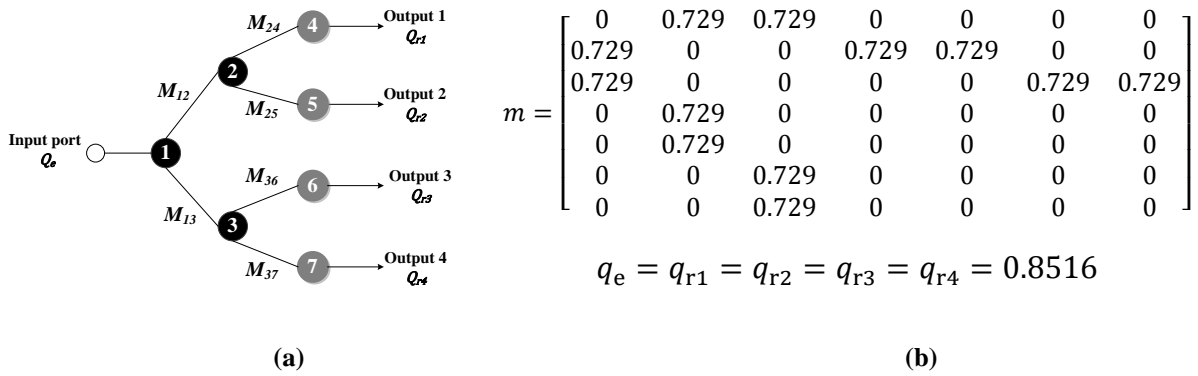


Figure 4.11: (a) Topology, (b) scaled coupling matrix, and (c) physical realisation of the 3rd order 2×2 antenna array-filter component. The dimensions in mm are: $a = 22.86$, $b = 10.16$, $l_0 = 8$, $l_1 = 19.76$, $l_2 = 23.90$, $l_r = 20.10$, $l_a = 17.65$, $t = 2$, $t_r = 10$, $d_0 = 17.70$, $d_{k12} = 1.14$, $d_r = 3.55$, $x = 79.56$, $y = 58.48$, $z = 42.86$, radius of the round corners = 1.6.

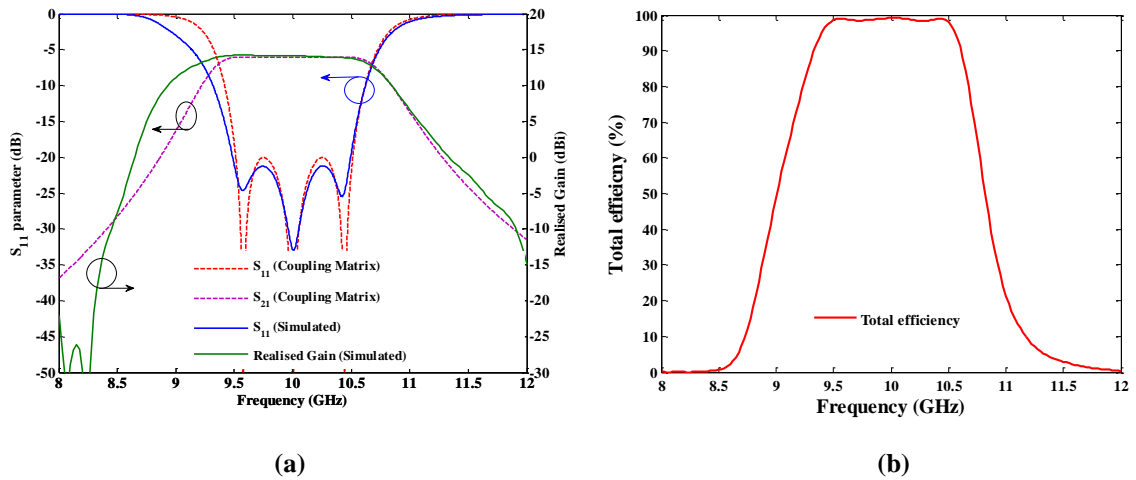


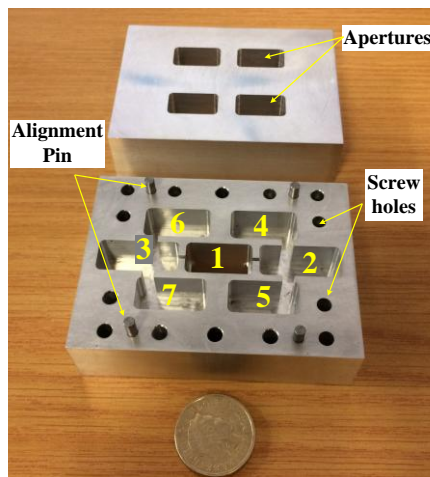
Figure 4.12: (a) Simulated response of the 3rd order 2×2 antenna array-filter component compared with the calculated response, (b) Simulated total efficiency.

4.3.2 Fabrication and measurement

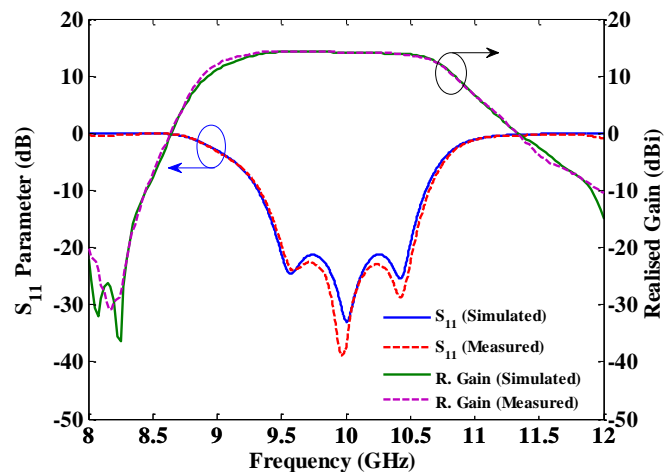
This section discusses the fabrication and measurement performed for the 3rd order 2×2 antenna array-filter component. The photograph of the fabricated component is shown in Figure 4.13 (a). It is built from two pieces of aluminium which are assembled using metal screws.

The measured realised gain and return loss is shown in Figure 4.13 (b), and they are in good agreement with each other. The realised gain fluctuates from 13.79 to 14.23 dBi over the passband, and the 3-dB gain bandwidth is 17.7%.

The measured E- and H-planes radiation patterns are compared with their simulated and shown in Figure 4.14 at three different frequencies within the passband frequency range. A very good agreement between them is depicted. The patterns in the H-plane have lower side lobe levels (below -13.5 dB) when they are compared to the E-plane patterns (-7 dB).



(a)



(b)

Figure 4.13: (a) Photograph, and (b) Simulated and calculated responses of the 3rd order 2 × 2 antenna array-filter component.

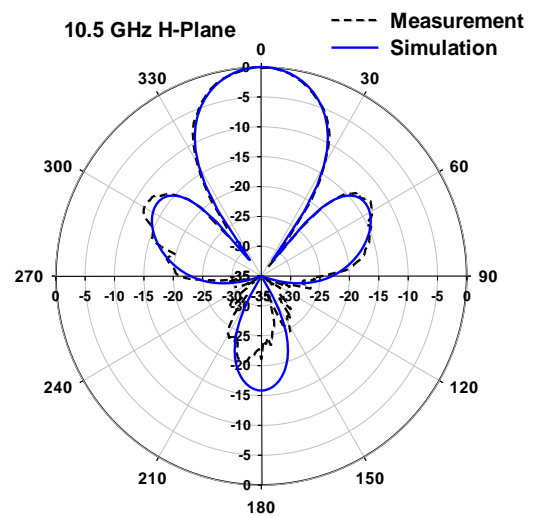
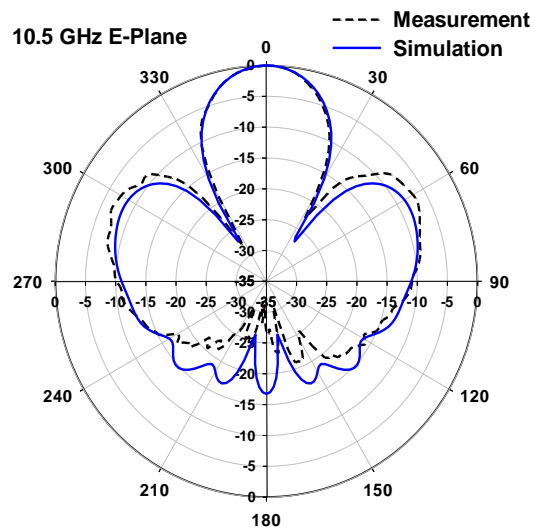
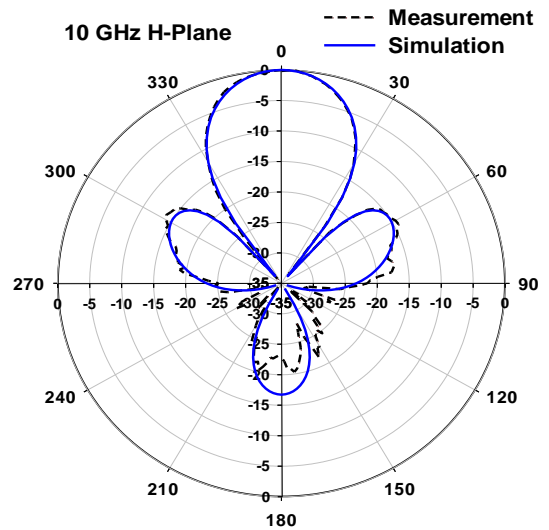
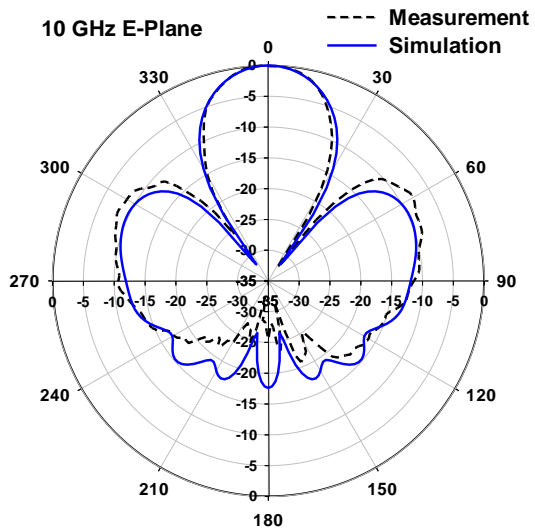
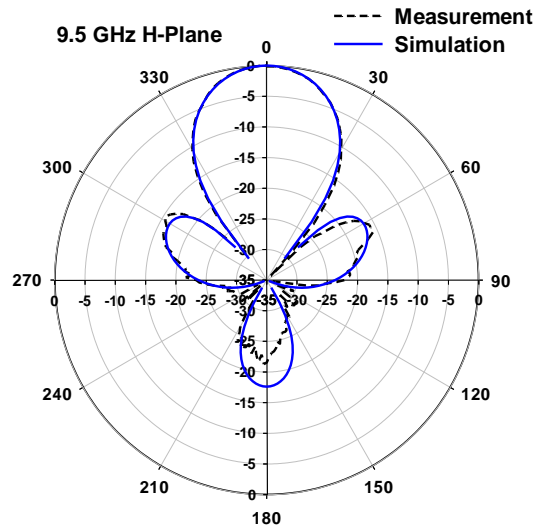
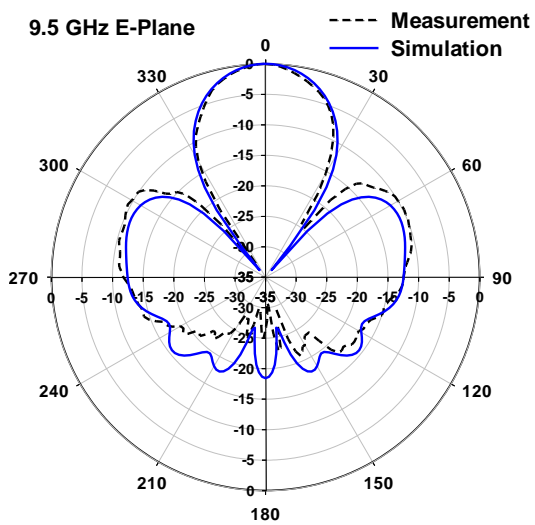


Figure 4.14: The simulated and measured radiation pattern of the 3rd order 2×2 antenna array-filter component for both the E- and H-planes at three different frequencies.

4.4 7th order 4×4 antenna array-filter component

In the previous section, design and fabrication of the 3rd order 2×2 *antenna array-filter* component have been analysed and discussed, and the peak gain obtained from the component was 14.23 dBi. In order to achieve higher gain, design of a larger-size array is still necessary.

There has been an increasing interest in using slotted waveguide antenna arrays in many high gain antenna applications due to ease in achieving high gains by making more slots in the walls of the waveguides. In addition to that, because the slotted waveguide arrays are mostly air-filled, they do not suffer from dielectric losses. Conventionally, series-fed networks were employed to design planar array slotted waveguide antenna [7-13]. Such feeding networks offer some unique features for the design such as using only a single waveguide-layer to form the whole antenna array, and hence simplifying the fabrication process. However, its main disadvantage is the reduction of the bandwidth of the arrays due to the “long-line” effect [14-16]. The effect becomes more obvious when the size of the array becomes larger. Therefore, to overcome this issue, a new technique to design a large array slotted waveguide antenna was proposed in [17, 18]. The technique was based on the double-layer waveguide structure. The lower layer was allocated to build the feeding network for the array, and the top layer was to form the arrays. Based on that technique, some interesting designs of slotted waveguide antenna arrays, notably 4×4, 8×8, and 16×16 arrays, are presented in [19], [16], [15, 20], respectively.

In this section, we use the coupling matrix approach to design a novel planar array waveguide aperture antenna. It is named the 7th order 4×4 *antenna array-filter* component. It consists of two waveguide-layers, proposing to construct from three pieces. The lower waveguide-layer

is to build the feeding network using coupled-resonators, whilst the top layer is to form the 4×4 array. On the other hand, another configuration for design of the 4×4 antenna array-filter component based on the coupled resonators, which is possible to be built of two pieces and using only a single waveguide-layer, has come to our attention. This will be presented in Chapter 5.

It is interesting to compare the electrical and physical specifications of the two 4×4 antenna array-filter components which are just mentioned above, and the 4×4 antenna array presented in [19]. This will also be handled to Chapter 5. In the following sub-sections, design, simulation and fabrication of the 7th order 4×4 antenna array-filter component will be discussed.

4.4.1 Design and simulation

Figure 4.15 shows the topology proposed for the 7th order 4×4 antenna array-filter component. It consists of thirty nine resonators that are coupled to each other via irises. It can be noticed from the topology that there are seven resonators that contribute to each radiating path, and with employing four power splitters to split the input power into sixteen outputs equally. Each resonator in the topology is coupled into no more than three resonators in order to simplify the physical implementation. The electrical specification is chosen to have 10% *FBW* and a return loss S_{11} of -20 dB over the passband (9.5-10.5 GHz) within the centre frequency 10 GHz.

The equivalent coupling matrix for the topology has been obtained by using the gradient-based optimisation technique [2]. All the optimised normalised non-zero entries of the coupling matrix are: $m_{1,2} = m_{1,3} = 0.588$, $m_{2,4} = m_{2,5} = m_{3,6} = m_{3,7} = 0.424$, $m_{4,8} = m_{5,9} = m_{6,10} =$

$m_{7,11} = 0.564$, $m_{8,12} = m_{9,13} = m_{10,14} = m_{11,15} = 0.564$, $m_{12,16} = m_{12,17} = m_{13,18} = m_{13,19} = m_{14,20} =$
 $m_{14,21} = m_{15,22} = m_{15,23} = 0.420$, $m_{16,24} = m_{16,25} = m_{17,26} = m_{17,27} = m_{18,28} = m_{18,29} = m_{19,30} =$
 $m_{19,31} = m_{20,32} = m_{20,33} = m_{21,34} = m_{21,35} = m_{22,36} = m_{22,37} = m_{23,38} = m_{23,39} = 0.588$. The scaled
 external and radiation quality factors are $q_e = q_{r1} = q_{r2} = \dots = q_{r15} = q_{r16} = 1.0080$.

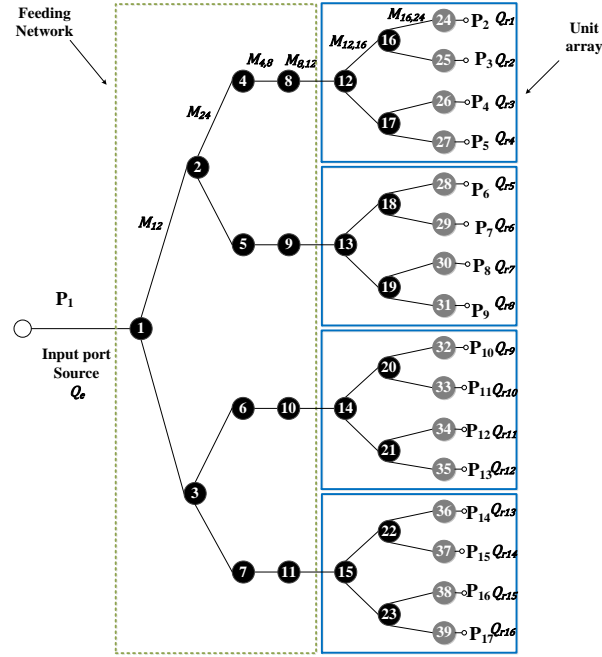


Figure4.15: Proposed topology for the 7th order 4x4 antenna array-filter component.

The topology of the component has been incorporated into a physical structure using rectangular waveguide cavity resonators whilst operating at the dominant mode TE₁₀₁ as shown in Figure 4.16. Although it is planned to build the component from three pieces (see Figure 4.16 (a)), it is shown in Figure 4.16 (b) with four pieces in order to label all the physical dimensions. It can be realised that all the resonators are coupled to each other by placing capacitive irises between them, except between resonators 8-12, 9-13, 10-14, and 11-15. Here, inductive irises were utilised in order to maintain vertical coupling and form the planar array configuration. All the dimensions of the component are given in the caption of the Figure 4.16.

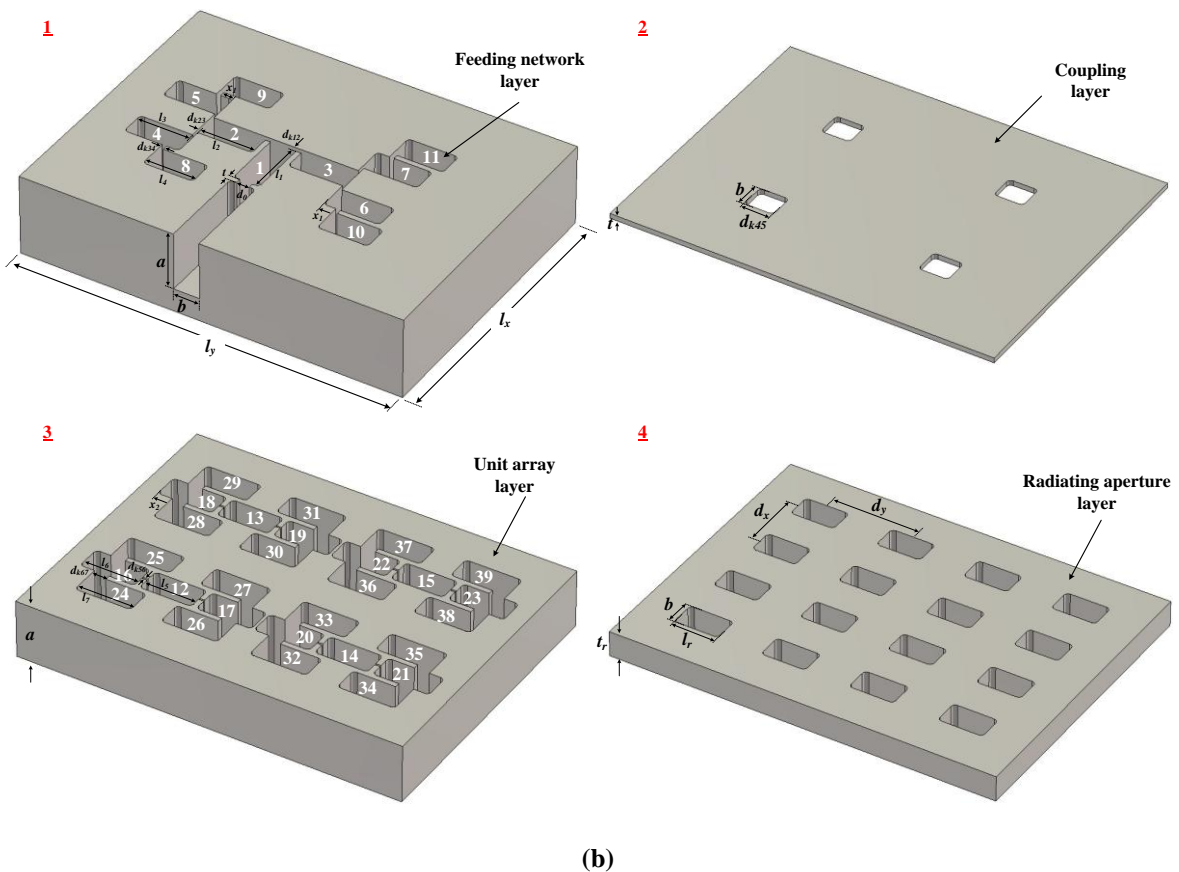
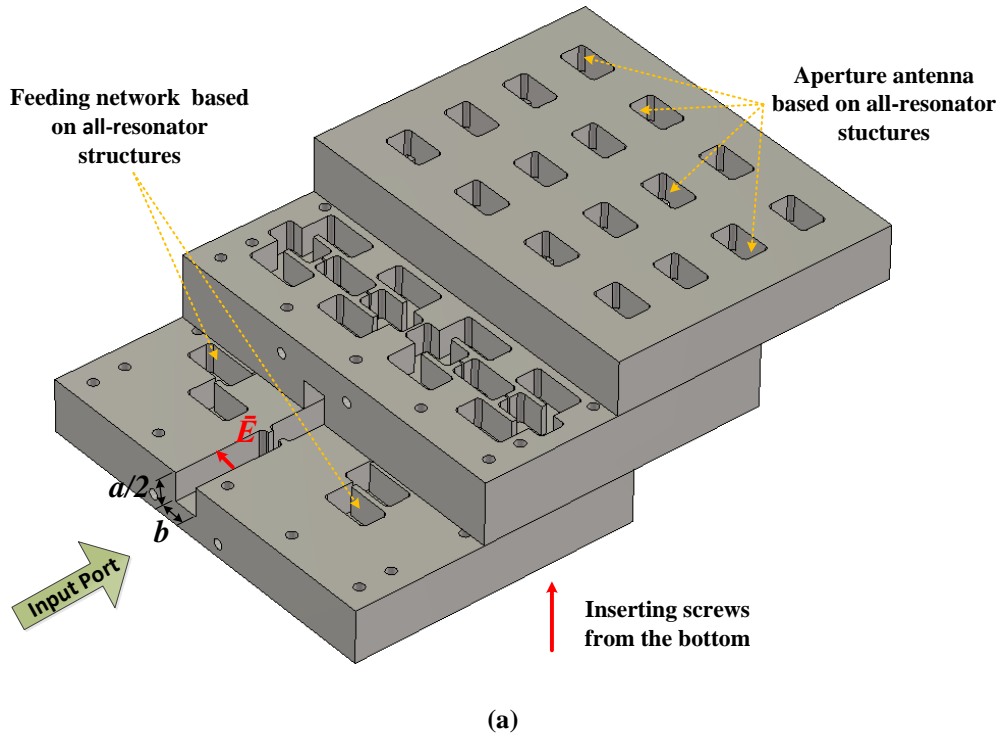


Figure 4.16: Layout view of the 7th order 4×4 antenna array-filter component modelled in the CST. The physical dimensions in mm are: $d_0 = 4.9779$, $d_{k12} = 1.7156$, $d_{k23} = 0.9132$, $d_{k34} = 1.6859$, $d_{k45} = 11.5715$, $d_{k56} = 0.6909$, $d_{k67} = 5.7733$, $l_1 = 25.3234$, $l_2 = 22.4451$, $l_3 = 21.7848$, $l_4 = 19.7931$, $l_5 = 20.4377$, $l_6 = 21.5814$, $l_7 = 22.0414$, $l_a = 17.2726$, $x_1 = 6.5500$, $x_2 = 15.7800$, $t = 2.0$, $t_r = 10$, $d_x = 24.32$, $d_y = 34.31$, $l_x = 113.5$, $l_y = 150.4$, radius of the round corners = 1.6.

The simulated frequency response of the component is obtained using the CST simulator [1], and compared in Figure 4.17 with the desired response obtained from the coupling matrix. Because the electrical size of the component is large, the time required to obtain the simulated frequency response is long, and this is impractical. To remedy this, the symmetry plane, which is a feature in the CST simulator [1], is used to reduce the time required for the computation by the factor of two. The simulated return loss is obtained, which is below -15 dB over the passband, and is in good agreement with the calculated. The realised gain is extremely stable over the passband, and has strong attenuation at out of the passband. The simulated total efficiency is shown in Figure 4.18 when using aluminium alloy to model the component, and it is apparent that this component is extremely efficient.

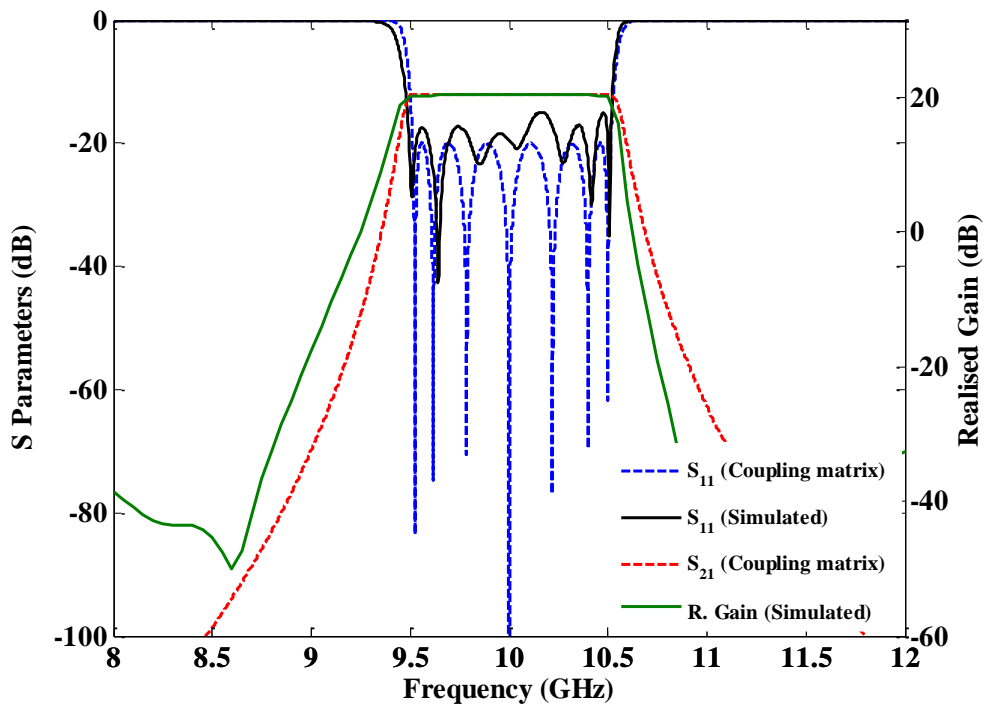


Figure 4.17: Simulated frequency responses compared with the calculated of the 7th order 4×4 antenna array-filter component.

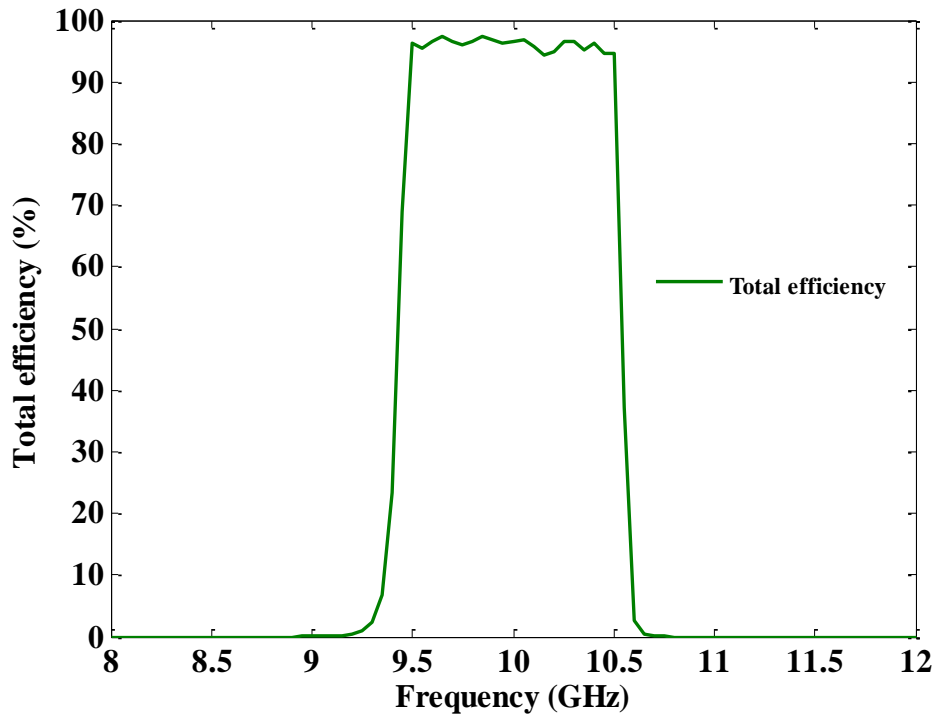


Figure 4.18: Simulated total efficiency of the 7th order 4×4 *antenna array-filter* component.

4.4.2 Fabrication and measurement

The 7th order 4×4 *antenna array-filter* component is fabricated from aluminium alloy using the CNC milling machine, and is shown in Figure 4.19. In order to facilitate the fabrication process, the component is made out of three pieces, splitting along the E-plane of the waveguide cavities. This minimises the effect of the additional loss occurring due to the imperfect joints in the pieces. Metal screws are used to assemble the pieces, and are inserted from the bottom in order to reduce the effect of the head of the screws on the radiation performance.

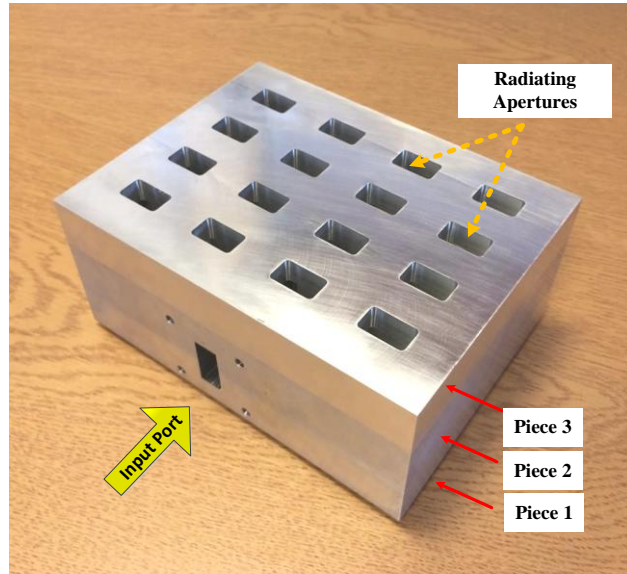
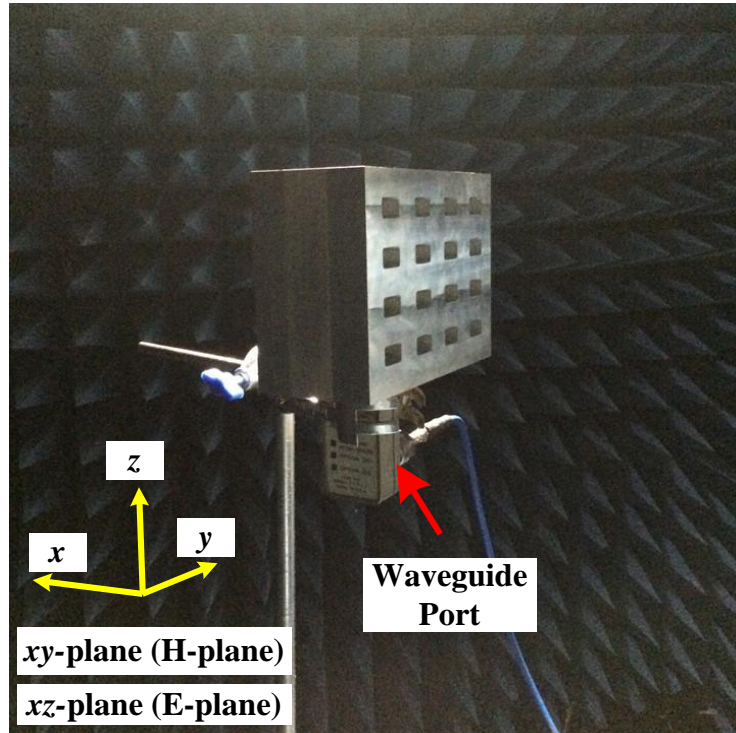


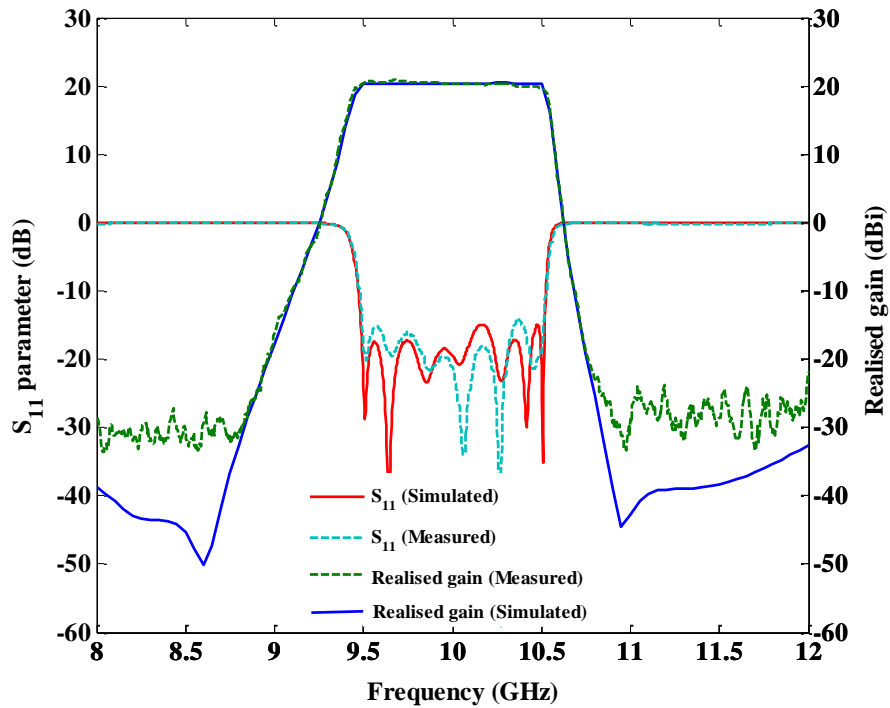
Figure 4.19: Photograph of the fabricated 7th order 4×4 antenna array-filter component.

In Figures 4.20 and 4.21, the measured frequency responses are compared with the simulated. It can be seen in Figure 4.20 (b) that the fractional impedance bandwidth, both in simulation and measurement, is more than 10% when $S_{11} = -15$ dB. The realised gain only fluctuates between 20.24 and 20.43 dBi over the entire passband, and the 3-dB gain bandwidth is 11%.

The radiation pattern for both the E- and H-planes are measured, and they are compared with the simulation in Figure 4.21. The measured patterns are in good agreement with the simulation. The side lobe level is lower than -12 dB at all the three given frequency points in the E-plane. However, in the H-plane, because the spacing between the radiating apertures is large ($1.14 \lambda_0$), two grating lobes can be identified. Reducing the spacing between the radiating outputs in the H-plane for the given component is not possible due to the electrically large dimensions of the waveguide resonators. However, it is possible to suppress the side lobe levels when constructing the component based on unequal power splitter. This is a new task, and it will be handled for future work [6]. Adding one more layer is also possible to suppress the grating and side lobe levels. However, this is not considered in this work.



(a)



(b)

Figure 4.20: (a) The 7th order 4×4 antenna array-filter component under test, (b) Measured frequency responses compared with the simulated.

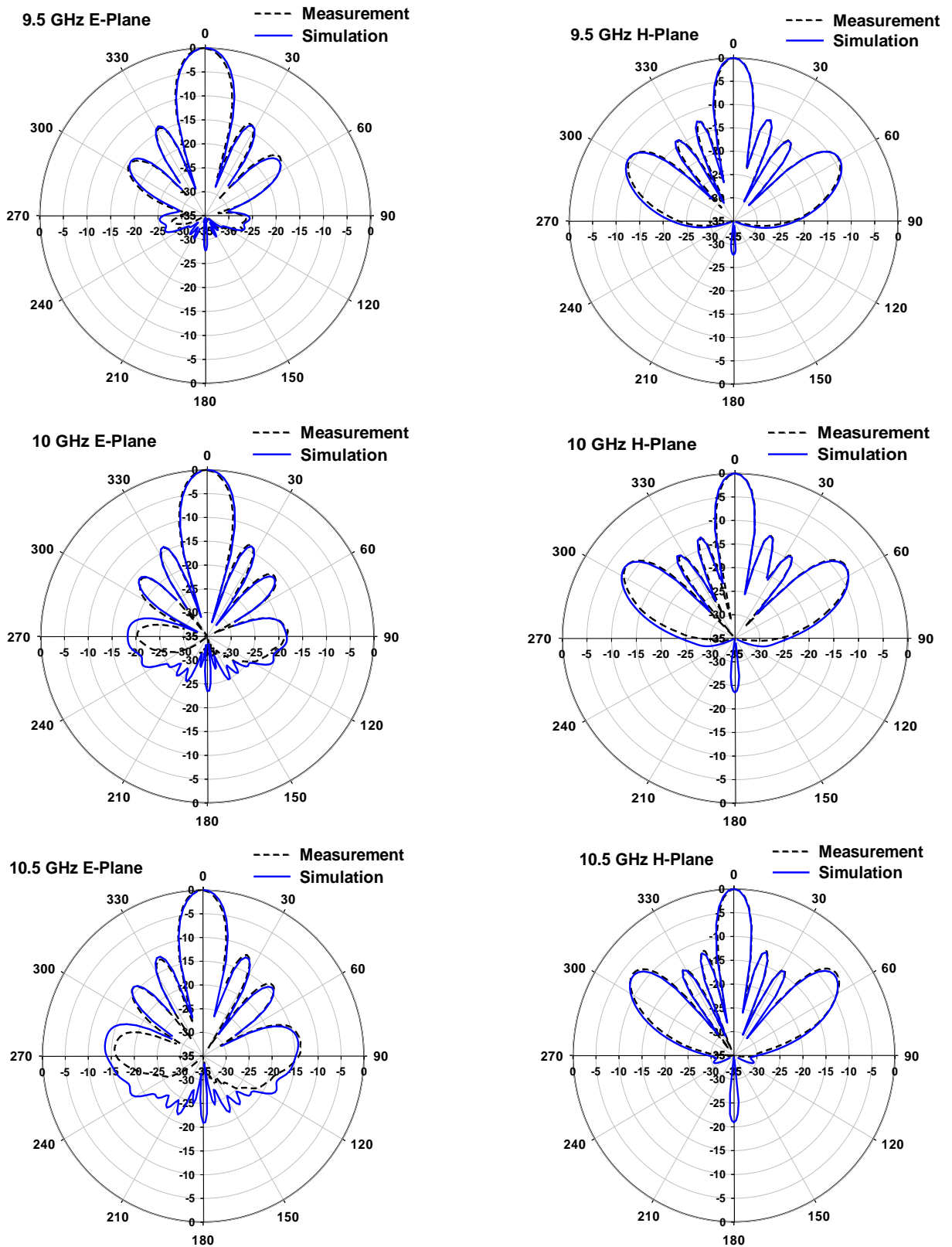


Figure 4.21: Measured radiation pattern of the 7th order 4×4 antenna array-filter component compared with the simulated at three different frequencies for both the E- and H-planes.

4.5 Conclusions

In this chapter, the topology, design and fabrication of four *antenna-filter* and *antenna array-filter* components have been presented and discussed. All the presented components, which were based on the design technique given in Chapter 3, were constructed using rectangular waveguide cavity resonators. The CNC milling machine was used to fabricate the components. Aluminium Alloy was used to build the components due to the fact that it was suitable for the milling and relatively cheap. The topologies were also selected keeping the physicality of realised components in mind. The measurements for the return loss, realised gain, and the radiation pattern of the components were conducted. The measured results were in very good agreement with the simulations, and validated the new design technique.

4.6 References

1. Studio, C.M., *Computer simulation technology*. GmbH, Darmstadt, Germany, 2009.
2. Skaik, T., M.J. Lancaster, and F. Huang, *Synthesis of multiple output coupled resonator circuits using coupling matrix optimisation*. IET microwaves, antennas & propagation, 2011. 5(9): p. 1081-1088.
3. Cogollos, S., et al. *Novel rectangular waveguide structures for advanced filter characteristics*. in *Microwave Symposium (IMS), 2014 IEEE MTT-S International*. 2014. IEEE.
4. Soto, P., et al., *Practical Design of Rectangular Waveguide Filters with a Capacitive Building Block providing an Extra Transmission Zero*.
5. Carceller, C., et al., *Design of Compact Wideband Manifold-Coupled Multiplexers*. 2015.
6. Lancaster, M.J., *Private communication*. 2015.
7. Goto, N., *A planar waveguide slot antenna of single layer structure*. IEICE Technical Choke, 1988.
8. Shirouzu, T., et al. *Wireless IP Access System for low cost FWA services*. in *6th European Conference on Wireless technology*. 2003.
9. Ando, M., et al., *Novel single-layer waveguides for high-efficiency millimeter-wave arrays*. *Microwave Theory and Techniques, IEEE Transactions on*, 1998. 46(6): p. 792-799.

10. Kimura, Y., et al., *A low-cost and very compact wireless terminal integrated on the back of a waveguide planar array for 26 GHz band fixed wireless access (FWA) systems*. Antennas and Propagation, IEEE Transactions on, 2005. **53**(8): p. 2456-2463.
11. Hirokawa, J., M. Zhang, and M. Ando. *94GHz single-layer slotted waveguide array by diffusion bonding of laminated thin plates*. in *Proc. Int. Symp. Antenna Propag. TP-C0.-3*. 2008.
12. Hirokawa, J., et al., *A single-layer slotted leaky waveguide array antenna for mobile reception of direct broadcast from satellite*. Vehicular Technology, IEEE Transactions on, 1995. **44**(4): p. 749-755.
13. Ando, M., *Planar waveguide arrays for millimeter wave systems*. IEICE transactions on communications, 2010. **93**(10): p. 2504-2513.
14. Zhang, M., J. Hirokawa, and M. Ando, *An E-band partially corporate feed uniform slot array with laminated quasi double-layer waveguide and virtual PMC terminations*. Antennas and Propagation, IEEE Transactions on, 2011. **59**(5): p. 1521-1527.
15. Hirokawa, J., *Plate-laminated Waveguide Slot Array Antennas and its Polarization Conversion Layers*. Automatika–Journal for Control, Measurement, Electronics, Computing and Communications, 2012. **53**(1).
16. Guan-Long, H., et al., *Broadband and high gain waveguide-fed slot antenna array in the Ku-band*. Microwaves, Antennas & Propagation, IET, 2014. **8**(13): p. 1041-1046.
17. Oh, S.-S., et al., *Two-layer slotted-waveguide antenna array with broad reflection/gain bandwidth at millimetre-wave frequencies*. IEE Proceedings-Microwaves, Antennas and Propagation, 2004. **151**(5): p. 393-398.
18. Johnson, R.C. and H. Jasik, *Antenna engineering handbook*. New York, McGraw-Hill Book Company, 1984, 1356 p. No individual items are abstracted in this volume., 1984. **1**.
19. Kim, D., et al., *4-Element Corporate-Feed Waveguide Slot Array Antenna With Cavities for the 120 GHz-Band*. Antennas and Propagation, IEEE Transactions on, 2013. **61**(12): p. 5968-5975.
20. Huang, G.-L., et al., *A Low Profile and Low Sidelobe Wideband Slot Antenna Array Fed by an Amplitude-Tapering Waveguide Feed-Network*. Antennas and Propagation, IEEE Transactions on, 2015. **63**(1): p. 419-423.

Chapter 5

Single waveguide-layer planar array antenna design

In this Chapter, the topology, design, and fabrication for two *antenna array-filter* components are presented, and measurements to validate their performance are conducted. The first component is a 3rd order 2×2 *antenna array-filter*. It is arranged to form a planar unit array using a single waveguide-layer and feeding from a side of the plane containing the component. The electrical and physical specifications of this component are compared with (i) the component given in Chapter 4 (Section 4.3) and (ii) a 2×2 waveguide-fed cavity backed unit array presented in the literature. The second component, the 4th order 4×4 *antenna array-filter*, is also introduced. It has a configuration which allows us to use only a single waveguide-layer to construct the whole component. For the purposes of comparison, specifications of this component are compared with (i) the component given in Chapter 4 (Section 4.4), and (ii) the 4×4 slot array given in the literature.

5.1 3rd order 2×2 *antenna array-filter* component

This section demonstrates the design and fabrication of the 3rd order 2×2 *antenna array-filter* component.

5.1.1 Design and simulation

Figure 5.1 shows the topology and normalised coupling matrix of the 3rd order 2×2 *antenna*

array-filter component. As can be noticed from the topology, only two resonators are utilised to build the feeding network, whilst the four remaining resonators act as the *resonator-radiators*. The gradient-based optimisation technique [1] is used to obtain the equivalent coupling matrix (see Figure 5.1 (b)). The specifications of the component are to have 10% *FBW* at the centre frequency 10 GHz and with the return loss over the band of interest -20 dB. The 3-D layout of the component is illustrated in Figure 5.2. The b_1 dimension for resonators 1 and 2 are chosen to be 7 mm so as to reduce the spacing between the radiating outputs in the yz -plane and minimise the side lobe levels. It should be pointed out that the input port is located in the plane containing the component. This allows constructing the component using only a single-waveguide layer. In addition to this, a Star-Junction is also employed to reduce the total number of resonators required to build the component.

Although the coupling value between the resonators 2 and 3 (M_{23}) is the same as between the resonators 2 and 5 (M_{25}) in the matrix (see Figure 5.1 (b)), their equivalent aperture widths (d_{k23} and d_{k25}) are not the same (see Figure 5.2). This is due to the fact that the positions where the couplings take place between resonators 2-3 and resonators 2-5 are not symmetrical. The simulation results are obtained using the CST simulator [2], and they are compared in Figure 5.3 with the desired responses. It can be noticed that the attenuation of the realised gain around the start band is poorer than expected. This is mainly because of the unexpected radiation of the component at frequency 8.6 GHz. It is believed that occurrence of the radiation could be due to the propagation of an additional mode in resonator 2. Also, capacitive irises usually provide poorer attenuation at the start band frequency [3]. The simulated total efficiency is shown in Figure 5.3 (b), and it is more than 95% over the passband.

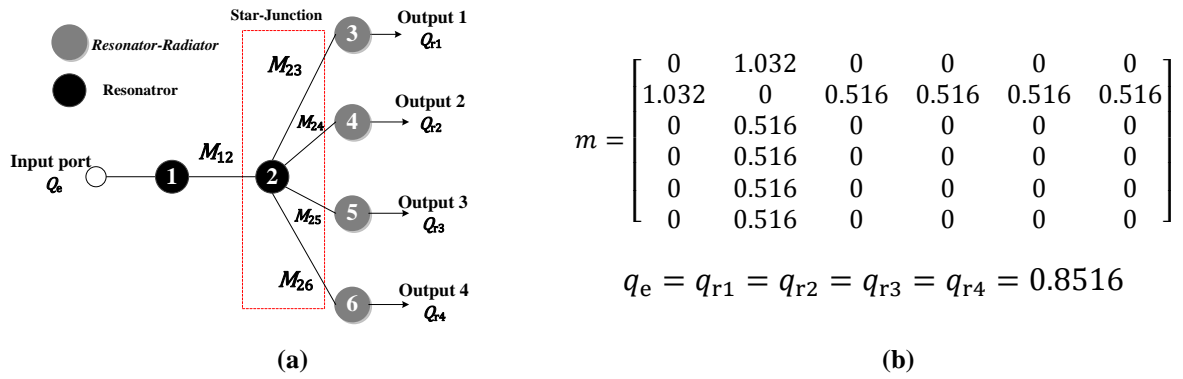


Figure 5.1: (a) Topology, and (b) equivalent coupling matrix of the 3rd order 2×2 antenna array-filter component.

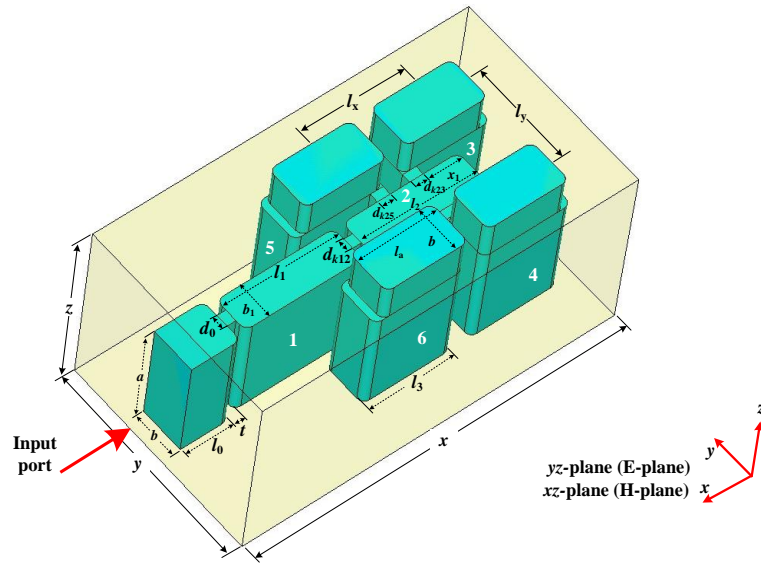


Figure 5.2: Physical structure of the 3rd order 2×2 antenna array-filter component. The dimensions in mm are: $a = 22.86$, $b = 10.16$, $b_1 = 7.0$, $l_0 = 11$, $l_1 = 26.55$, $l_2 = 26.47$, $l_3 = 20.21$, $l_a = 18.60$, $t = 2$, $t_r = 10$, $d_0 = 4.80$, $dk_{12} = 1.45$, $dk_{23} = 3.12$, $dk_{25} = 2.95$, $x_1 = 8.138$, $x = 82.12$, $y = 43.32$, $z = 42.86$, $l_x = 23.04$, $l_y = 21.16$, radius of round corners = 1.6.

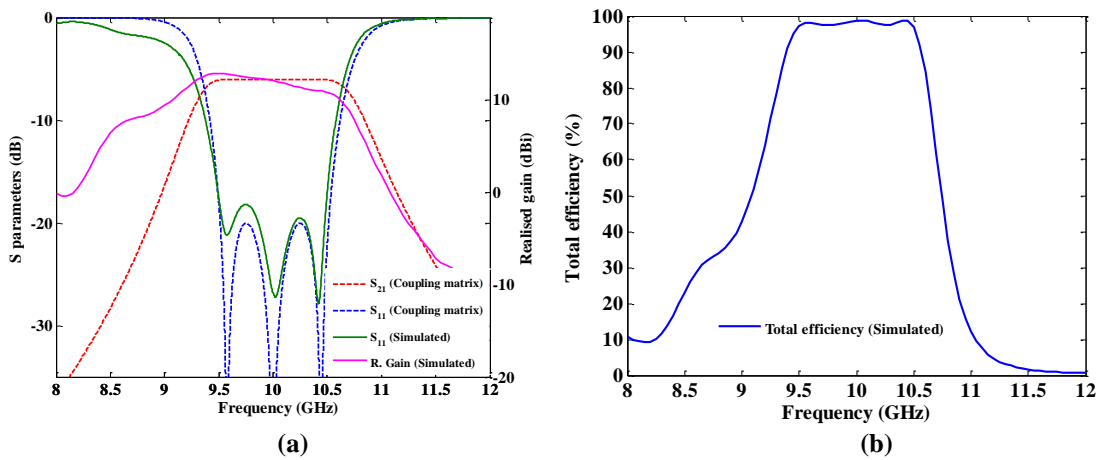


Figure 5.3: (a) Frequency responses of the 3rd order 2×2 antenna array-filter component compared with the desired responses calculated from the coupling matrix (b) simulated total efficiency.

5.1.2 Fabrication and measurement

The component is fabricated from aluminium alloy 6082 using the CNC milling machine. It is split along the E-plane into two pieces in order to facilitate the fabrication process (See Figure 5.4). Alignment pins are used to avoid the misalignment between the two pieces and metal screws are used to assemble them.

The measured return loss is compared with the simulated return loss in Figure 5.5 (a), and they are in good agreement. The measured S_{11} has a better matching level over the passband when compared with the simulated. However, its bandwidth is slightly narrower than. These differences could be due to errors in manufacture. The simulated and measured realised gain is plotted in Figure 5.5 (b). The 3-dB gain bandwidth of the component is about 15.7% at the centre frequency 10 GHz, having a peak gain (12.94 dBi) at frequency 9.55 GHz.

The simulated and measured radiation patterns for both the E- and H-planes for three frequency points within the passband are shown in Figure 5.6. They are in very close agreement with each other. The side lobe levels in the E-plane patterns are -10 dB, whilst they are -16.5 dB in the H-plane. It can be noticed that the main beam of the radiation pattern in the H-plane at frequency 9.5 GHz is shifted 3° to the right hand side. It is found that, after employing four E- and H-field probes at the centre of each radiating output of the component in CST, a small phase variation in the H-plane at 9.5 GHz has been identified.

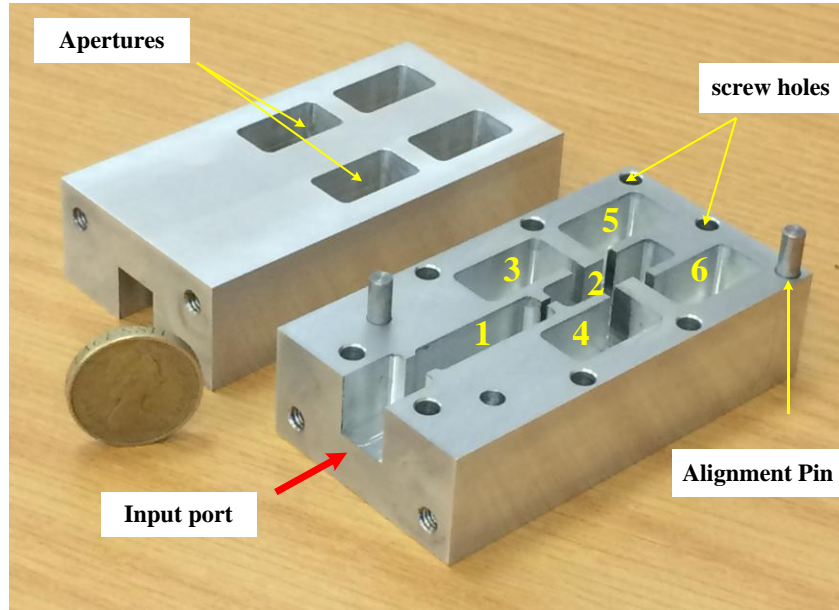


Figure 5.4: Photograph of the fabricated 3rd order 2×2 antenna array-filter component.

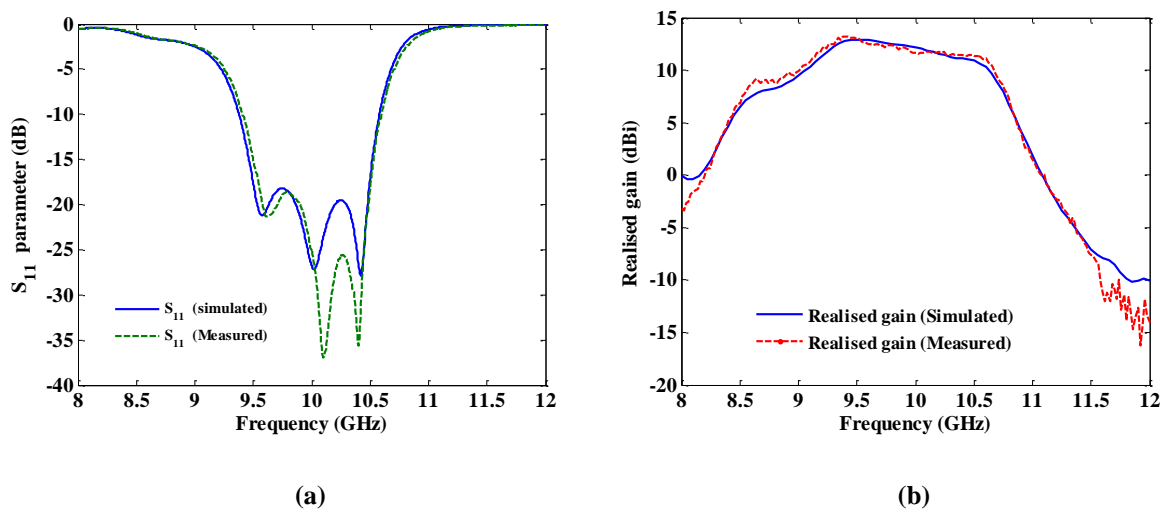


Figure 5.5: Measured frequency responses of the 3rd order 2×2 antenna array-filter component compared with the simulated.

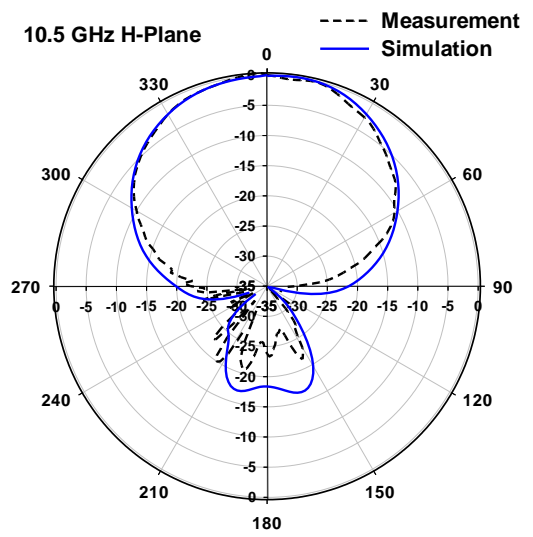
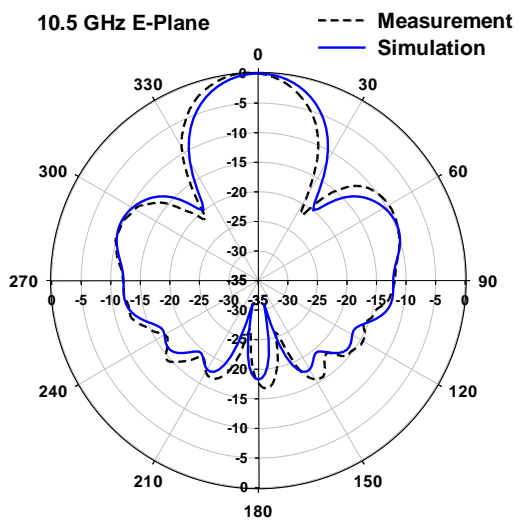
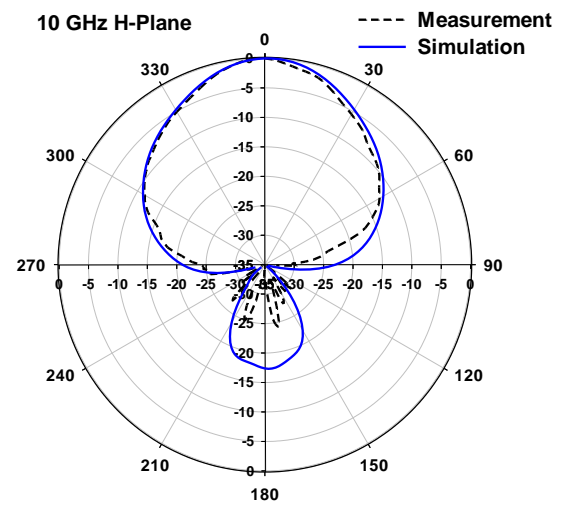
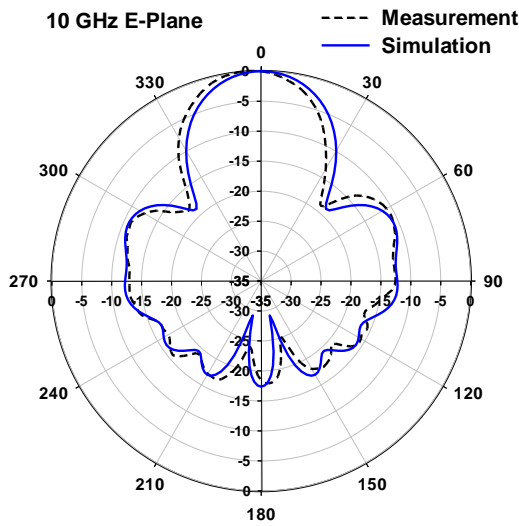
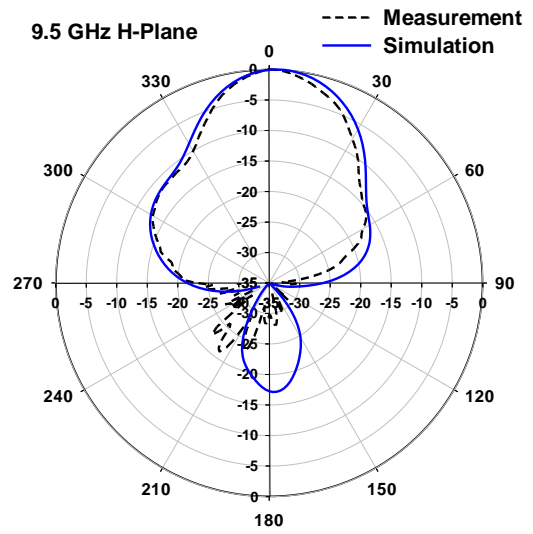
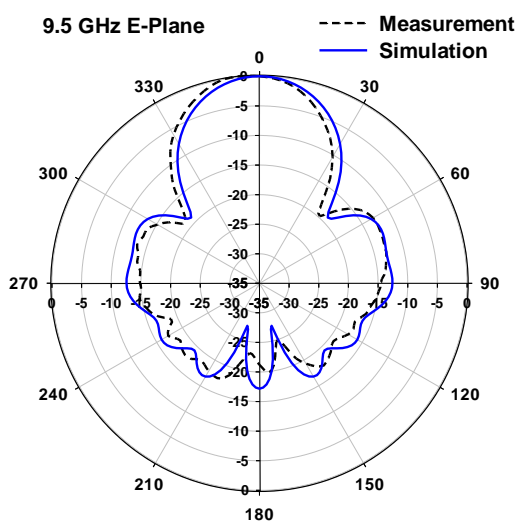


Figure 5.6: The simulated and measured radiation pattern of the 3rd order 2×2 antenna array-filter component for both the E- and H-planes at three different frequencies.

5.2 Comparison

A comparison of some important parameters of the 2×2 *antenna array-filter* components presented in the previous section and Chapter 5 (Section 5.1), against the 2×2 waveguide-fed cavity backed unit array given in [4] is demonstrated in this section. The category of the comparison is based on the electrical and physical specifications of the mentioned components. Due to the inconsistency of the physical structures of the components, an absolute comparison for their physical specifications is not straightforward. Therefore, only several physical features, which are common among the components, are summarised in Table 5.1.

The electrical specifications shown in Table 5.1 are based on the simulated performances. The design of the 2×2 waveguide-fed cavity backed unit array has been demonstrated in many publications [4-7]. However, the specifications given in [4] for the 2×2 waveguide-fed cavity backed unit array is shown in Table 5.1 for the purpose of the comparison due to the fact that they are mentioned in detail.

The 2×2 *antenna array-filter* component with 7 resonators given in chapter 4 has a better performance in terms of antenna bandwidth and filtering functionality in comparison to the other two given components. Also, the gains of the three components are comparable to each other. In terms of the component size, the 2×2 *antenna array-filter* component with 6 occupies less space than the others. On the other hand, the 2×2 *antenna array-filter* component with 7 resonators and the 2×2 waveguide-fed cavity backed unit array utilised two waveguide layers. This increases the volume of the components. However, the 2×2 *antenna array-filter* component with 6 resonators utilised only one-single waveguide layer which leads to reduce the total volume of the component.

Table 5.1: Comparison between some physical and electrical specifications of the components at their designed centre frequency.

| Components | | 3 rd order 2×2 antenna array-filter (Chapter 4, Section 4.3) | 3 rd order 2×2 antenna array-filter (Chapter 5, Section 5.1) | 2×2 waveguide-fed cavity backed unit array [4] |
|-------------------------|------------------------|--|---|---|
| Physical Specifications | Topology | <p>Resonator-Radiator (grey circle), Resonator (black circle). Input port Q_6 connects to Resonator 1. Resonator 1 is coupled to Resonators 2, 3, and 4. Resonator 2 is coupled to Resonators 5 and 6. Resonator 3 is coupled to Resonator 7. Resonators 4, 5, 6, and 7 are radiators connected to Output 1 (Q_1), Output 2 (Q_2), Output 3 (Q_3), and Output 4 (Q_4) respectively. Coupling matrices are labeled $M_{12}, M_{13}, M_{24}, M_{25}, M_{36}, M_{37}$.</p> | <p>Resonator-Radiator (grey circle), Resonator (black circle). Input port Q_6 connects to Resonator 1. Resonator 1 is coupled to a Star-Junction (Resonator 2). The Star-Junction is coupled to Resonators 3, 4, 5, and 6. Resonators 3, 4, 5, and 6 are radiators connected to Output 1 (Q_1), Output 2 (Q_2), Output 3 (Q_3), and Output 4 (Q_4) respectively. Coupling matrices are labeled $M_{12}, M_{23}, M_{24}, M_{25}, M_{26}$.</p> | NA |
| | Physical configuration | <p>3D view of 7 resonators in a rectangular cavity. Dimensions: l_x, l_y, l_z. Resonator positions: $d_{x12}, d_{x13}, d_{x24}, d_{x25}, d_{x36}, d_{x37}$. Coordinate system: yz-plane (E-plane), xz-plane (H-plane). Input port is shown at the bottom.</p> | <p>3D view of 6 resonators and a star-junction in a rectangular cavity. Dimensions: l_x, l_y, l_z. Resonator positions: $d_{x12}, d_{x23}, d_{x24}, d_{x25}, d_{x26}$. Coordinate system: yz-plane (E-plane), xz-plane (H-plane). Input port is shown at the bottom.</p> | <p>Top view diagrams showing: ① waveguide port, ② aperture, ③ cavity, ④ slot. Dimensions: $a, b, c, d, e, k, l, m, j, i$. Coordinate system: yz-plane (E-plane), xz-plane (H-plane).</p> |
| | No. of layers | 1 | 1 | 2 |
| | No. of resonators | 7 | 6 | NA |

| Components | | 3 rd order 2×2 <i>antenna array-filter</i> (Chapter 4, Section 4.3) | 3 rd order 2×2 <i>antenna array-filter</i> (Chapter 5, Section 5.1) | 2×2 waveguide-fed cavity backed unit array [4] | |
|----------------------------------|---|---|---|---|----------|
| Electrical Specifications | Bandwidth (%) ($S_{11} < -10$ dB) | 13.0 | 12.0 | 11.3 | |
| | Peak gain (dBi) | 14.26 | 13.21 | 15.30 | |
| | Side lobe level (dB) | E-plane | - 8.5 | - 10.8 | ≈ - 13.0 |
| | | H-plane | - 15 | - 17.3 | |
| | Realised gain attenuation (dB) | Start band (8 GHz) | - 36.33 | - 0.40 | NA |
| | | Stop band (12 GHz) | - 15.01 | - 10.14 | |

5.3 4th order 4×4 antenna array-filter component

The design of the 7th order 4×4 antenna array-filter component was demonstrated in Chapter 4. It was formed out of two waveguide-layers and using thirty nine coupled-resonators. In this section, a design of 4×4 antenna array named the 4th order 4×4 antenna array-filter component is introduced. It is arranged in a way that can be formed out of only a single waveguide-layer and twenty-five coupled-resonators. Its topology, design, and fabrication are given in the following sub-sections.

5.3.1 Design and simulation

Figure 5.7 shows the topology of the 4th order 4×4 antenna array-filter component. It consists of twenty-five resonators coupled to each other using capacitive irises. Four Star-Junctions are implemented in the topology in order to offer size reduction. Looking at the topology from the input port side (left hand side) to the output side (right hand side), four resonators contribute to build each of the radiating path. Two four-way power splitters are utilised in the topology so as to split the input signal into sixteen outputs equally, and keep all the outputs in phase (see Figure 5.8). The gradient-based optimisation technique [1] is used to generate an equivalent coupling matrix for the topology. The non-zero entries of the coupling matrix, and scaled external and radiation quality factors are $m_{1,2} = m_{1,3} = m_{1,4} = m_{1,5} = 0.456$, $m_{2,6} = m_{3,7} = m_{4,8} = m_{5,9} = 0.700$, $m_{6,10} = m_{6,11} = m_{6,12} = m_{6,13} = m_{7,14} = m_{7,15} = m_{7,16} = m_{7,17} = m_{8,18} = m_{8,19} = m_{8,20} = m_{8,21} = m_{9,22} = m_{9,23} = m_{9,24} = m_{9,25} = 0.456$, $q_e = q_{r1} = q_{r2} = \dots = q_{r15} = q_{r16} = 0.931$.

The topology is used to convert into an actual physical structure that is shown in Figure 5.8. It is proposed to construct this with two pieces using aluminium alloy. It should be mentioned

that the structure is electrically large, and, as a result, the computational time required by the CST simulator [2] to extract the simulated electrical parameters is long (≈ 5 minutes) when using a personal computer PC with a specification of (Processor: Intel(R) Core(TM) i5-3570 CPU @3.40 GHz, Installed memory (RAM): 8.00 GB). However, because the structure is symmetrical in both the E- and H-planes, the symmetrical boundary plane featured in the CST simulator can be used to reduce the total time required by a factor of four. The simulated frequency response is plotted in Figure 5.9. There is a very good agreement shown between the simulation and the desired response obtained from the coupling matrix. The simulated total efficiency of the component is plotted in Figure 5.10, and it is more than 95 % over the frequency band of interest. The dimensions obtained for the structure to generate the simulated result are given in the caption for Figure 5.8.

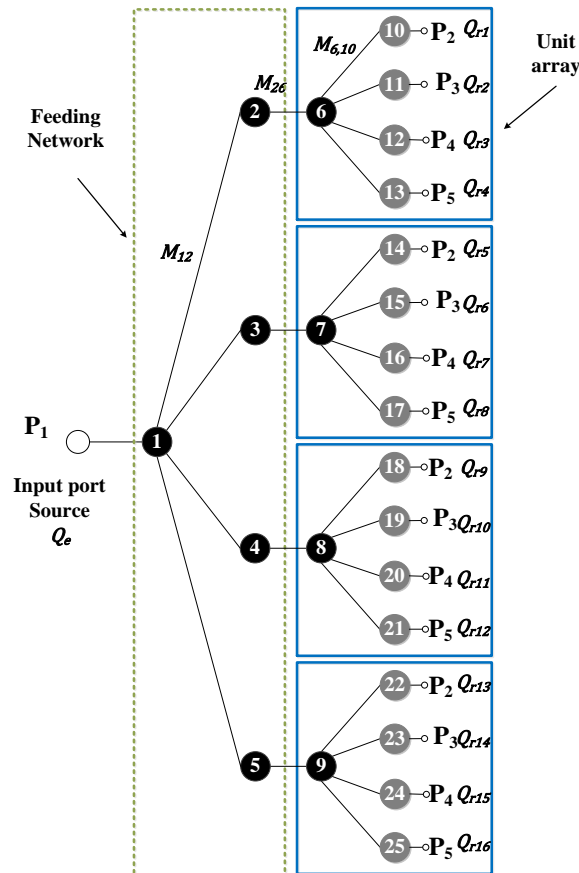


Figure 5.7: Proposed topology for the 4th order 4x4 antenna array-filter component.

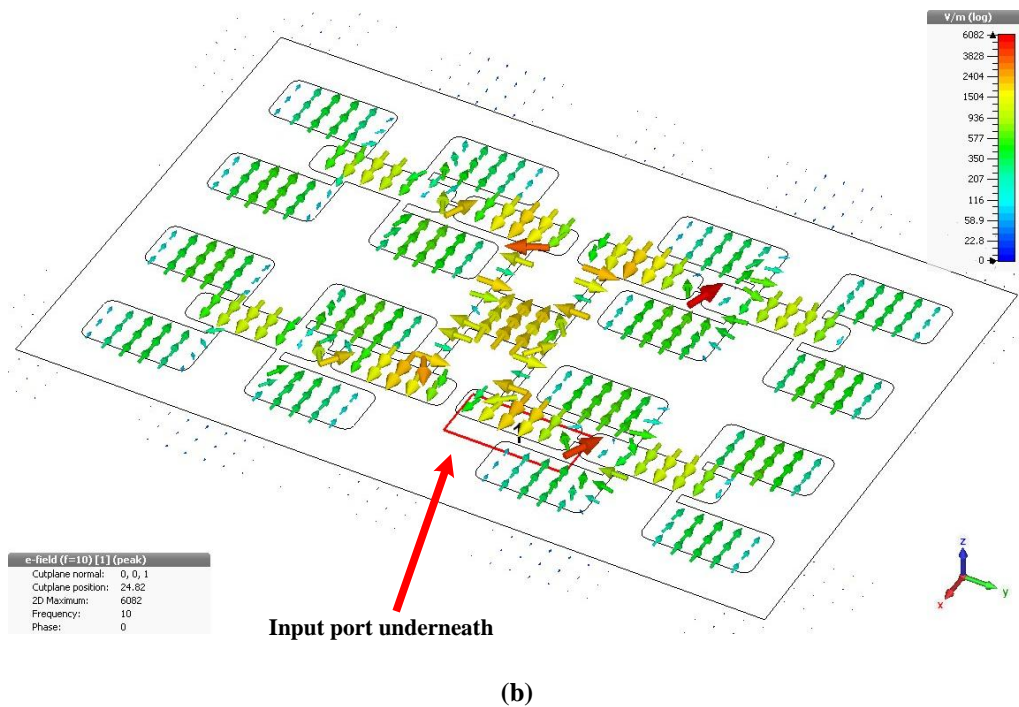
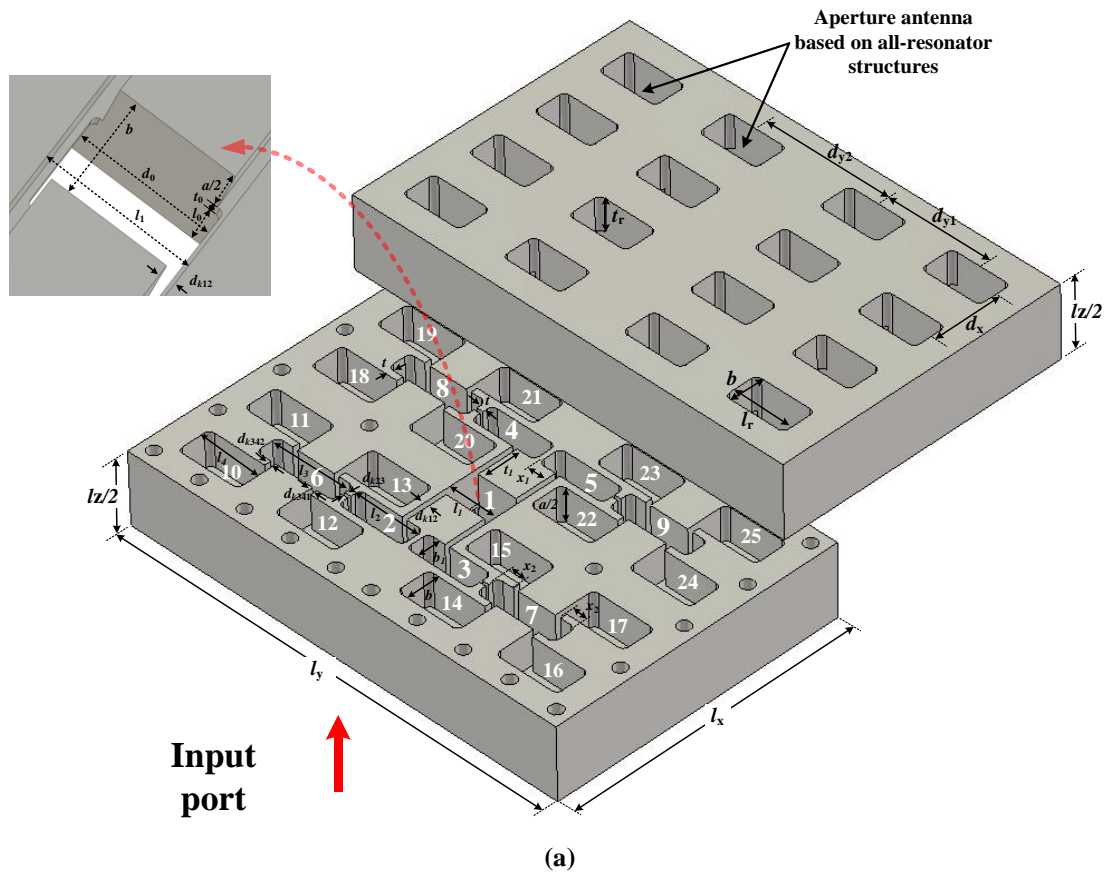


Figure 5.8: (a) Physical configuration of the 4th order 4×4 antenna array-filter component modelled in the CST. The physical dimensions in mm are: $d_0 = 15.68$, $d_{k12} = 1.48$, $d_{k23} = 0.82$, $d_{k341} = 1.52$, $d_{k342} = 1.64$, $l_1 = 15.70$, $l_2 = 21.20$, $l_3 = 25.62$, $l_4 = 20.38$, $l_a = 17.00$, $x_1 = 5.46$, $x_2 = 6.21$, $t = 2.0$, $t_0 = 1$, $t_r = 10$, $d_x = 21.46$, $d_{y1} = 32.22$, $d_{y2} = 41.98$, $l_x = 90$, $l_y = 140$, $l_z = 42.86$, radius of the round corners = 1.6. (b) The E-field distribution inside the component at 10 GHz with the aid of CST [2].

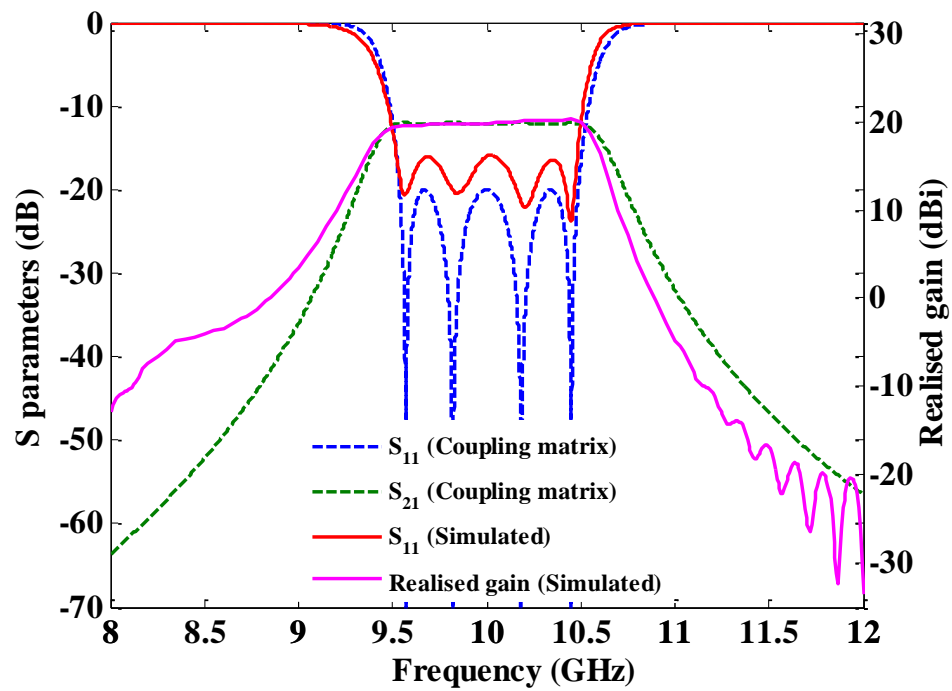


Figure 5.9: Frequency responses of the 4th order 4×4 antenna array-filter component compared with the desired responses calculated from the coupling matrix.

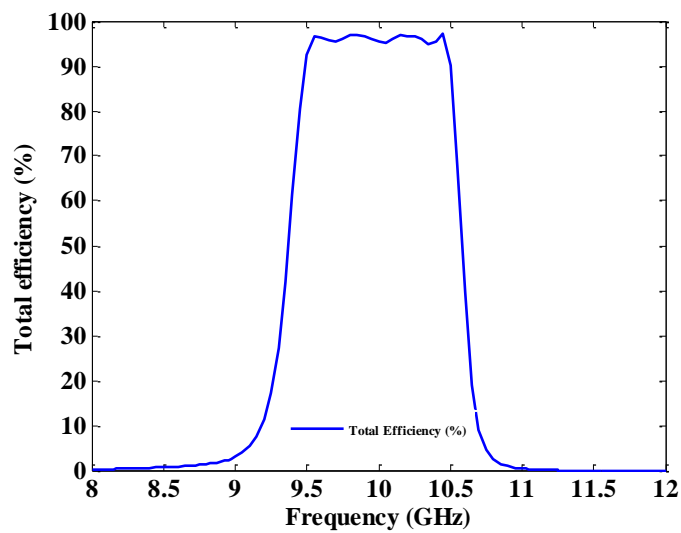


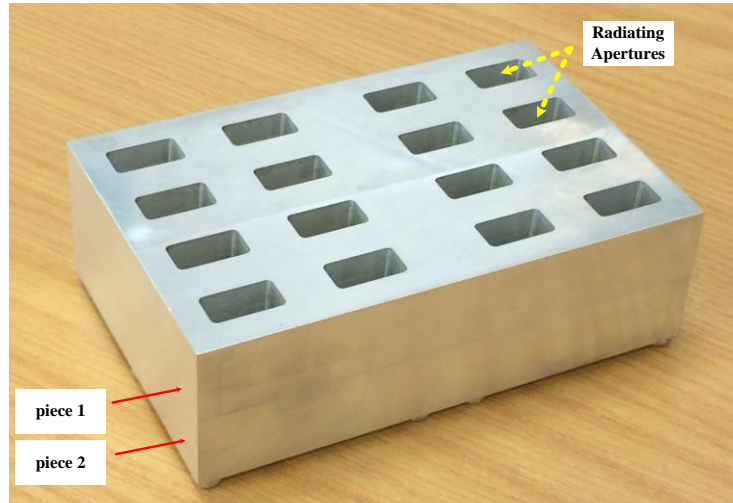
Figure 5.10: Simulated total efficiency response of the 4th order 4×4 antenna array-filter component.

5.3.2 Fabrication and measurement

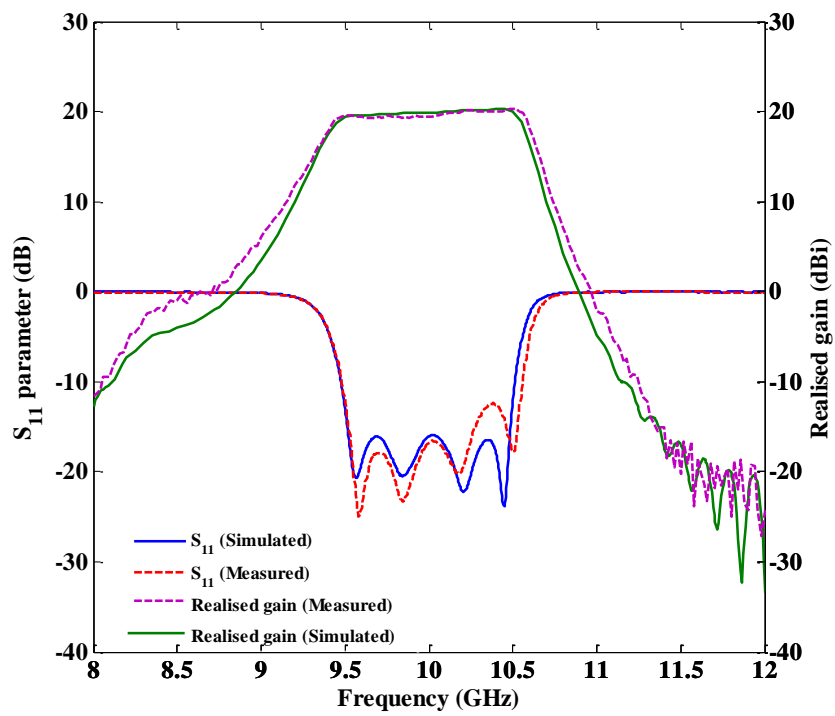
Figure 5.11 (a) shows the photograph of the fabricated 4th order 4×4 *antenna array-filter* component. It is made out of two pieces of aluminium alloy using the CNC milling machine.

The measured return loss and realised gain are shown in Figure 5.11 (b). They are in very good agreement with their simulations. The *FBW* is about 10 % when S_{11} is about -15 dB. Moreover, the realised gain is extremely stable over the frequency band of interest (9.5-10.5 GHz), having only 0.9 dB fluctuation. The peak gain of the component is 20.32 at frequency 10.45 GHz. The 3-dB gain bandwidth is 12 %. There is a very good attenuation of the realised gain observed at the stop band, whilst it is slightly poorer at the start band.

The E- and H-plane radiation patterns of the component are simulated and measured at three frequency points within the frequency band of interest, and they are shown in Figure 5.12. They are in good agreement with each other. It can be clearly seen that the side lobe levels at all the given frequencies points are below -13 dB in the E-plane. However, because the spacing between the radiating apertures in the H-plane is large due to the inherent electrically large dimensions of rectangular waveguide resonators, the side lobe levels decrease to -7.5 dB.



(a)



(b)

Figure 5.11: (a) Photograph, and (b) Measured frequency response of the fabricated 4th order 4×4 antenna array-filter component compared with the simulated response.

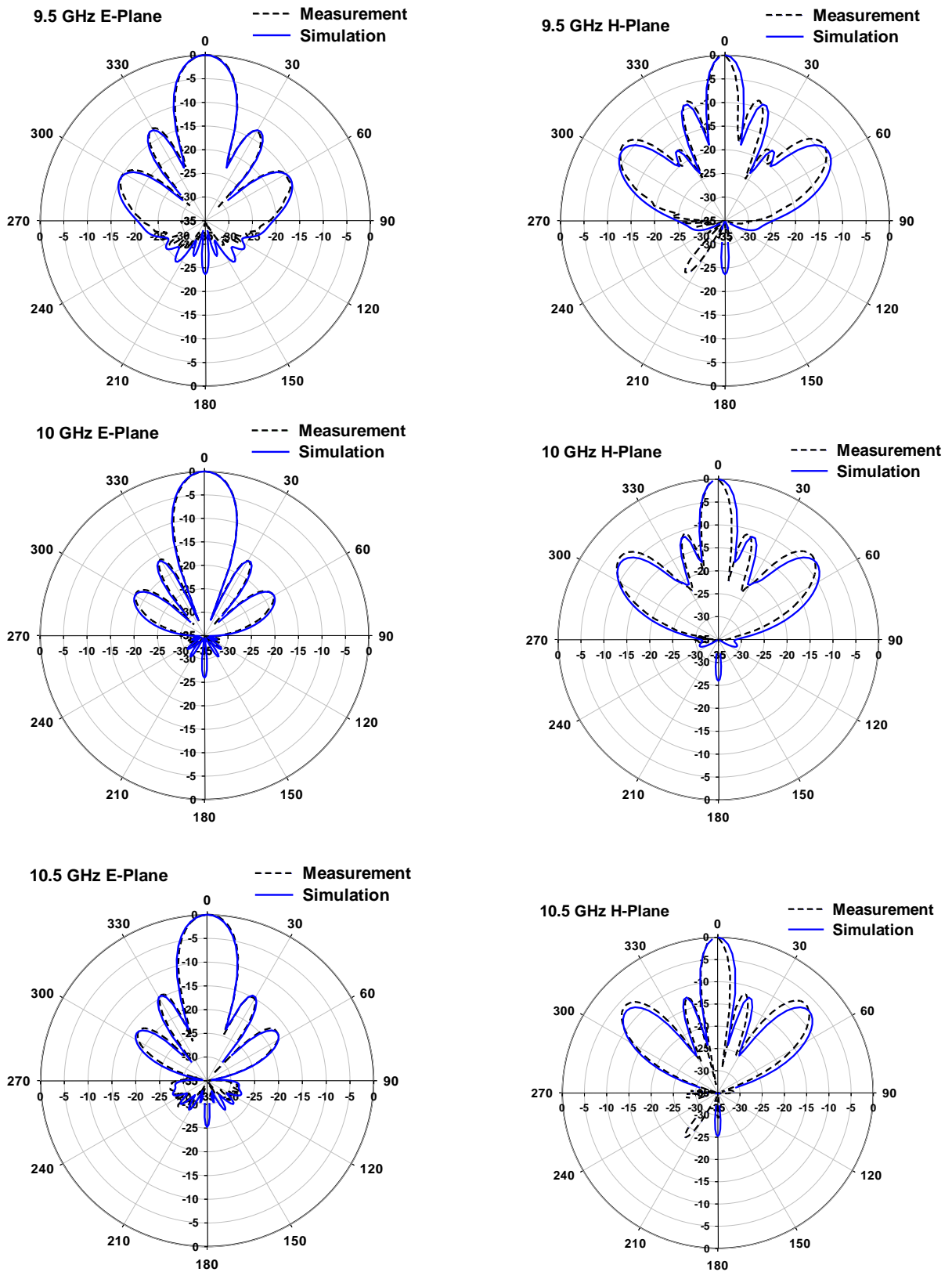


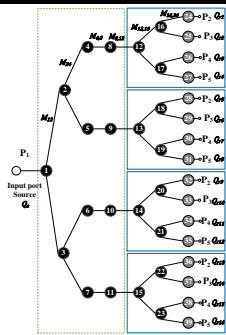
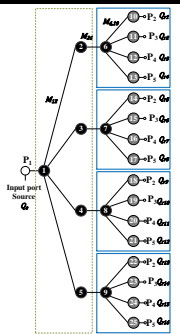
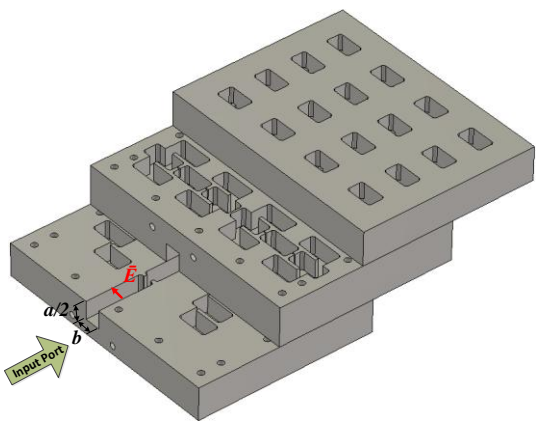
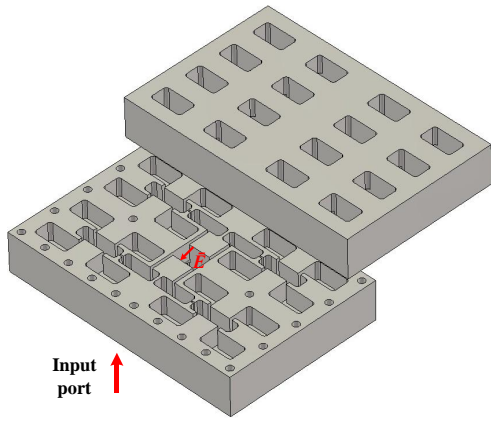
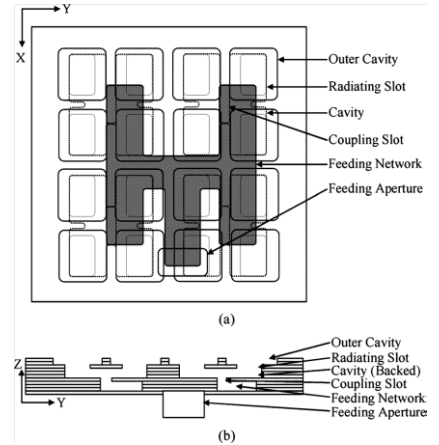
Figure 5.12: The simulated and measured radiation pattern of the 7th order 4×4 antenna array-filter component for both the E- and H-planes at three different frequencies.

5.4 Comparison

Table 5.2 shows a summary of some electrical and physical parameters of the 4×4 *antenna array-filter* components given in this chapter (Section 5.2), Chapter 4 (Section 4.4), and the 4×4 corporate waveguide-fed slot array planar array given in [7]. The topologies, physical configurations, and the number of layer are considered as the most important physical parameters of the components, and they are summarised in the table. On the other hand, the electrical parameters shown in the table are considered as common parameters among them. The gain of the 4×4 corporate waveguide-fed slot array planar array is 20.20 dBi, whilst it increases up to 21.20 dBi when using the outer cavity layer [7]. It is therefore both of the values are mentioned in the table. In addition, because the side lobe level value was not exactly mentioned in the paper [7], thus, it was extracted from the radiation pattern figures and is presented in the table for the purpose of the comparison.

Both 7th and 4th order 4×4 *antenna array-filter* components have a very good filtering functionality, particularly the 7th order component. However, the 4×4 corporate waveguide-fed slot array component has no filtering feature. All the three compared components in Table 5.2 have gain and bandwidth values which are comparable to each other. In terms of side lobe levels, the 4×4 corporate waveguide-fed slot array component has a side lobe level which is better than the other components based on the waveguide resonators. Regarding to the physical size and volume, the 4th order 4×4 *antenna array-filter* component covers less space than the others. In addition to this, there is only one waveguide-layer and two pieces of aluminium are used to construct it. While, for the other two components two waveguide-layers with more than two pieces are utilised.

Table 5.2: Comparison between some physical and electrical specifications of the components at their designed centre frequency.

| Components | | 7 th order 4×4 antenna array-filter (Chapter 4, Section 4.4) | 4 th order 4×4 antenna array-filter (Chapter 5, Section 5.3) | 4×4 corporate waveguide-fed slot array [7] |
|-------------------------|------------------------|--|--|--|
| Physical Specifications | Topology |  |  | NA |
| | Physical configuration |  |  |  |
| | No. of layers | 2 | 1 | 2 |
| | No. of resonators | 39 | 25 | NA |

| Components | | 7 rd order 4×4 antenna array-filter (Chapter 4, Section 4.4) | 4 rd order 4×4 antenna array-filter (Chapter 5, Section 5.3) | 4×4 corporate waveguide-fed slot array [7] | |
|----------------------------------|---|--|--|---|--|
| Electrical Specifications | Bandwidth (%) (VSWR < 1.5 dB) | 10.4 | 10.0 | 12 | |
| | Peak Gain (dBi) | 20.43 | 20.32 | 21.20-20.20 | |
| | Side lobe level at centre frequency (dB) | E-plane | - 13.9 | - 16.5 | \cong - 12.5 (extracted from the Figures) |
| | | H-plane | - 8 | - 7.8 | |
| | Realised gain attenuation (dB) | Start band (8 GHz) | - 50.15 | - 12.80 | NA |
| | | Stop band (12 GHz) | - 44.47 | - 33.52 | |

5.5 Conclusion

In this chapter, design and fabrication for two new components were given. The unique feature of the given components was that they were built by using only a single waveguide-layer. Their performances have been measured, and a very good agreement has been noticed with their equivalent simulation results. Comparisons between the electrical and physical parameters of the given components in this chapter, two components given in Chapter 5, and two other designs presented in the literature were also shown here. The advantages and disadvantages of the components have been discussed based on their physical and electrical specifications. It was realised that the 4th order 4×4 *antenna array-filter* component has advantages over the other components in terms of size and volume. Moreover, 7th order 4×4 *antenna array-filter* component has the better filtering functionality than others.

5.6 References

1. Skaik, T., M.J. Lancaster, and F. Huang, *Synthesis of multiple output coupled resonator circuits using coupling matrix optimisation*. IET microwaves, antennas & propagation, 2011. **5**(9): p. 1081-1088.
2. Studio, C.M., *Computer simulation technology*. GmbH, Darmstadt, Germany, 2009.
3. Shang, X., *SU-8 micromachined terahertz waveguide circuits and coupling matrix design of multiple passband filters*. 2011, University of Birmingham.
4. Guan-Long, H., et al., *Broadband and high gain waveguide-fed slot antenna array in the Ku-band*. Microwaves, Antennas & Propagation, IET, 2014. **8**(13): p. 1041-1046.
5. Hirokawa, J., *Plate-laminated Waveguide Slot Array Antennas and its Polarization Conversion Layers*. Automatika–Journal for Control, Measurement, Electronics, Computing and Communications, 2012. **53**(1).
6. Huang, G.-L., et al., *A Low Profile and Low Sidelobe Wideband Slot Antenna Array Fed by an Amplitude-Tapering Waveguide Feed-Network*. Antennas and Propagation, IEEE Transactions on, 2015. **63**(1): p. 419-423.
7. Kim, D., et al., *4 4-Element Corporate-Feed Waveguide Slot Array Antenna With Cavities for the 120 GHz-Band*. Antennas and Propagation, IEEE Transactions on, 2013. **61**(12): p. 5968-5975.

Chapter 6

Terahertz communication systems and antennas

In this chapter, terahertz applications are reviewed. The benefits and challenges of a communication system that operates in the terahertz frequency band are also discussed. The atmospheric attenuation at terahertz frequencies is a significant challenge. The impact of the attenuation on a terahertz communication system and the role of an antenna to overcome its effects are discussed. Later, a terahertz communication system, proposed to operate at 300 GHz, with a design based on waveguide structure, is briefly discussed. Due to the small size, a conventional milling machine is no longer an appropriate choice to fabricate terahertz waveguide components, so attention has been paid to a promising alternative fabrication technique called micromachining SU-8. Based on the SU-8 fabrication technique, two designs of waveguide antenna arrays are presented.

6.1 Terahertz frequency band and its applications

The terahertz frequency band is a portion of the electromagnetic spectrum which lies between the microwave and infrared regions (see Figure 6.1). It starts from 0.1 THz and goes up to 10 THz [1]. This range of frequency is extremely wide, and covers a large region of the spectrum. In the last two decades, significant attention has been paid to this frequency region due to an interest from a variety of applications such as space science, medical science, agriculture, defence, and security [1-3]. These wide range of applications goes back to the unique features of the electromagnetic waves in the frequency band [4]. For instance, terahertz

electromagnetic waves can penetrate materials with various levels of attenuation which helps with security imaging [5]. Moreover, resolution of images increases when using terahertz frequencies due to the fact that it is in inverse relation to the wavelength [6]. Figure 6.2 shows a photo taken using terahertz waves of a closed cardboard box; all the items placed in the box are identified. This is extremely useful to check the packages and belongings of passengers in airports. Like image resolution, the scattering is also in inverse relation to the wavelength, thus, it is low within the frequency band [4]. Furthermore, a small ionisation effect can be identified in biological tissues when using terahertz frequency instead of X-rays due to less energy being carried by the photons by a factor of six [6-8]. Thus, it is believed that people and animals being diagnosed using terahertz imaging devices are less under the threat from electromagnetic radiation. Advantages of terahertz frequencies are also found in the field of communication systems, and they are discussed in the next section.

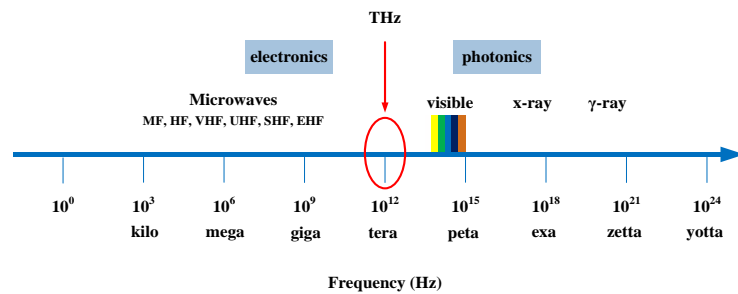


Figure 6.1: Terahertz frequency region illustration at the electromagnetic spectrum [1].

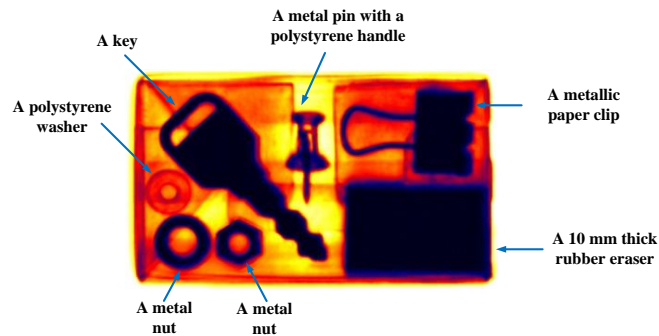


Figure 6.2: Terahertz photo taken for a closed cardboard box [6].

6.2 Terahertz in wireless communication systems

According to the Japanese government, the annual growth of mobile telephone traffic will reach 71% between 2007 and 2017 [9]. A higher growth prediction is also obtained for the United States market [9]. On the other hand, with the increase in the demand from wireless users to deliver varieties of information rather than just simple text messages and voices, an increase in the high data rate capacity for a communication system is necessary. Increasing bandwidth of a communication system is considered a key solution to meeting these demands [1]. Increasing the bandwidth of the system components could fulfil the demands to some extent. However, the bandwidth of the system will still be limited if it is designed at low operating frequency band. In addition to this, the conventional components usually provide a bandwidth of about 10 % of its carrier frequency [1], which may not be sufficient for some applications. These limitations encourage scientists to direct their attention towards the terahertz frequency band. A communication system when operated at terahertz frequencies offers two unique features which are (i) the availability of a larger bandwidth, and (ii) a reduction in the total circuit size.

In the literature, there are several systems demonstrated at millimetre and terahertz frequencies. Two communication systems with operating frequencies of 60 and 90 GHz are presented in [10-12]. In [13], a wireless communication system is proposed to work at 220 GHz, and to have the data rate capability of about 20 Gbit/s over a distance of 100 metres. Another wireless communication link operates at 300 GHz with an experimental verification for the transmitting data stream capability of 12.5 Gbit/s over a distance of 0.5 metre [14]. The technical feasibility of a communication transceiver system with a carrier operating frequency of 307.2 GHz, with a bandwidth of 30 GHz and a capability of transmitting/receiving signals at the speed of 12.5 Gbit/s, is also described in [15].

It can be noticed from the specifications of the systems mentioned above that using a terahertz communication system to transmit/receive signals over a long-range distance is a challenge due to the significant atmospheric path loss effect on the terahertz waves [1, 3]. Figure 6.3 shows the attenuation of the propagated terahertz waves at the sea level within the frequency range of 100 GHz to 1 THz for six atmospheric conditions. It implies that the attenuation increases with an increase in the operating frequency. The Friss transmission equation gives more information regarding the attenuation and frequency relationship, and is discussed in section 6.4. Figure 6.3 also explains that the atmospheric conditions have impacts on the attenuation level. For instance, when there is high humidity, the attenuation level exceeds 10^3 dB/km at frequency 400 GHz and above. It is therefore suggested for a communication system to operate a below 400 GHz. In the following sections, a terahertz communication system, which is proposed to operate at 300 GHz, is briefly demonstrated. Attention is then paid to an antenna and its role in reducing the impact of the atmospheric path loss.

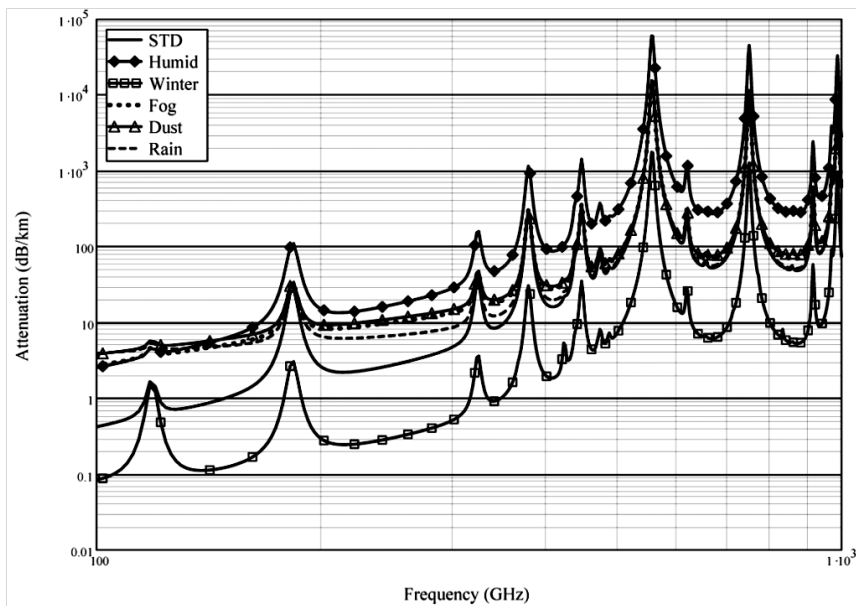


Figure 6.3: Atmospheric attenuation of the propagated waves for six atmospheric conditions at sea level (taken from [3]).

6.3 300 GHz wireless communication system

This section demonstrates a 300 GHz communications system which is being proposed by the EDT research group at the University of Birmingham [16]. It is proposed to build an indoor 10 metres communication link with a data rate capability of 10 Gbit/s. In Chapter 1 a simplified terahertz communication link budget was shown, illustrating the transmitter and receiver parts. Both transmitter and receiver have common components like antennas, bandpass filters, mixers, and amplifiers. Due to the compatibility of waveguide structure, layered SU-8 micromachining technology is considered for the fabrication process of the system [16]. Figure 6.4 shows the proposed transmitter chain architecture of the system, demonstrating the configuration of the components based on five SU-8 layers.

The calculations of the power budget for the system show a free space path length of 10 metre [16]. The path loss for a broadside antenna when operating at 300 GHz is about 100 dB. An antenna with a 32 dBi gain and with an input power of -10 dBm can provide a -56 dBm power level at the receiver [16]. This would be sufficient to achieve a satisfactory Signal-to-Noise-Ratio (SNR) to Bit-Error-Rate (BER), (SNR/BER) ratio. In the following sections, attention is concentrated on the antenna's role in the system, identifying which kind of antenna can be best suited to the system, and designing an antenna for the system, respectively.

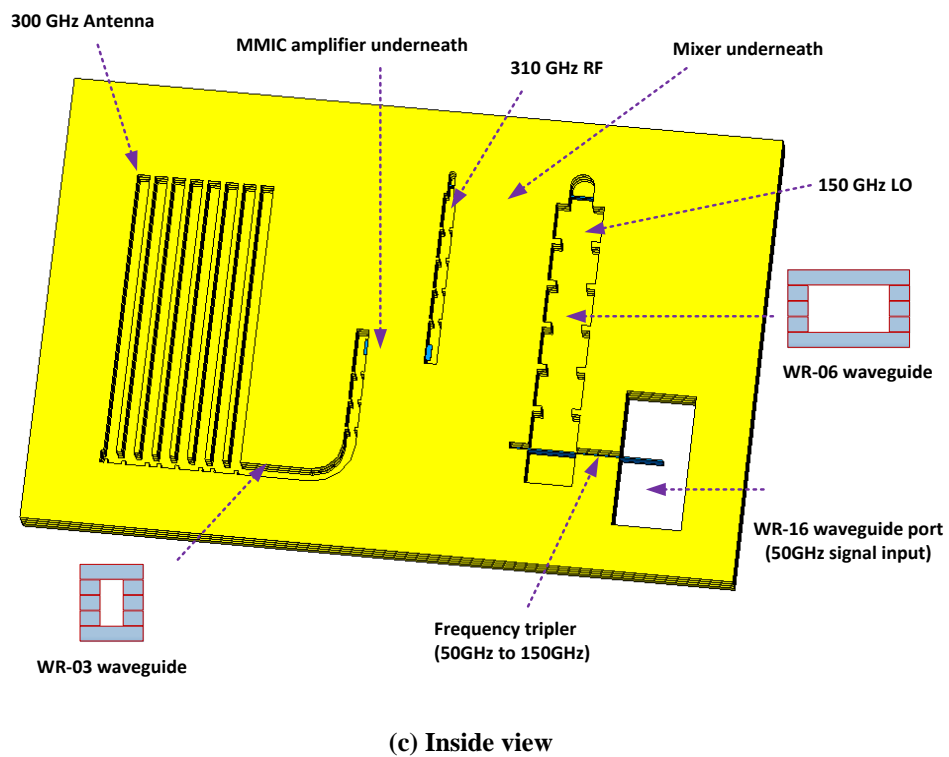
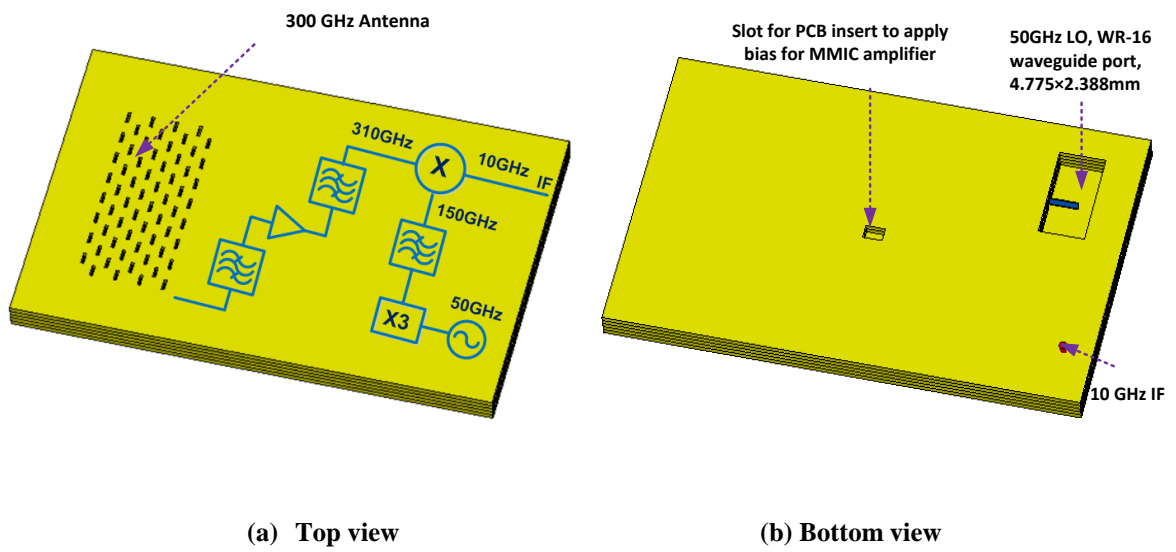


Figure 6.4: Proposed transmitter chain architecture of the 300 GHz System showing the layered view of the components based on the rectangular waveguide structure [16].

6.4 Terahertz antennas

Section 6.2 explains that the atmospheric path loss effect is considered as one of the main challenges facing a terahertz communication system in transmitting/receiving signals over a large distance. It is mentioned in [1], that with the increase of the transmit input power of a system, the range can be increased to some extent. However, due to the limitations of the power source, the transmitting distance still remains shorter than required in some applications. An increase in the antenna gain can be considered as a key solution. To define the function of an antenna in a wireless communication system, a look at the Friss Transmission Equation is necessary. The equation for a wireless communication system placed in free space is [17]:

$$P_r = G_{d_r} G_{d_t} \left[\frac{\lambda}{4\pi r} \right]^2 P_t \quad (6.1)$$

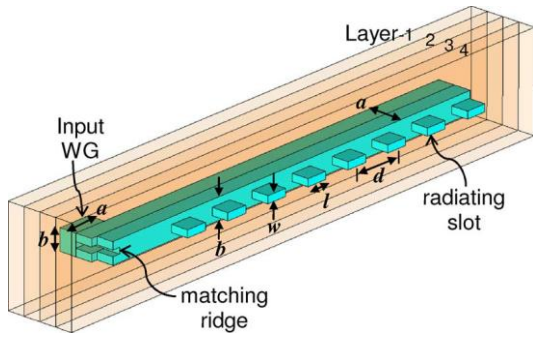
Here P_r , P_t , G_{d_t} , G_{d_r} , r , and λ are the power received by the receiver antenna, P_t is the power transmitted by the transmitter antenna, gain of the transmitter antenna, gain of the receiver antenna, the distance between the transmitter and receiver antennas, and operating free space wavelength, respectively. It can be observed from Equation 6.1 that the received power is in inverse relation to the square of the distance between the antennas and the operating frequency. It is believed that increasing the antenna gain is one good approach to lead to a terahertz system that can operate over a relatively long-range.

There are several kinds of antennas presented in the literature which could be of interest for terahertz communication systems. Lens antennas are considered a good candidate due to their gain being simply increased by (i) increasing the size of the antenna, and (ii) using the relative permittivity of the dielectric material used in constructing the antenna [1]. In [18], a 246 GHz

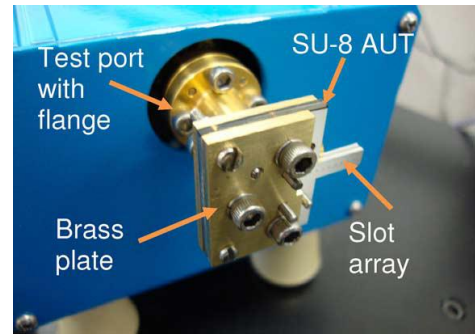
high gain lens antenna is demonstrated. It is fed by placing double slots at the back of the lens. Another dielectric lens antenna is reported in [19], investigating the effect of the edge illumination on the radiation characteristic performance. A terahertz leaky wave lens antenna, which is suitable for non-dispersive links over a wide bandwidth, is also demonstrated in [20].

Horn antennas are another type that could fulfil terahertz communication systems requirements. In [21], a 1.6 THz waveguide horn antenna was fabricated using the monolithic micromachined waveguide technique. The fabrication of the tapering section of horn antennas usually requires a very accurate and costly fabrication process. Reflector antennas also seem a promising candidate. An optical system is proposed in [22], using a reflector-based antenna for the purposes of re-focusing terahertz beam and high resolution applications.

An antenna with a planar structure is interesting particularly for the proposed terahertz communication system shown in Section 6.3 due to its physical advantages and simplicity in packaging. Micromachined SU-8 photoresist technology has been developed at the University of Birmingham to fabricate terahertz planar-based components like filters [23-25] and antennas [26, 27]. A 300 GHz linear array slotted waveguide antenna based on four SU-8 silver coated layers was fabricated (Figure 6.5), and demonstrated in [26]. The measured performance of the antenna validates the accuracy of the fabrication technique at such an operating frequency band. Another antenna named the Fabry-Perot cavity antenna, with a 2D planar structure as shown in Figure 6.6, was also constructed using the same fabrication process [27]. It is believed that using SU-8 fabrication technology it is possible to fabricate further terahertz planar antennas. In the following sections, the designs of two antennas, compatible with the SU-8 layers, are presented.

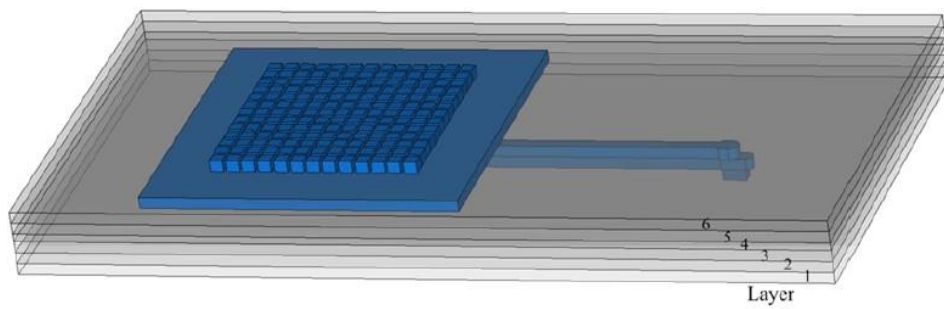


(a)

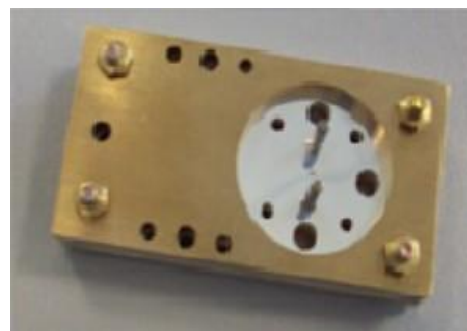
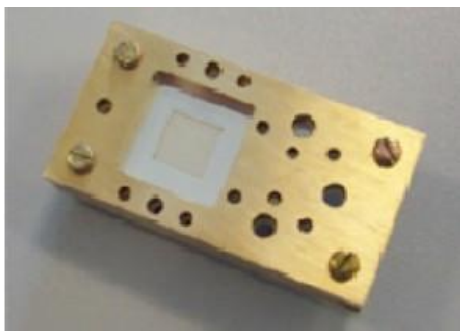


(b)

Figure 6.5: 3D view of Slotted waveguide antenna, (b) Antenna under test (taken from [26]).



(a)



(b)

Figure 6.6: (a) 3D view of the Fabry Perot cavity antenna, (b) The actual antenna (taken from [27]).

6.5 Design of 300 GHz planar array 8×8 slotted waveguide antenna

This section describes the design of an 8×8 planar array narrow-wall slotted waveguide antenna operating in the WR-03 band frequencies (220-325 GHz). It is illustrated in Figure 6.7. The antenna is proposed to be constructed from five SU-8 silver coated layers with equal thicknesses ($t = 0.288$ mm). The top layer contains the slots and the following three layers form the radiating and feeding waveguides. The bottom layer is to enclose the whole design and maintain the input port position. As can be seen from Figure 6.7, the slots are cut on the narrow-wall of radiating waveguides with one-guide wavelength spacing. Such spacing produces grating lobes in the radiation pattern of the antenna [17, 26]. In order to suppress the grating lobes, the slots on a radiating waveguide are alternated with those on the neighbour radiating waveguides by half a guide wavelength ($\lambda_g/2$).

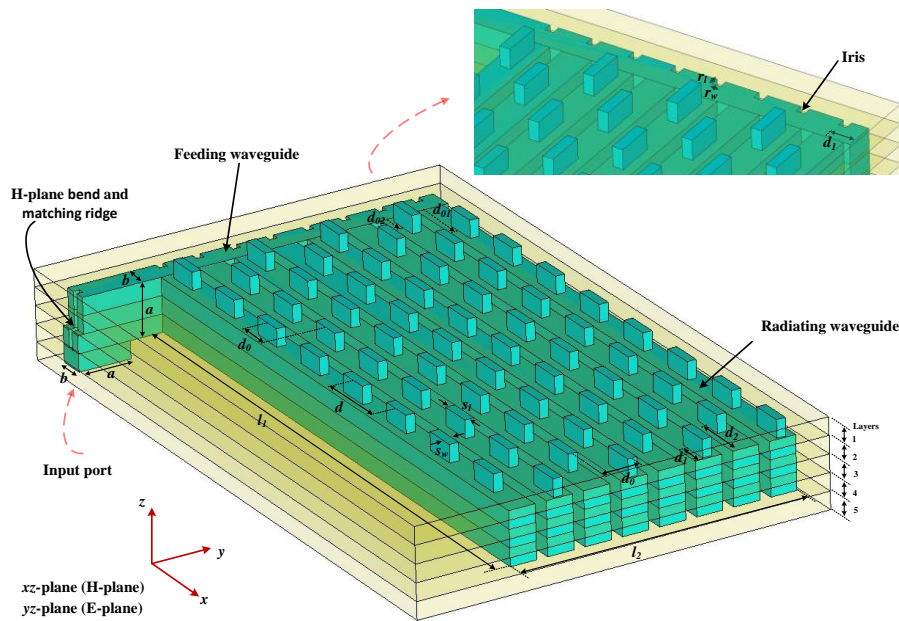


Figure 6.7: 3D layout of the narrow-wall 8×8 slotted waveguide antenna.

The radiating waveguides are attached directly to the feeding waveguide (see enlargement section in Figure 6.7). This forms a series of T-junction E-planes. In order to couple power to

the radiating waveguides, irises are designed at each junction. The lengths of the irises are used to control the coupling power and to cancel reflection due to the junctions. It should be mentioned that some of the irises are shifted away from the centre of the junctions. This is to keep the resonant centre frequency at 300 GHz. The H-plane waveguide bend designed in Chapter 2 (Section 2.5.3) is embedded with the antenna here in order to facilitate the measurement process. The dimensions of the slots and the inter-element spacing for the antenna are obtained following the design steps given in Chapter 2 (Section 2.5.2). Table 6.1 summarises some of the physical dimensions of the antenna.

Table 6.1
Physical dimensions of the planar array 8×8 slotted waveguide antenna.

| No. | Parameters | Value (mm) |
|-----|---|----------------------|
| 1 | Waveguide Dimensions $a \times b$ | 0.864×0.432 |
| 2 | Radiating System Area $l_1 \times l_2$ | 9.903×4.723 |
| 3 | Enter Slot Space d | 1.226 |
| 4 | Slot dimensions $S_1 \times S_w$ | 0.578×0.134 |
| 5 | Neighbour Slot space d_0 | 0.613 |
| 6 | Length and width of irises $r_l \times r_w$ | 0.131×0.123 |
| 7 | Layer Thickness SU-8 b_1 | 0.288 |
| 8 | Last slot centre to end (d_1, d_2) | 0.307, 0.920 |
| 9 | First slot centre to feeding waveguide (d_{01}, d_{02}) | 1.014, 0.401 |

6.5.1 Simulation Results

The simulated results of the proposed antenna are analysed and discussed in this section. The variation of the return loss, directivity and the realised gain versus frequency are obtained using CST simulator [28], and they are plotted in Figure 6.8. The S_{11} is below -30 dB at the centre frequency of 300 GHz, with a bandwidth of about 2 GHz when $|S_{11}|$ is -10 dB. Moreover, the maximum directivity is depicted at the centre frequency 300 GHz, and is 25.20

dBi. The losses due to the material and the mismatch cause a reduction in the antenna realised gain of about 0.6 dBi at 300 GHz. The 3-dB gain bandwidth is 1.3% at 300 GHz.

Figure 6.9 shows the radiation pattern of the proposed antenna at three frequency points including the centre frequency for both E- and H-planes. The side lobe levels are below -13 dB for both of the planes and at all the given frequency points. It is found that with the increase in the operating frequency, a small distortion in radiation patterns occurs, particularly in the E-plane. Also, a beam inclination of about 2° is observed in the E-plane with the increase of the operating frequency to 301 GHz. This could be due to the phase variation of the EM waves at that plane. Table 6.2 summarises some of the simulated electrical parameters of the antenna.

Table 6.2
Electrical parameters of the planar array 8×8 slotted waveguide antenna.

| Parameters | Frequency (GHz) | Directivity (dBi) | Realised Gain (dBi) | Bandwidth (GHz) | 3dB beam width | Side lobe level (dB) |
|-------------|-----------------|-------------------|---------------------|-----------------|---|--------------------------------|
| Performance | 300 | 25.19 | 24.59 | 2 | E-plane 13.2° H-plane 5.0° | E-plane -14.8 H-plane -13.4 |

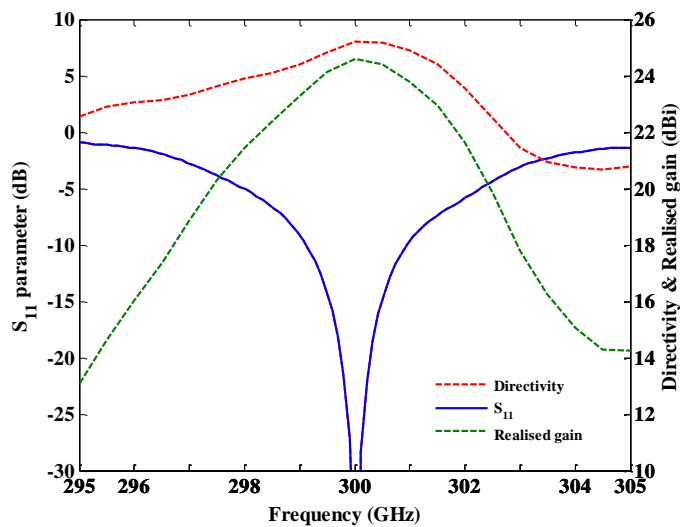


Figure 6.8: Variation of of the simulated directivity, realised gain and return loss of of the proposed antenna versus frequency.

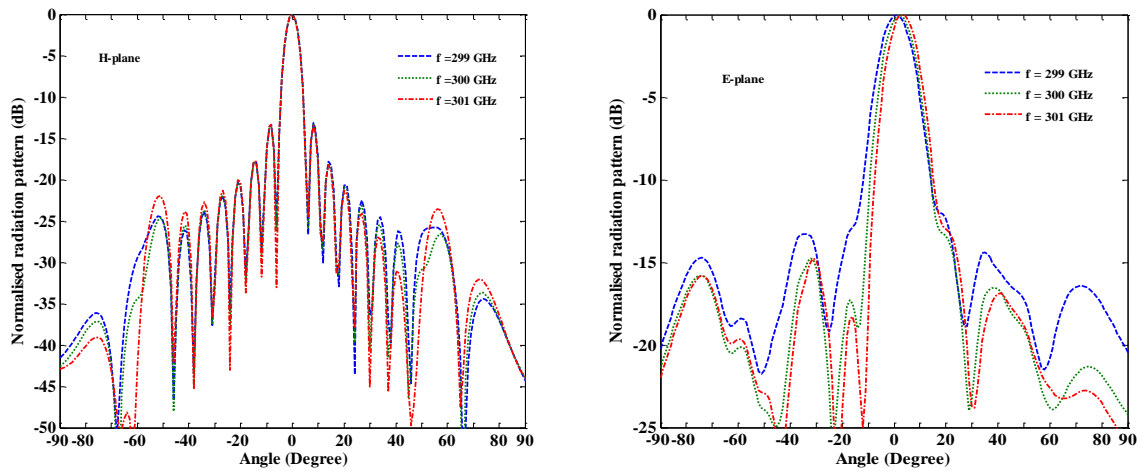


Figure 6.9: Simulated radiation patterns of the proposed antenna for E- and H-planes at three frequency points including the centre frequency.

6.5.2 Fabrication

This section discusses the fabrication process of the antenna using the SU-8 micromachining technique. This technique is useful due to its ability to achieve high aspect ratio in the form of the waveguide structures as well as high dimension accuracy [26, 29]. In addition to this, the fabrication cost is relatively low [30]. Moreover, the thickness of the photoresist can be controlled.

The antenna has been prepared to fabricate using five equal thickness (0.288 mm) SU-8 silver coated layers (Figure 6.10). Silver coating for the SU-8 layers is chosen after finding its losses similar to solid metals for waveguide structures [23]. All five SU-8 layers were included in one mask and were produced in one go during the lithography process. Liquid SU-8 was firstly applied on a 4-inch silicon wafer. The initial soft bake was performed at a temperature 65° C for 20 minutes, and then 95° C for about 4 hours. Subsequently, the SU-8 photoresist

was exposed through the mask to 365 nm ultra violet light. After the completion of the exposure, the post exposure bake for the SU-8 was begun directly first at 65° C for 2 minutes first and later at 95° C for 30 minutes. The SU-8 wafer was left to cool to room temperature. In order to make the SU-8 photoresist more robust, more development was performed using the EC solvent and then hard-baked at 150° C. All the SU-8 photoresist pieces were released from the silicon wafer using a 10% sodium hydroxide solution. Finally, they were silver-coated with 2 micron-thickness in a vacuum evaporator. During the evaporation, the SU-8 pieces were rotated at an angle in order to allow the evaporated-silver to coat the inside of the slots and the H-plane bend ridges of the antenna. Additional information regarding the SU-8 fabrication process is provided in [30-32].

Once the SU-8 photoresist layers were constructed and coated, they were assembled in a very precise manner using alignment and precision pins (see Figure 6.12). Two brass-plates were introduced to the fabricated antenna in order to (i) give high strength, (ii) clamp together, and (iii) maintain direct interconnection of the antenna with the waveguide flange. The influence of the brass-plates on the radiation characteristics of the antenna has been minimised by choosing appropriate l_1 and l_2 dimensions (Figure 6.10). The simulated antenna performance with and without the brass plates is compared in Figure 6.11, and negligible effects of the brass plates on the antenna performance have been observed. The photograph of the fabricated antenna is shown in Figure 6.12. However, the antenna has delaminated and measurements were not possible. The measurements will be performed when the fabrication is completed successfully.

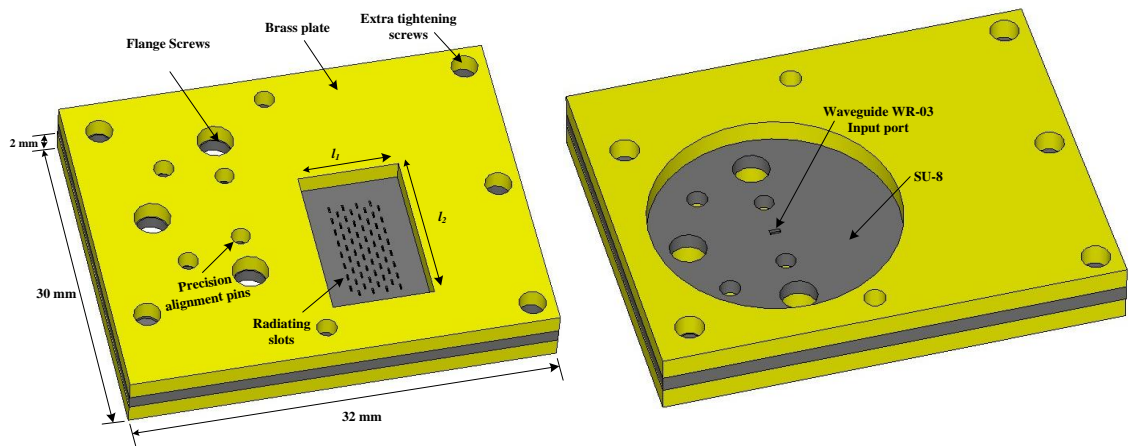


Figure 6.10: Complete structure of the proposed 8×8 slotted waveguide antenna, including the brass plates and the required holes for interconnection with the waveguide flange.

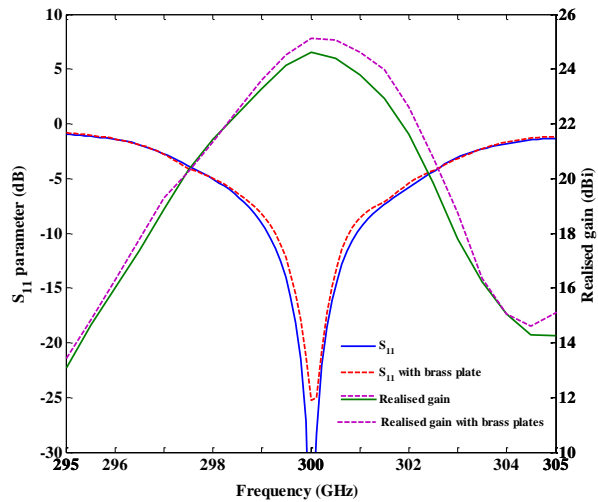


Figure 6.11: Effects of the brass plates on the simulated frequency performance of the proposed antenna.

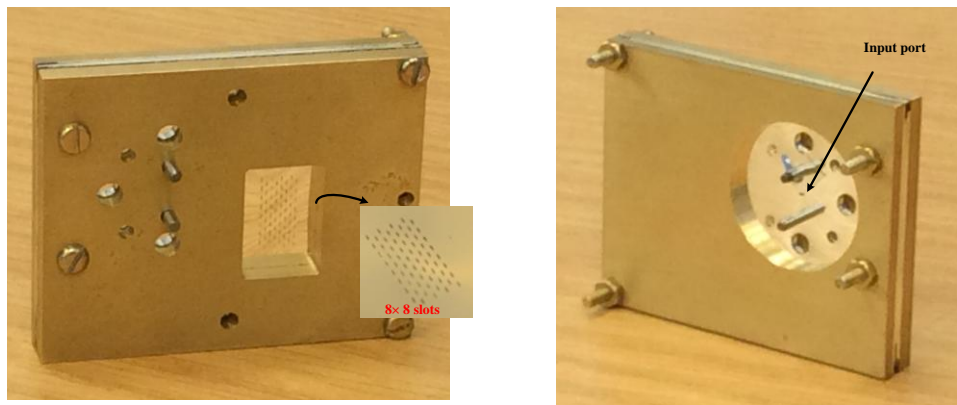


Figure 6.12: Photograph of the fabricated 8×8 slotted waveguide antenna.

6.6 Micromachined travelling-wave array slotted waveguide antenna

High gain and wide bandwidth antennas have received much attention for beam scanning radar applications at the millimeter wave and terahertz frequency bands. To date, different types of antenna arrays have been investigated for this purpose. Microstrip patch antenna arrays are attractive high gain antennas. However, they suffer from a series of losses when operating at high frequencies [33, 34]. The curvature shape of a parabolic dish antenna and its difficulty in packaging with a communication system are issues which make the antenna less preferable for the applications [34]. There has been increasing interest in using beam scanning waveguide antennas due to their compact size, simplicity in fabrication, and inherent low losses [26, 35].

Since 1950, frequency scanning waveguide slot antenna arrays have been introduced for radar applications [36-38]. In a conventional travelling-wave array slotted waveguide antenna, a matching load is placed at the termination of waveguides to absorb the power not radiated, and a phase shifter to control the main beam direction. However, due to the inefficiency of shifters, and the challenge of employing a matching load onto an antenna because of the reduced size at terahertz frequencies; their implementation would be very difficult [39, 40]. In the next section, an H-bend radiated (HBR) slot has been designed (Figures 6.13 and 6.16) instead of a matched load in the designed frequencies (220-325 GHz). Following that, the radiation characteristics of the HBR slot are discussed. The HBR slot is then integrated in Section 6.6.2 with 7 radiating slots placed on the narrow wall of a rectangular waveguide (WR-03) to form a linear array travelling-wave array antenna. The performance of the array in terms of antenna gain, bandwidth, and beam scanning are demonstrated. The antenna array presented here has been designed to be compatible with the micromachined SU-8 photo-resist

layers. The interconnection of the antenna with the standard waveguide flange WR-03 and its assembly with the brass plates are demonstrated in sub-Section 6.6.4.

6.6.1 Design of HBR slot

The HBR slot shown in Figure 6.13 has a length of (a) and a width of (b). Three matching steps are introduced in the waveguide below the radiating slot to minimise the power reflected to the input port. The simulated reflection coefficient of the HBR slot is obtained using CST microwave studio [28], and is less than -20 dB within the whole operating frequency band (Figure 6.14). The slot has a gain of (6.85dBi) at 300 GHz with only 0.8 dBi variation over the whole WR-03 band as can be seen in Figure 6.14. The radiation pattern of the HBR slot is presented in Figure 6.15. A small degradation on the right hand side of the H-plane radiation patterns can be identified due to the asymmetrical physical structure.

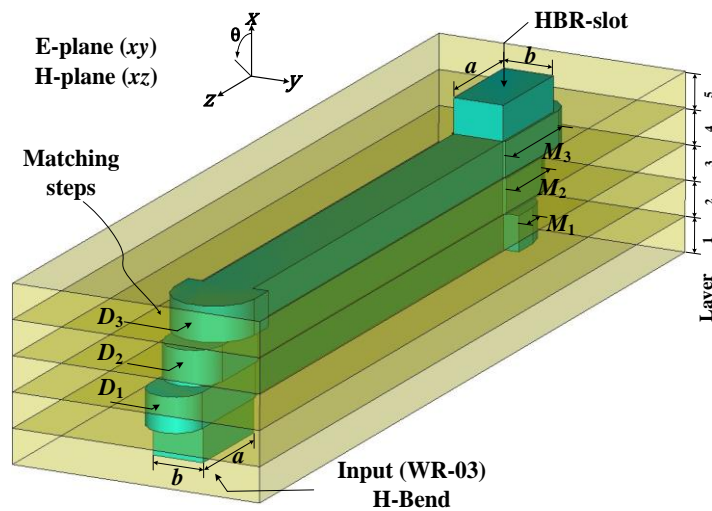


Figure 6.13: Diagram of the designed HBR slot with the characterisation of the three matching steps. $B = 0.432$ mm, $d = 0.96$ mm, $a = 0.864$ mm, $D_1 = 0.699$ mm, $D_2 = 0.499$ mm, $D_3 = 0.469$ mm, $M_1 = 0.24$ mm, $M_2 = 0.60$ mm, $M_3 = 0.91$ mm.

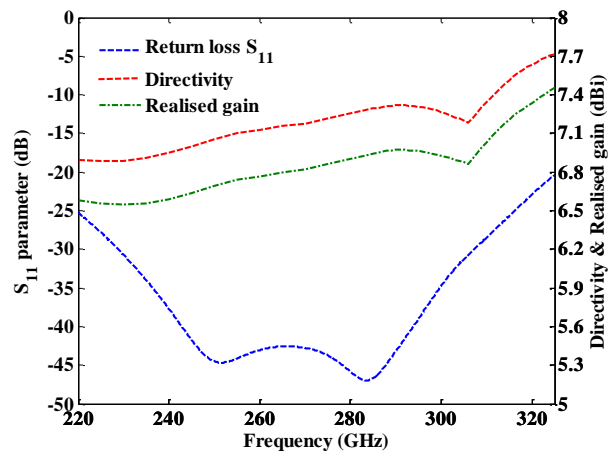


Figure 6.14: Variation of S_{11} , realised gain, and directivity of the HBR slot versus frequency.

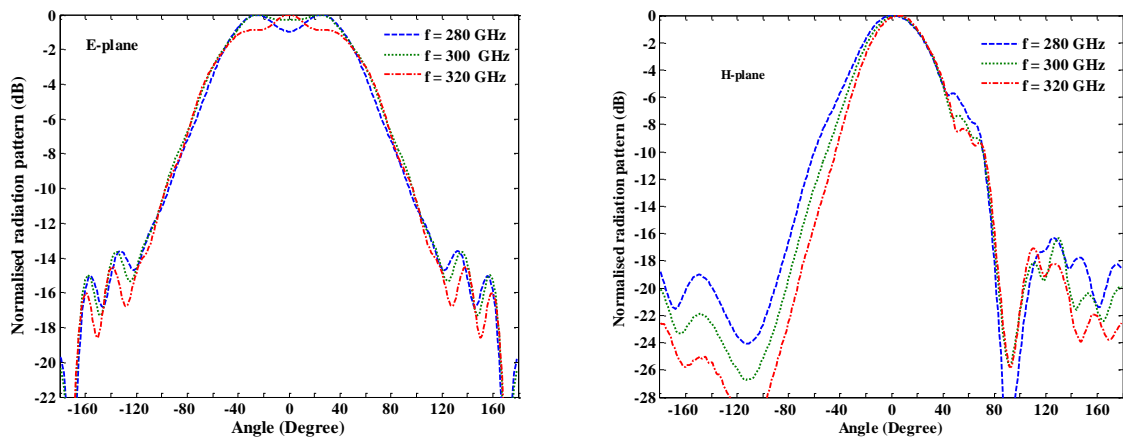


Figure 6.15: Radiation pattern of the designed HBR slot at three different frequencies for both E- and H-planes.

6.6.2 Design of linear array with 8-radiating slots

The complete travelling-wave slotted waveguide antenna array is shown in Figure 6.16. For a travelling-wave array, the spacing between the radiating slots does not have to be λ_g [41, 42] as discussed in chapter 2. Here, all the slots are not excited in phase. As a result of this, a progressive phase shift is generated between the radiating slots, and the main beam pattern

starts scanning with the change in the operating frequency. For the design presented here, the inter-element space is optimised, and chosen to be $d = 0.78 \lambda_g$. This provides a wide bandwidth and a wide beam scanning range for the array.

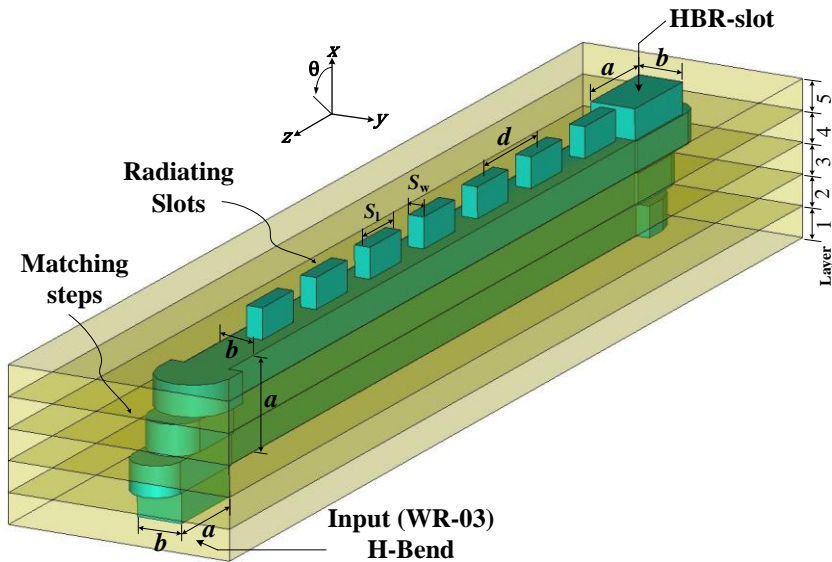


Figure 6.16: Layout of an 8-slot travelling array cut in the centre of the narrow wall of the waveguide based on the micromachining layers (equal thickness $t = 0.288$ mm). An H-plane bend is integrated with the structure at the input port and an H-plane radiating slot at the input port. The outstanding structure in the central represents the hollow waveguide WR-03 and slots, while the surrounding id conductor which is set to be transparent). $a = 0.864$ mm, $b = 0.432$ mm, $d = 0.964$ mm, $S_w = 0.15$ mm, $S_1 = 0.55$ mm.

6.6.3 Design performance

This section demonstrates the simulated performance of the antenna operated at 300 GHz. The simulated radiation pattern of the antenna has a main beam in the H-plane which is -13° scanned towards the input port, with the existence of one grating lobe at 55° as shown in Figure 6.17 (a). The scanning of the main beam has occurred due to the produced progressive phase shift between the slots in accordance with the input port phase. The appearance of single grating lobe is because of the spacing ($0.78 \lambda_g$) which is still larger than half of the

free- space wavelength. The side lobe level is -13.3 dB in the E-plane which is better than -6.8 dB in the H-plane as can be seen in Figure 6.17 (a). A very good return loss matching, which is below -15 dB from 240 to 325 GHz, is observed in Figure 6.17 (b). The peak gain of the antenna is 14.37 dBi at 287 GHz. As a result of the good matching, the realised gain and directivity of the antenna are comparable to each other.

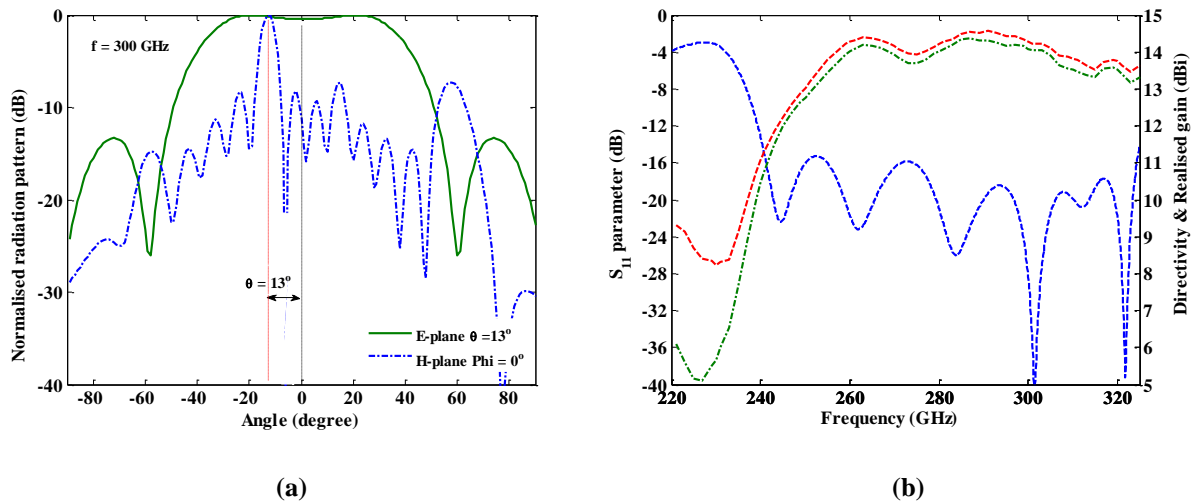


Figure 6.17: (a) Simulated radiation pattern of the 8-slots at operating frequency 300 GHz for both E- and H-planes, (b) variation of the antenna return loss, directivity, and realised gain over the whole operating frequency band.

6.6.4 Main beam scanning

This section discusses the scanning of the main beam and the radiation patterns of the antenna with respect to frequency change. The H-plane radiation patterns in Figure 6.18 indicate that their main beam scans from -27° to -7° with the frequency from 255 to 325 GHz, which means a 20° main beam scanning over 23.3 % fractional bandwidth ($1.16^\circ/\text{GHz}$). The beam scanning feature is significant for such a simple antenna structure which makes it a good candidate for terahertz wave and radar applications. Further scanning can be achieved when

the antenna is operated close to the cut-off frequency. However, in this case, the main beam degrades.

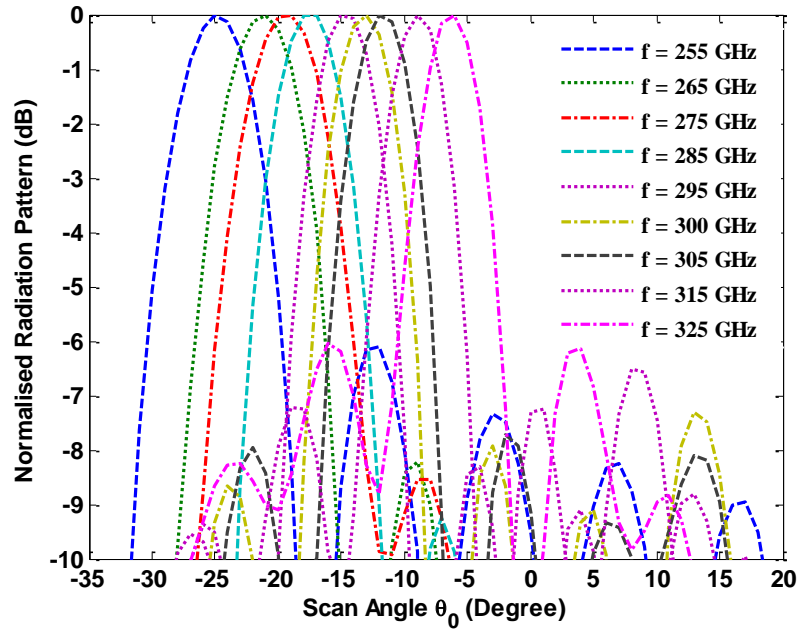


Figure 6.18: Normalised H-plane radiation pattern of an 8-slotted waveguide array with the variation of operating frequencies from 255 to 325 GHz. The total beam scanning is 20° over a 23.3 GHz fractional bandwidth.

The proposed antenna array structure can be fabricated using micromachining SU-8 silver coated layers. The full assembly of the antenna is shown in Figure 6.19. The brass plates are used to clamp the five SU8 layers. The effect of the brass plates on the performance of the antenna has been minimised by keeping enough space around the array. The influence of the brass plates on the frequency response of the antenna is shown in Figure 6.20, and this only causes a small discrepancy in the performance of the antenna.

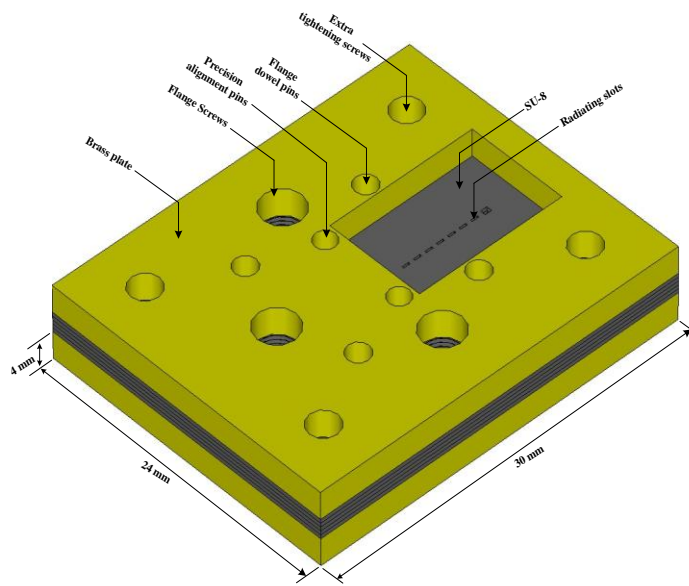


Figure 6.19: CST model of the assembled antenna. The holes are for the necessary screws to connect the antenna with the WR-03 waveguide flange.

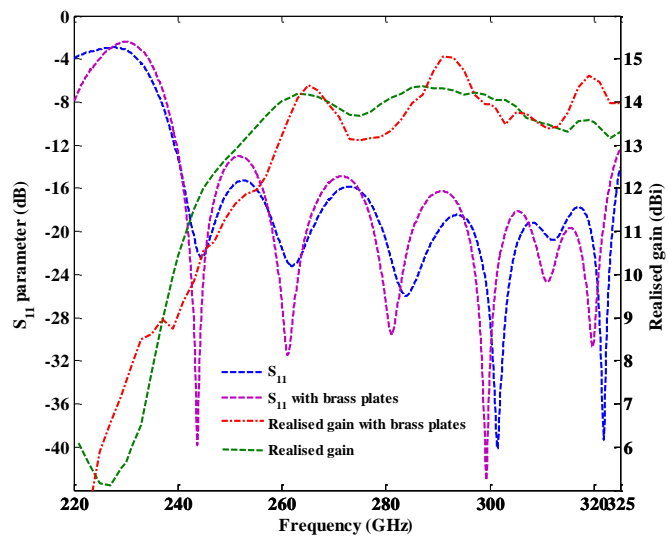


Figure 6.20: Effects of the brass plates on the simulated frequency performance of the proposed antenna.

6.7 Conclusion

In this chapter, terahertz frequency applications were discussed. The advantages and challenges, that will be present when designing a communication system to operate at terahertz frequencies, were also addressed. Moreover, a 300 GHz communication system, which is currently being investigated at the University of Birmingham, was briefly described. Later, more attention was paid to those antennas which are suitable for terahertz communication systems, more specifically for the proposed 300 GHz communication system. Two antennas, named the 'planar array 8×8 slotted waveguide antenna' and the linear array travelling-wave slotted waveguide antenna have been introduced, and their performances have been obtained and analysed in simulation.

6.8 References

1. Jha, K.R. and G. Singh, *Terahertz planar antennas for next generation communication*. 2014: Springer.
2. Armstrong, C.M., *The truth about terahertz*. Spectrum, IEEE, 2012. **49**(9): p. 36-41.
3. Appleby, R. and H.B. Wallace, *Standoff Detection of Weapons and Contraband in the 100 GHz to 1 THz Region*. Antennas and Propagation, IEEE Transactions on, 2007. **55**(11): p. 2944-2956.
4. Woolard, D.L., et al., *Terahertz Frequency Sensing and Imaging: A Time of Reckoning Future Applications?* Proceedings of the IEEE, 2005. **93**(10): p. 1722-1743.
5. Lee, Y.-S., *Principles of terahertz science and technology*. Vol. 170. 2009: Springer Science & Business Media.
6. Dobroiu, A., C. Otani, and K. Kawase, *Terahertz-wave sources and imaging applications*. Measurement Science and Technology, 2006. **17**(11): p. R161.
7. Berry, E., et al., *Do in vivo terahertz imaging systems comply with safety guidelines?* Journal of Laser Applications, 2003. **15**(3): p. 192-198.
8. Zhang, X., *Terahertz wave imaging: horizons and hurdles*. Physics in Medicine and Biology, 2002. **47**(21): p. 3667.
9. Ho-Jin, S. and T. Nagatsuma, *Present and Future of Terahertz Communications*. Terahertz Science and Technology, IEEE Transactions on, 2011. **1**(1): p. 256-263.
10. Daniels, R.C. and R.W. Heath Jr, *60 GHz wireless communications: emerging requirements and design recommendations*. Vehicular Technology Magazine, IEEE, 2007. **2**(3): p. 41-50.
11. Daniels, R.C., et al., *60 GHz wireless: Up close and personal*. Microwave Magazine, IEEE, 2010. **11**(7): p. 44-50.
12. Frigyes, I., et al. *Applicability of the 50–90 GHz frequency bands in feeder networks*. in *Antennas and Propagation, 2009. EuCAP 2009. 3rd European Conference on*. 2009. IEEE.
13. Zhang, B., Y.O. Fan, and Z. Chen. *220-GHz-band wireless link system using all-electronic technologies for 20Gbit/s data transmission*. in *Intelligent Signal Processing and Communication Systems (ISPACS), 2010 International Symposium on*. 2010. IEEE.
14. Song, H.-J., et al. *Terahertz wireless communication link at 300 GHz*. in *Microwave Photonics (MWP), 2010 IEEE Topical Meeting on*. 2010. IEEE.
15. Chia, M., et al. *Wideband 307 GHz transceiver system for high speed digital wireless at 12.5 Gbps*. in *Microwave Symposium Digest (MTT), 2011 IEEE MTT-S International*. 2011. IEEE.
16. Lancaster, M.J., *Ep/m016269/1 epsrc research grant application*. 2015.
17. Sadiku, M., *Elements of electromagnetics (the oxford series in electrical and computer engineering)*. 2002: Oxford University Press, USA.

18. Filipovic, D.F., S.S. Gearhart, and G.M. Rebeiz, *Double-slot antennas on extended hemispherical and elliptical silicon dielectric lenses*. Microwave Theory and Techniques, IEEE Transactions on, 1993. **41**(10): p. 1738-1749.
19. Boriskin, A.V., R. Sauleau, and A. Nosich, *Performance of hemielliptic dielectric lens antennas with optimal edge illumination*. Antennas and Propagation, IEEE Transactions on, 2009. **57**(7): p. 2193-2198.
20. Neto, A., *UWB, non dispersive radiation from the planarly fed leaky lens antenna—Part 1: Theory and design*. Antennas and Propagation, IEEE Transactions on, 2010. **58**(7): p. 2238-2247.
21. Bowen, J.W., et al., *Micromachined waveguide antennas for 1.6 THz*. Electronics Letters, 2006. **42**(15): p. 842-843.
22. Llombart, N., et al., *Confocal Ellipsoidal Reflector System for a Mechanically Scanned Active Terahertz Imager*. Antennas and Propagation, IEEE Transactions on, 2010. **58**(6): p. 1834-1841.
23. Xiaobang, S., et al., *WR-3 Band Waveguides and Filters Fabricated Using SU8 Photoresist Micromachining Technology*. Terahertz Science and Technology, IEEE Transactions on, 2012. **2**(6): p. 629-637.
24. Xiaobang, S., et al., *A SU8 Micromachined WR-1.5 Band Waveguide Filter*. Microwave and Wireless Components Letters, IEEE, 2013. **23**(6): p. 300-302.
25. Wang, Y., X. Shang, and M.J. Lancaster. *Micromachined 3D millimeter-wave and terahertz devices*. in *Advanced Materials and Processes for RF and THz Applications (IMWS-AMP), 2015 IEEE MTT-S International Microwave Workshop Series on*. 2015.
26. Yi, W., et al., *Micromachined 300-GHz SU-8-Based Slotted Waveguide Antenna*. Antennas and Wireless Propagation Letters, IEEE, 2011. **10**: p. 573-576.
27. Konstantinidis, K., et al., *Micromachined terahertz Fabry-Perot cavity highly directive antennas*. Microwaves, Antennas & Propagation, IET, 2015. **9**(13): p. 1436-1443.
28. Studio, C.M., *Computer simulation technology*. GmbH, Darmstadt, Germany, 2009.
29. Shang, X., et al., *Micromachined W-band waveguide and filter with two embedded H-plane bends*. Microwaves, Antennas & Propagation, IET, 2011. **5**(3): p. 334-339.
30. Shang, X., *SU-8 micromachined terahertz waveguide circuits and coupling matrix design of multiple passband filters*. 2011, University of Birmingham.
31. He, T., *Filtering amplifiers based on coupled resonator circuits*. 2015, University of Birmingham.
32. Konstantinidis, K., *Multi-layer periodic surfaces and metasurfaces for high-gain antennas*. 2015, University of Birmingham.
33. Ando, M. and J. Hirokawa. *High-gain and high-efficiency single-layer slotted waveguide arrays in 60 GHz band*. in *Antennas and Propagation, Tenth International Conference on (Conf. Publ. No. 436)*. 1997. IET.

34. Sekretarov, S. and D.M. Vavriv, *A wideband slotted waveguide antenna array for SAR systems*. Progress In Electromagnetics Research M, 2010. **11**: p. 165-176.
35. Wang, Y. and M. Lancaster. *A micromachined centre-fed slotted waveguide antenna for mm-wave applications*. in *Microwave Workshop Series on Millimeter Wave Wireless Technology and Applications (IMWS), 2012 IEEE MTT-S International*. 2012. IEEE.
36. Robertson, R.M., *Variable Width Waveguide Scanners for Eagle (AN/APQ-7) and GCA (AN/MPN-1)*. 1946: Radiation Laboratory, Massachusetts Institute of Technology.
37. Gustafson, L., *S-band two-dimensional slot array*. Hughes Aircraft Company, Culver City, CA, Tech. Memo, 1957. **462**.
38. Derneryd, A. and T. Lorentzon. *Design of a phase/frequency scanned array antenna with non-resonant slotted ridge waveguide elements*. in *Antennas and Propagation Society International Symposium, 1991. AP-S. Digest*. 1991. IEEE.
39. Cullens, E.D., et al., *Micro-fabricated 130–180 GHz frequency scanning waveguide arrays*. Antennas and Propagation, IEEE Transactions on, 2012. **60**(8): p. 3647-3653.
40. Ranzani, L., et al., *G-Band Micro-Fabricated Frequency-Steered Arrays With 2/GHz Beam Steering*. Terahertz Science and Technology, IEEE Transactions on, 2013. **3**(5): p. 566-573.
41. Johnson, R.C. and H. Jasik, *Antenna engineering handbook*. New York, McGraw-Hill Book Company, 1984, 1356 p. No individual items are abstracted in this volume., 1984. **1**.
42. ISOGAI, Y. and T. TAKESHIMA, *Frequency bandwidth of slotted array aerial system(Center feed system for broadening frequency bandwidth in X-band edge slotted waveguide array antenna)*. ELECTRONIC ENGINEERING, 1969. **41**: p. 201-204.

Chapter 7

Conclusions and future work

7.1 Conclusions

The main objective of this PhD work was to investigate antennas that can provide high gain and wide bandwidths. There are many communication systems in today's modern society that demand an antenna with such specifications, and the proposed 300 GHz communication system presented in Chapter 1 and discussed in Chapter 6 is an example [1]. In Chapter 2, a review of the previous work related to high gain and wide bandwidth antennas was given. The limitations of antenna gain and bandwidth parameters were discussed together with antenna size. Clear visions regarding their limitations have resulted.

Due to the trade-off between the gain and bandwidth parameters, achieving a wide bandwidth for a high gain antenna has always been a challenge. In Chapter 3, a new approach has been presented to design high gain and wide bandwidth antennas. The approach was based on the coupling matrix theory. The parameters of the matrices such as coupling coefficient (M_{ij}) and quality factors (Q_{ei} , Q_{rj}) have been investigated in chapter 3 using rectangular waveguide cavity resonators. We have concluded that the bandwidth of the antennas, made with coupled resonators and using the new approach, can be controlled by M_{ij} , Q_{ei} and Q_{rj} values of the matrices.

The new approach presented in chapter 3 has been implemented with six novel antenna topologies in chapters 4 and 5. The components have been constructed based solely on

resonators. They have confirmed the flexibility in accomplishing wide bandwidth and high gain. Moreover, the designed antennas have gained filtering functionality, as a result of the new approach. This is extremely useful due to the fact that a bandpass filter is no longer necessary after the antenna. The measured performances of the fabricated antennas were in very good agreement with their simulations, validating the new design approach.

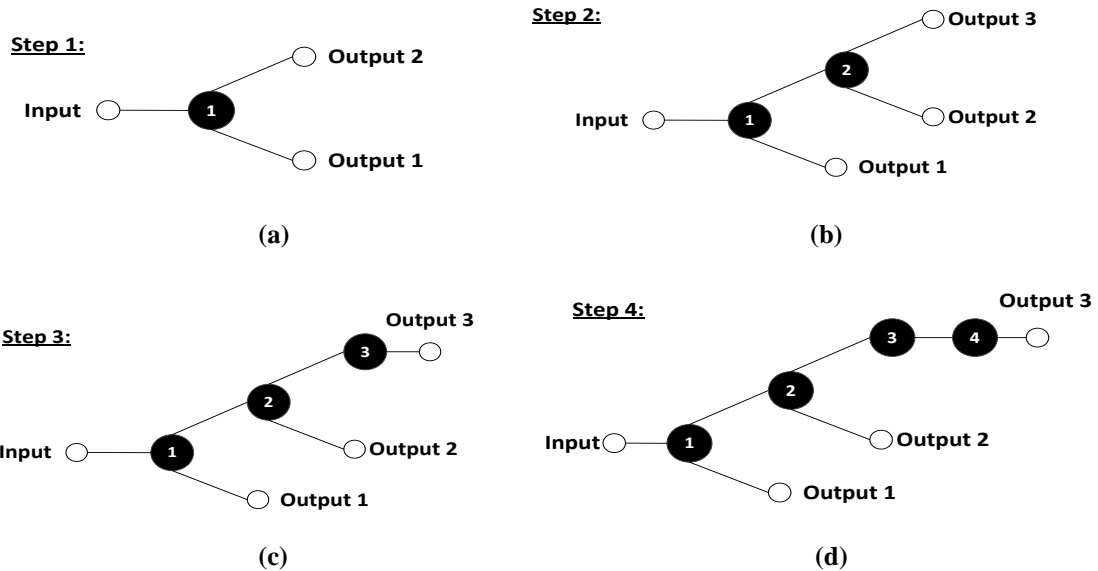
Finally, a terahertz communication system proposed to operate at 300 GHz [1] was reported in Chapter 6. The specification of the system was briefly detailed. Later, the antenna required for the system and its specification dominated the main theme of the chapter. A design of 300 GHz planar array (8×8) slotted waveguide antenna based on SU-8 layered waveguide technology has been introduced, and its fabrication discussed. Additionally, a 300 GHz linear array travelling-wave slotted waveguide antenna has been proposed which could be of interest to terahertz beam scanning applications.

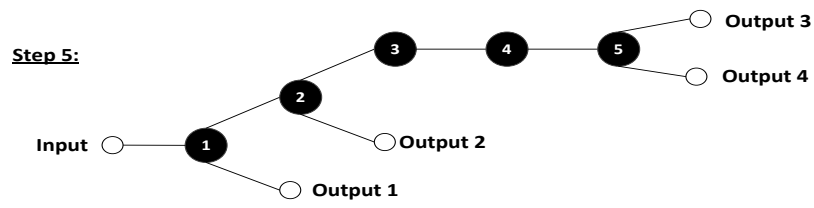
7.2 Future work

The design approach presented in this thesis can be developed further still by seeking different antenna topologies so as to reduce the circuit size and suppress the side lobe levels of the radiation patterns further. Moreover, the *antenna array-filter* components presented in Chapters 4 and 5 were based on equal power splitter topologies. Using unequal power splitter topologies can be useful to maintain an extreme side lobe level suppression of the radiation patterns.

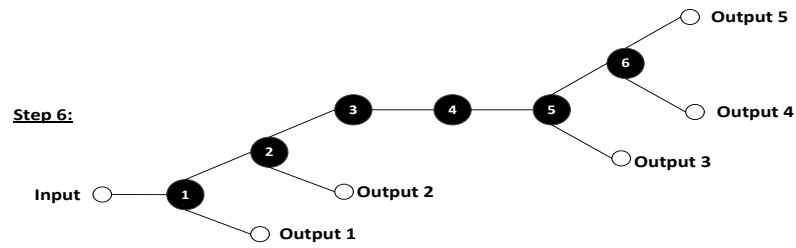
As discussed in Chapter 3, the new design approach has allowed us to control the antenna bandwidth with gain. However, when the component sizes become large electrically (large

arrays), the computational time required by an EM simulator to simulate them is long. Obtaining the desired response is not guaranteed due to having many resonators and physical dimensions to tune. The step tune technique presented in [2, 3] can be used to overcome this issue. Instead of tuning the whole component, the technique allows us to tune the component step by step. For each step, no more than three physical parameters of the resonators are required to be tuned. Figure 7.1 shows the necessary steps required for the design of the 7th order 4×4 antenna array-filter component presented in Chapter 4. It consists of seven steps, adding one resonator at each successor steps until reaching to the last resonator. This promises to obtain the desired responses and reduce the computational time. It should be mentioned here that for each step, an equivalent coupling matrix is required. This technique will be utilised in the future for the design of 8×8 and 16×16 planar antenna array-filter components when appropriate topologies are prepared.

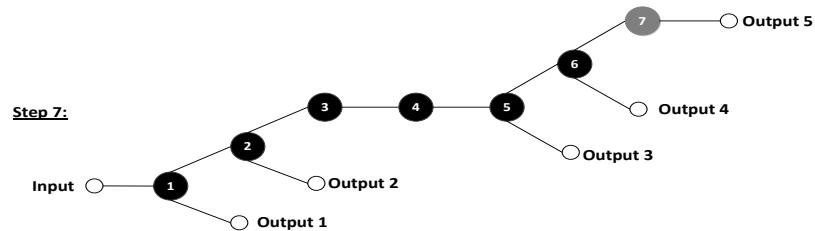




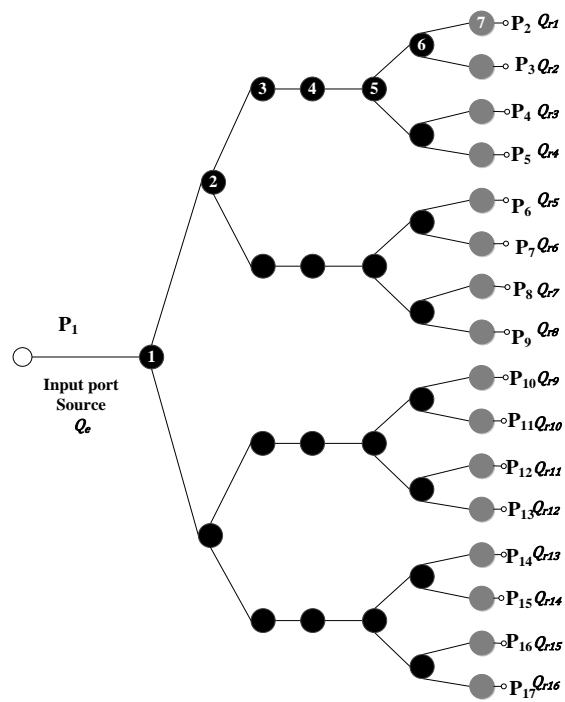
(e)



(f)



(g)



(h)

Figure 7.1: (a-g), Design steps for the 7th order 4×4 antenna array-filter component, (h) the whole topology.

The design of multiband antennas and the use of cross-coupled topologies which introduce transmission zeros to the antenna gain response so as to increase the out-of-band rejections are the aspects left for future investigations. For these purposes, advantages can be taken from the topologies presented in Chapters 4 and 5.

The antenna integrated with the 300 GHz communication system in Chapter 6 (Section 6.3) has narrow bandwidth ($\sim 1\%$ *FBW*). Since our ultimate goal is to have an antenna having 10% *FBW* at 300 GHz, the bandwidth of the integrated antenna will have to be broadened eventually for the final prototype of the system. There are two ways that can be used for this purpose. These are (i) building the antenna based on coupled-resonators using the coupling matrix approach as introduced in Chapter 3, and/or (ii) employing the reflection cancelling techniques presented in [4] into the antenna.

7.3 References

1. Lancaster, M.J., *Ep/m016269/1 epsrc research grant application*. 2015.
2. Xia, W., *Diplexers and multiplexers design by using coupling matrix optimisation*. 2015, University of Birmingham.
3. Shang, X., W. Xia, and M.J. Lancaster, *The design of waveguide filters based on cross-coupled resonators*. *Microwave and Optical Technology Letters*, 2014. **56**(1): p. 3-8.
4. Sakakibara, K., et al. *A slotted waveguide array using reflection-cancelling slot pairs*. in *Antennas and Propagation Society International Symposium, 1993. AP-S. Digest*. 1993.